Distribution Agreement

In presenting this thesis or dissertation as a partial fulfillment of the requirements for an advanced degree from Emory University, I hereby grant to Emory University and its agents the non-exclusive license to archive, make accessible, and display my thesis or dissertation in whole or in part in all forms of media, now or hereafter known, including display on the world wide web.   I understand that I may select some access restrictions as part of the online submission of this thesis or dissertation.   I retain all ownership rights to the copyright of the thesis or dissertation.   I also retain the right to use in future works (such as articles or books) all or part of this thesis or dissertation.

Signature:

_____   _____
                                                    Date

Development of DNA-based Fluorescent Molecular Tension Probes

to Investigate Integrin Mediated Mechanical Forces

By

Yun Zhang

Doctor of Philosophy

Chemistry

_____
Khalid Salaita
Advisor

_____
Brian Dyer
Committee Member

_____
Stefan Lutz
Committee Member

Accepted:

_____
Lisa A. Tedesco, Ph.D.
Dean of the James T. Laney School of Graduate Studies

_____
Date

Development of DNA-based Fluorescent Molecular Tension Probes

to Investigate Integrin Mediated Mechanical Forces

By

Yun Zhang

B.S. Xiamen University, 2010

Advisor: Khalid Salaita, Ph.D.

An abstract of

A dissertation submitted to the Faculty of the

James T. Laney School of Graduate Studies of Emory University

in partial fulfillment of the requirements for the degree of

Doctor of Philosophy

in Chemistry

2016

Abstract

Development of DNA-based Fluorescent Molecular Tension Probes

to Investigate Integrin Mediated Mechanical Forces

By Yun Zhang

Mechanical stimuli profoundly alter cell functions and cell fate, yet the mechanisms underlying mechanotransduction remain obscure because of a lack of methods for molecular force imaging. The aim of this dissertation is to describe the design and application of DNA hairpin force probes to study β_3 integrin receptor involved mechanotransduction mechanisms in living cells.

Chapter 1 introduces the cell adhesion molecules participating in mechanotransduction processes, mainly focusing on the integrin subfamily of adhesion receptors. This chapter also analyzes and compares the available tools and methods for directly measuring the forces transduced by integrins.

Chapter 2 gives a detailed description of the development of a new class of molecular tension probes that employs a DNA hairpin as a 'switch' element. This probe unfolds at a specific threshold force and reports tension in a digital rather than analogue manner. Application of the DNA-based probes in early focal adhesions reveals that $\alpha_v\beta_3$ integrins prefer stiffer ligands at the leading tip of the focal adhesions.

Chapter 3 explores the role of $\alpha_{IIb}\beta_3$ integrin mechanics in platelet activation, which is critical in the process of clot formation. We found that lateral ligand mobility influenced platelet activation. Using the DNA-based probe, the first molecular tension map of $\alpha_{IIb}\beta_3$ integrin was generated, revealing platelet mechanics with high spatial and temporal resolution. This work led to a proposed model for the role of mechanics in platelet activation and aggregation.

Chapter 4 details the development of a DNA-origami tension sensor, aiming at increase the force threshold of current single hairpin molecular probes via multiple parallel sensors at the end

of a DNA six-helix bundle. Force calibration and simulations revealed unexpected mechanical response of this origami structure, providing novel insights into DNA nanostructure mechanics. Biological application of this design was demonstrated through the measurement of platelet forces.

Chapter 5 summarizes the thesis and discusses future directions for DNA based molecular tension probes. These tools are anticipated to impact the field of mechanotransduction by enabling force measurements with high spatial and temporal resolution.

Development of DNA-based Fluorescent Molecular Tension Probes

to Investigate Integrin Mediated Mechanical Forces

By

Yun Zhang

B.S. Xiamen University, 2010

Advisor: Khalid Salaita, Ph.D.

A dissertation submitted to the Faculty of the

James T. Laney School of Graduate Studies of Emory University

in partial fulfillment of the requirements for the degree of

Doctor of Philosophy

in Chemistry

2016

Acknowledgements

First and foremost, I would like to thank my advisor, Khalid Salaita, for letting me join the group when I first came to the United States to start my PhD. He is one of the most optimistic and passionate scientists I have ever worked with, and I am very grateful for the mentorship and guidance he has provided during my time at Emory. I also would like to thank the members of my thesis committee, Dr. Brian Dyer and Dr. Stefan Lutz for offering their advice, challenging me to think about my research and being patient with me as a last-minite person. I would like to extend my gratitude to Dr. Vincent Conticello for being on my committee for my second-year talk, third-year data report and fourth-year research proposal.

I would also like to thank the past and current members of the Salaita lab for the help and assistance over the past five years and making these years entertaining and exciting at Emory. I cannot imagine having survived graduate school without their support. I am also very grateful to my collaborators for their expertise in other fields. I am very grateful for the time I was able to spend with Jing Chen, Yuxing Wang, Liangbin Fu, Huan Huang and so many others!

Thanks to my parents for their unconditional love and support. I am also grateful for my dog "Dollar" for being here with me and my parents' dogs "ShuaiShuai" and "DuDu" for accompanying my parents.

Finally, I would like to thank my fiancé who consistently sacrifices his time to video-chat with me and gives me the freedom to pursue my Ph.D. Without his support this work would not have been possible.

List of Abbreviation

Abbreviation	Full Name
AFM	atomic force microcopy
AGD	HHLGGAKQAGDV
BFP	biomembrane force probes
CAM	cell adhesion molecule
cRGDfK	cyclic Arg-Gly-Asp-D-Phe-Lys
ECM	extracellular matrix
EGF	epidermal growth factor
EGFR	epidermal growth factor receptor
FAs	focal adhesions
FRAP	fluorescence recovery after photobleaching
FRET	förster resonance energy transfer
ICAM-1	intercellular adhesion molecule-1
MLCK	myosin light chain kinase
mPAD	micropost array detector
MTFM	molecular tension-based fluorescence microscopy
NSET	nanometal surface energy transfer
PA	polyacrylamide

PECAM-1	platelet endothelial CAM-1
PEG	polyethylene glycol
pN	piconewton
PS	phosphatidylserine
PSGL-1	P-selectin glycoprotein ligand-1
QE	quenching efficiency
RICM	reflection interference contrast microscopy
ROCK	Rho-associated protein kinase
SCFM	Single cell force microcopy
SLB	supported lipid bilayer
sLe^X	sialy Lewis^X
TFM	Traction force microscopy
TSMod	tension sensor module
VinTS	vinculin tension sensor
WLC	worm-like chain

Table of Contents

List of Tables

Chapter 1   Mechanotransduction by cell adhesion molecules and the methods to study

cellular forces

1.1   Mechanotransduction by cell adhesion molecules

Cells are constantly subject to mechanical forces. For example, fibroblasts in blood vessels are exposed to shear stress by blood flow, and cardiomyocytes within cardiac muscles are repeatedly contracted. Osteocyte formation is also stimulated by physical activities.[1] The mechanism by which living cells convert mechanical forces into biochemical signal is called mechanotransduction.[2] This process requires cells to first sense the forces (either from the extracellular matrix (ECM) or neighboring cells) and then to transduce the forces into cells. Finally, cells transform these physical cues into biochemical signaling pathways. Many molecules such as ion-channels, myosins, integrins and cytoskeletal structures have been shown to be involved in the process of mechanotransduction.[3] Among these mechano-chemical mediators, cell adhesion molecules (CAMs) emerge as important components for force sensing and signal transduction. Along with the identification of tension sensing proteins, new technological breakthroughs in force measurements have enabled biophysicists to characterize the dynamics of cellular forces with high temporal and spatial resolution.[4]

This chapter will introduce the major types of CAMs, their roles in mechanotransduction, and the current tools available to measure mechanics at the cellular level.

1.1.1 Examples of CAMs for cell-cell and cell-ECM interaction

CAMs are integral membrane proteins that bind to ligands and receptors on neighboring cells and the ECM in order to maintain the overall multicellular structure. The typical structure of a CAM consists of an extracellular domain for ligand binding, a transmembrane domain and a cytoplasmic tail which interacts with other proteins, such as kinases or adaptor proteins, to trigger

biochemical signaling pathways and to link to the cytoskeleton. There are four major types of

adhesion molecules (Figure 1.1): 1) the cadherins, 2) LEC-CAMs, cell adhesion molecules with

lectin-like domains, 3) the immunoglobulin (Ig) and 4) integrins.[5, 6]
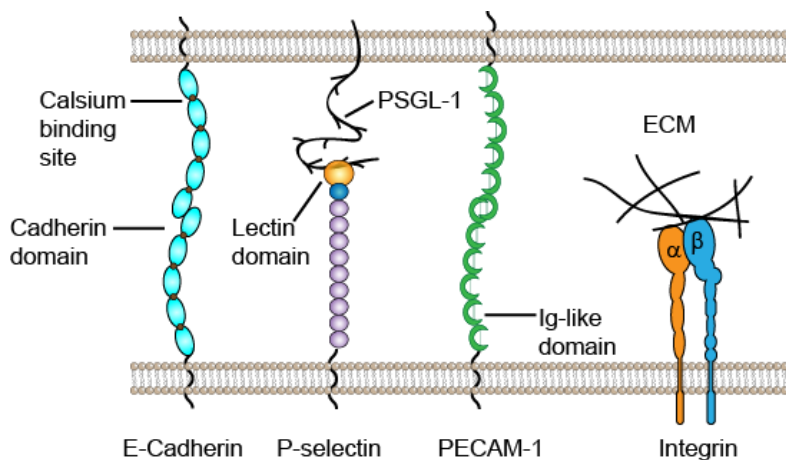
Figure 1.1 Representative molecules from the four major families of cell-adhesion molecules (CAMs). E-Cadherin from the cadherin family and the PECAM-1 from the immunoglobulin (Ig) superfamily of CAMs mediate homophilic cell-cell adhesions. In a heterophilic interaction, the lectin domain of P-selectins binds sugar chains presented on adjacent cells. Integrin, as the major cell-ECM adhesion molecule, is a heterodimer of α and β subunits.

1.1.1.1 Cadherins and E-cadherins

Cadherins, a family of Ca^{2+}-dependent CAMs, are the major receptors of cell-cell adhesions,

playing critical roles in cell recognition and tissue morphogenesis.[7, 8] Cadherins are highly

abundant in brain, presumably due to the necessity of forming specific cell-cell contacts. Loss of

cadherins in cancer cells has shown to promote tumor progression.[9, 10] Members of the cadherin

family can be classified into at least five major subfamilies: classical cadherins of type I, cadherin

of type II, desmosomal cadherins, protocadherin and other cadherin-related molecules.[11]

E-cadherin (epithelial cadherin, a type I cadherin) is the prototype of all cadherins because it

is the most extensively studied and characterized cadherin. E-cadherin contains an N-terminal

extracellular region, a transmembrane anchor and a C-terminal intracellular region. The ectodomain consists five characteristic extracellular cadherin domains, which are rigidified into a curved conformation by Ca^{2+} binding (Figure 1.1).[12] E-cadherins bind cells together through a homophilic mechanism; cadherins on one cell bind to the same molecules on adjacent cells. Homophilic partner binding strengthens and stabilizes the adhesion site. The forces required to separate E-cadherin-expressing cell doublets (200 nN) were significantly higher than the breaking force of the adhesion junctions formed between an E-cadherin-expressing cell and an N-cadherin-expressing cell.[13]

Extensive literature has shown that E-cadherin mediated junctions mechanically connect cells in tissues. Through catenin, vinculin and other proteins, E-cadherins are linked intracellularly with actin cytoskeletons.[14-16] Such couplings endow mechanosensitivity to the cadherin junctions. When forces were applied to the E-cadherin complex, junction stiffness was reported to increase by 70%, accompanied by the accumulation of F-actins and vinculins at adhesion site.[15] Furthermore, the stability of the interaction between E-cadherins and adaptor proteins has been shown to be force-dependent. The E-cadherin/β−catenin/α-catenin complexes exhibit a catch-bond behavior, meaning that the bond stability increases when ~5 to 10 pN of tension is applied to this complex.[17]

1.1.1.2 Lectin-CAM and P-selectins

Lectins are carbohydrate-binding receptors for specific cell adhesions. A lectin usually contains several binding sites for carbohydrate units. Lectins from one cell bind to the sugar moieties presented on the membrane of another cell through relatively weak interactions. Based

on the binding domains and biochemical properties, lectins can be divided into different classes. C-type lectins (calcium required lectin) comprise a large family of lectin receptors that interact with sugars in a Ca^{2+} dependent way, playing important roles in cell-cell adhesions and immune responses.[18]

P-selectins, a prototype C-type lectin receptor, are mainly expressed on activated platelets and endothelium. It is the largest one in the selectin family with a mass of 140 KDa and 40-nm extracellular domain. P-selectins have an N-terminal lectin domain for ligand binding, an epidermal growth factor (EGF) motif, nine regulatory protein repeats and a C terminal transmembrane section with a short cytoplasmic tail.[19] P-selectins from granule release mediate leukocyte rolling via the interactions with the glycoprotein counter-ligand P-selectin glycoprotein ligand-1 (PSGL-1) on the leukocyte surface.[20, 21]

The adhesive interactions of P-selectin with it ligands are under hydrodynamic shear stresses. To fulfill their physiological function, these interactions exhibit some unique mechanical properties. The complexes can withstand forces greater than 100 pN and the stability of the complexes is directly proportional to the loading rate.[22] The complex also shows a high molecular elasticity with a spring constant of 5.3 pN/nm and rapid on-and-off rates, which are necessary to support leukocyte rolling at physiological shear stresses.[23] Marshall et al. provided direct evidence of catch-bond behavior between P-selectin and PSGL-1.[24] They showed that the bond lifetime first increased at forces below 20 pN and then decreased with additional forces, indicating that the catch-bond was followed by a slip-bond. After this work, Sarangapani et al. from the same lab also revealed that this catch-bond behavior also exists in the interaction of

L-selectin and PSGL-1, suggesting that the catch-bond behavior is possibly a general mechanism for selectin-ligand adhesion under shear flow.[25] Expression of P-selectins on the platelet membrane has also been reported to further stabilize platelet aggregation, suggesting a mechanical role of P-selectin in cell-cell adhesion.

1.1.1.3 Immunoglobulin superfamily and PECAM-1

Immunoglobulin superfamily (IgSF) is a large and diverse family of calcium-independent transmembrane glycoproteins. Different from the cadherins forming specific adhesion junctions between two cells, IgSFs are distributed along the cell membrane. The definitive characteristic of the IgSF members is that the N-terminal extracellular domain contains several immunoglobulin-(Ig-) like domains, whereas the conserved cysteine residues stabilize two opposing antiparallel β−sheets into a sandwich structure (Figure 1.1).[26] The C-terminal cytoplasmic tail of IgSF usually interacts with adaptor proteins and cytoskeletal proteins, such as actin, spectrin and afadin.[27, 28] Examples of the IgSF include intercellular adhesion molecule-1 (ICAM-1), neural CAM (NCAM), and platelet endothelial CAM-1 (PECAM-1).

PECAM-1, also known as CD31, is found on platelets, endothelial cells, monocytes and certain types of T-cells. Its structure comprises six Ig-like extracellular domains, a short transmembrane domain and a cytoplasmic domain, whereas two Tyrosine-based Inhibitory Motifs (ITIMS) at Tyr 663 and Tyr 666 have been characterized to initiate further signaling pathways.[29] Phosphorylation of these tyrosine residues also promotes the interaction of the cytoplasmic tail with cytoskeletal components, such as catenin.[30] The Ig-like domain 1 is important for the homophilic binding of PECAM-1 in the intercellular junctions of endothelial cells and the Ig-like

domains 5 and 6 have been shown to be involved in the heterophilic binding interaction with neutrophil-specific antigen CD177, integrin $\alpha_v\beta_3$, and CD38 on lymphocytes.[31]

PECAM-1 plays important roles in mechanosensing in endothelial cells. Early studies showed that PECAM-1 at cell-cell junction is rapidly phosphorylated when subjected to fluid shear stress.[32, 33] Soon after, PECAM-1 was demonstrated to be a direct force transducer in the mechanosensory complex of PECAM-1/VE-cadherin/VEGFR2, which further activating phosphatidylinositol-3-OH kinase (PI(3)K) and integrin.[34] FRET-based tension sensors engineered into VE-cadherin and PECAM-1 reported that fluid shear stresses triggered a simultaneous increase in tension across PECAM-1 and a decrease in tension across VE-cadherin.[35, 36] By using magnetic tweezers to specifically pull on PECAM-1 molecules on endothelial cells, Collins et al. provided the direct evidence showing that tensional forces resulted in global activations of PI(3)K and RhoA, which in turn triggered integrin activation, cytoskeletal remodeling and cell stiffening.[37]

1.1.2 Integrin CAMs

Whereas cadherins, lectin-CAM and IgSF introduced in the first chapter participate in cell-cell adhesion, the integrin family mediates cell-matrix interactions. Integrins are heterodimeric, composed of non-covalently associated α and β subunits (Figure 1.1). Humans have more than 18 α subtypes and 8 β subtypes generating totally 24 identified pairs of integrin heterodimers.[38, 39]

Here, we will focus on the integrins with β_3 subtypes, which consist only of the integrin $\alpha_v\beta_3$

and integrin $\alpha_{IIb}\beta_3$, specifically recognize the RGD tripeptide from different ECM proteins. Integrin $\alpha_v\beta_3$ expression is highly correlated with endothelial tumors and other cancers.[40] Integrin $\alpha_{IIb}\beta_3$ is the most abundant integrin on the platelet membrane, total $60,000 \sim 80,000$ per cell.[41] Although $\alpha_{IIb}\beta_3$ can bind to fibronectin and von Willebrand's factor, it serves as the primary fibrinogen receptor mediating platelet aggregation.[42] The structures of those two integrins have been successfully characterized which provides extensive information for investigating ligand-receptor interaction and the activation of integrins.

1.1.2.1 *β_3 integrin structure*

The two subunits of integrins are constructed from several domains linked by flexible linkers. Similar to the structure of other CAMs, each subunit contains a short cytoplasmic tail, a single transmembrane helix and a large ectodomain.[41, 43] The major breakthrough in understanding the extracellular domain of *β_3* integrins was from the crystal structure of $\alpha_v\beta_3$ and $\alpha_{IIb}\beta_3$ (Figure 1.2).[44-46] The α-chain contains four domains: a β-propeller, a thigh and two calf domains. The β-propeller can bind Ca^{2+}, which influences integrin ligand binding.[47] There is also a knee at the bend between the thigh and calf-1 domains, which allows the integrin molecule to adopt a bent conformation. The β-leg has seven domains: βI domain, hybrid domain, plexin-semaphorin-integrin (PSI) domain, and four epidermal growth factor (EGF) modules and a β-tail domain. The EGF1 and EGF2 domains (the β-knee) and the PSI/hybrid domain/EGF1 are relatively plastic, making the β-leg is overall more flexible than the α-leg.[48] The transmembrane segments have also been resolved for resting receptors.[49-52] The α unit is more perpendicular to

the membrane and the β_3 helix is tilted. There is also some electrostatic interaction at the helix-helix interface in order to increase packing interactions. It has also been proposed that binding of the talin leads to the dissociation of helix-helix clasp.[52, 53] The cytoplasmic domain is relatively short and less structurally confined, resulting in less consistent reports about their structure.[48]
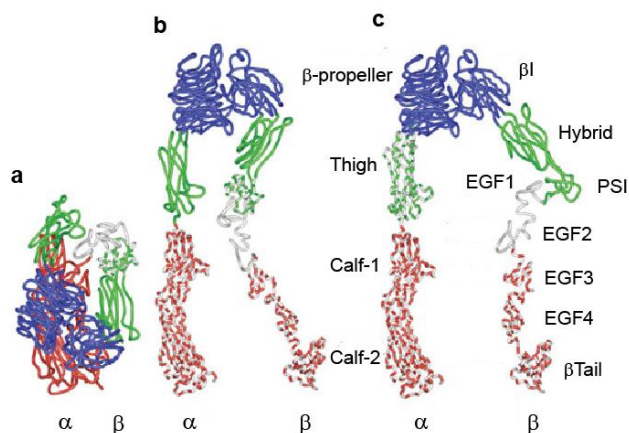
Figure 1.2 Integrin structure. (a-c) Three conformational states of platelet integrin $\alpha_{IIb}\beta_3$ visualized in electron microscopy and in crystal structures, reprinted from reference 46 with permission of the publisher.

1.1.2.2 Integrin conformational change and activation

The existence of several flexible points or "knees" in integrin structure allows integrins to adopt distinct conformations: closed or bent at the resting stage and extended in the active form.[44, 54, 55] In the bent conformation, the ligand binding head is folded close to the tail of the extracellular domain, positioning the ligand binding site near the membrane. When the $\alpha_v\beta_3$ integrin is complexed with a RGD peptide, it was also bent suggesting an active stage of integrin.[44, 45, 56] The authors of these two papers proposed a "deadbolt" model, which can regulate affinity for ligand in the absence of integrin extension.[57] According to this model, a small loop in

the β-tail domain interacts with βI domain and this interaction restricts the displacement of the βI domain, thus keeping the integrin in the low affinity state. However, this model was challenged by extensive experimental evidences. Site-mutation of the hairpin loop in the β_3 did not show any effect on the ligand binding for either $\alpha_{IIb}\beta_3$ or $\alpha_v\beta_3$ integrins.[58] Electron microscopy study demonstrated that Mn^{2+} triggers a completely extended conformation and this conformation was of high ligand binding affinity.[54]   In a FRET study, activation of integrin by Mn^{2+} showed a 5-nm distance increase from the membrane, suggesting an upright activated form.[59] Based on these observations, a second "switchblade" model was proposed that the headpiece of integrin bends down facing the membrane in the inactive conformation and projects upright once activated.[60] Although there is controversy about those two models, the "switchblade" model is now more widely accepted over the "deadbolt" one.

1.1.2.3 Integrin mechanotransduction

Understanding of integrin mechanotransduction starts with integrin activation. As discussed above, integrin activation involves an intramolecular conformational change from a bent conformation to an extended conformation. This structural change can be induced by either extracellular ("outside-in") and intracellular ("inside-out") signals.[61] Examples include the ligand binding by the extracellular head and talin binding at the β tail.[54, 62] More importantly, in molecular simulation, the application of force is sufficient to accelerate integrin activation process.[63] Direct activation of integrins by mechanical force has been shown for integrin $\alpha_5\beta_1$. Myosin force converts the integrins from a relaxed state to a tense state and this switch further generates phosphorylation signals.[64] These studies provide evidence that integrins serve as

mechanosensors and also suggest that integrins contribute to adhesion signaling pathways.

Once integrins are activated, they become the main physical linkage between the extracellular matrix and living cells by directly and indirectly coupling to the cytoskeleton. This process is also accompanied by integrin clustering into focal complexes and focal adhesions.[65-67] Similar to the bidirectional activation of integrins, the relationship between integrin-mediated adhesions and mechanical forces also functions in two directions. Cells apply forces to the matrix through those focal adhesion structures. In turn, formation of these structures requires tension from the cytoskeleton and the resistance from the substrates. Talin is the best-known linkage between the β integrin cytoplasmic domain and actin.[68] Integrin also binds to α-actinin, which binds to F-actin. Cytoskeletal forces transmitted through α-actinin drives adhesion maturation.[69] Transition into focal complexes also recruits paxillins and vinculins. Single molecule force microscopy showed that mechanical unfolding of talin exposes the cryptic site for vinculin binding.[70] Loss of cytoskeletal tension leads to the dissociation of vinculin from focal complexes, suggesting that force is necessary to maintain integrin focal complexes.[71] Single molecule fluorescence microscopy revealed that vinculins in focal adhesion transmit 2.5 pN force and that larger forces are associated with adhesion assembly.[72] Integrins also play a role in triggering signaling pathways upon application of tension, usually associated with signaling networks through focal adhesion kinase and Src-family protein tyrosine kinases.[73-75]

CAMs are critical structural and signaling proteins, participating in numerous cellular processes and responses, especially in the process of transducing physical cues. Although we discuss the four major types separately, cells usually employ several different CAMs to mediate

cell-cell adhesions and cell-ECM adhesion. One example is leukocytes transmigration from circulation into tissue.[76, 77] P-selectin-mediated rolling and capture of leukocytes on an endothelial blood vessel wall is the first step, followed by integrin activation on the leukocyte surface in order to form firm adhesion and spreading. VE-cadherins move away from endothelial cell junctions and facilitate the opening of endothelial cell junctions, allowing leukocytes migrating through the endothelium. PECAM-1 supports the final disconnection of leukocytes from endothelial cells and their passage through the basement membrane. Leukocytes migration shows high cooperativity between different CAMs.

1.2   *Methods for measuring cellular forces*

The cell adhesion molecules discussed above integrate physical cues from the extracellular matrix with fundamental cellular functions, such as cell migration, tissue development, differentiation and proliferation. They not only sense the forces from microenvironment, such as resistance forces from the substrates and shear stresses from blood flow, but also apply force generated by the myosin contraction to their microenvironments. In order to understand how mechanical forces impact biological processes, it is important to first measure them with high spatial and temporal resolution. Characterizing cellular forces at the single cell level remains challenging because of the dynamics of cellular processes. In addition, elucidating the interplay between mechanical force and cellular behaviors requires interdisciplinary expertise from both cell biology and biophysics. Advances in force microscopy over the past decade have revolutionized our understanding of mechanotransduction. This chapter will also introduce the techniques that are applied to understand integrin-based adhesions in cells at the single molecule

level.

1.2.1 Single cell force microcopy (SCFM)

This class of force measurements includes atomic force microscopy (AFM), optical tweezers, magnetic tweezers and biomembrane force probes (BFP).[78-85] These techniques have been widely used to measure forces of single ligand receptor bonds.[86, 87] Using AFM, the Zhu lab characterized the "catch-bond" behavior, an important noncovalent bond, for P-selectin with PSGL-1 and integrin $\alpha_5\beta_1$ with fibronectin.[24, 88] In contrast to a slip bond, a catch bond is a bond whose bond strength increases with applied forces. The existence of such catch bonds in a live cell system provides a possible mechanism for regulating cell adhesion under mechanical stress.

Instead of a measurement, SCFM techniques are more akin to manipulation techniques, in which the target (ligands and cell receptors or substrates and cells) were fixed on two ends of the probes-trapped beads, AFM tip or a surface. After the interaction or the bond formation between the two subjects, certain mechanical load is applied on this bond and the extension of the molecule or ligand-receptor behavior is determined and recorded from the position of the probe from its equilibrium position. Generally, these techniques are passive techniques that directly apply external force on cells and then monitor extension. Comparisons of the four methods are summarized in **Table 1.1**. In brief, AFM offers the greatest range of detection forces, which is usually used to measure the force of a cell detaching from its substrate. Tweezers and BFP are particularly useful to analyze cell receptor-ligand interaction with single molecule resolution.

Table 1.1 Comparison of four major single cell force microscopies.

	AFM	Magnetic Tweezers	Optical Tweezers	Fluorescence BFP
Force Range (pN)	10-10^4	0.01-100	0.1-100	1-100
Spatial Resolution (nm)	0.5-1	5-10	0.1-2	~ 3
Temporal Resolution (s)	10^{-3}	10^{-1}-10^{-2}	10^{-4}	10^{-3}
Reference	81, 82	83, 84	85, 86	87, 88

SCFM allows single receptor-ligand interactions to be examined in cellular environment ensuring the native state of the receptors. It is also capable identifying transient and rare events, which are ignored by ensemble measurements. The disadvantage of SCFM is that it is low-throughput and time-consuming as only one cell is tested every time. Another issue is that the attachment methods used to trap cells may affect its response, such as the cell shape change by aspiration in BFP measurement. The environment where the measurements are performed also impact the quality of the results, such as temperature stability, mechanical vibration and air flow.[86]

1.2.2 Traction force microscopy based on the substrate deformation
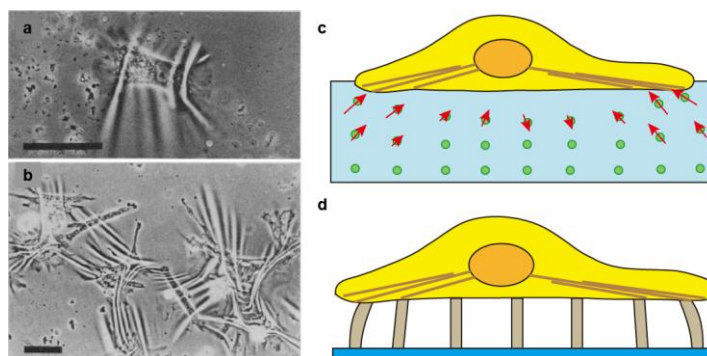
Figure 1.3 Examples and principles of the traction force microscopy. (a) An individual chick

heart fibroblast whose contractility wrinkled the silicone rubber substratum. Scale bar: 50 μm. (b) Lower magnification view of several chick heart fibroblasts and their distortions in the rubber substratum. Scale bar: 100 μm. Reprinted from reference 89 with permission of the publisher. (c) Schematic showing the principles of the traction force microscopy. Cells are seeded on an elastic gel which contains embedded beads. These beads serve as markers to visualize any deformation of the gel. When these cells start to contract, they deform the underlying substrate and cause the displacement of the beads. These displacements are used to calculated the contraction force. (d). Schematic showing the principle of the micropost array detector. Cell contractility bends the elastic pillars and this deformation can be converted into cell applied force.

Though adhesion molecules, cells are mechanically attached to the extracellular matrix. Cellular contraction force to the local environment is called cellular traction. If the substrate is soft, cellular traction forces deform the material, which can be recorded and quantified to estimate the loading (Figure 1.3 a and b).[89] Traction force microscopy (TFM) is designed based on this working mechanism. Generally, this technique requires an elastic substrate with well-defined mechanical properties, the measurement or recording of the material deformation to calculate the applied force.

The first type of TFM uses small fluorescent beads as markers to track the shape change of a polyacrylamide (PA) substrate.[90-92] The fluorescent beads are usually smaller than 1 μm and smaller than the size of the spread cells, resulting in subcellular spatial resolution. The PA polymer is the ideal material due to its superior optical and mechanical properties. PA gel is transparent, allowing a combination of TFM with fluorescence microscopy and this material is linearly elastic over a wide range of deformations. In a typical TFM experiment, the stiffness is controlled from 4 to 50 kPa for cells to spread and deform the material.[93] The PA gel also enables the ligand deposition by various crosslinking chemistry in order to support cell adhesions.

A second type of TFM technique is based on the concept of a micropost array detector

(mPAD). In this technique, elastic micropillars are fabricated in arrays on a 2D surface. The tops of these micropillars are coated with ECM protein, supporting cell spreading over multiple posts. The pattern of micropost arrays can be visualized by phase contrast or fluorescent labeling. The displacement of the pillars under cellular traction force can be determined from their vertical unstressed states, which are then used to calculate the force.

Both techniques have been widely used to characterize the focal adhesion formation and maturation, cell migration and differentiation in living cell.[90-92, 94-96] However, both methods possess their own limitations. First, the substrate stiffness in these experiments ranges from at least a few kPa, which is still higher than the physical stiffness of tissue (50 Pa-20 kPa).[97, 98] Second, the ECM protein deposition is a problem for both methods. Crosslinking PA gel with different stiffness affects the ligand density. mPADs also restrict cell adhesions to a specific topography, which may influence the distribution of the cellular forces. In addition, only one ECM molecule can be used in one experiments, which limits the further application to study the crosstalk between multiple CAMs. Last but not the least, those two methods also have limited spatial resolutions. The bead size and micropost dimensions and their mechanical properties determine their measurements at the unit of focal adhesions.

1.2.3 FRET based molecular tension probes

TFM and mPADs have provided sub-focal adhesion resolution (as low as 500 nm) and revealed that the force distribution is highly heterogeneous within single focal adhesion.[92, 99] As focal adhesions are comprised of hundreds of individual integrins, it is highly desirable to directly measure the force at single receptors, since this would provide the necessary information needed

to reconstruct the tension map of the focal adhesion across entire cells.

The tension experienced by individual integrin receptors has been estimated at around a few piconewtons (pN) to one hundred pN.[24, 88, 100] To measure the forces through single membrane receptors, new methods are needed with pN force sensitivity.

1.2.3.1 Mechanism of Förster resonance energy transfer (FRET)

FRET is a widely used technique to report changes in structure and dynamics of biomolecules at nanometer distance.[101-103] The FRET efficiency is determined as (1)

$$E = \frac{R_0^6}{[R_0^6 + r^6]} = 1 - \frac{I_{DA}}{I_D} \qquad (1)$$

where r is the donor-acceptor distance, R_0 is the characteristic distance where the efficiency of energy transfer is 50%, I_{DA} is the fluorescence intensity of the donor with the acceptor and I_D is the intensity of the donor without the acceptor. Each donor-acceptor pair has its unique R_0 value, which can be experimentally determined or theoretically calculated.[104-106] With the R_0 and the fluorescence intensity measured experimentally, distance changes at the molecular level can be extracted to ultimately calculate receptor forces. Overall, the requirements for a FRET based tension sensor are:

(1) a fluorescent donor that is in proximity to a quencher or acceptor,

(2) a molecular "spring" that is extended under force,

(3) a pre-determined relationship between the mechanical load and extension of the spring.

The choice of fluorescent pair and the spring affects the dynamic force range of the FRET tension probe system by determining the extension of the linker and the fluorescence signal collected with or without force.

1.2.3.2 Genetically encoded FRET tension sensors

Genetically encoded FRET tension sensors are engineered protein complexes in which a flexible peptide linker is inserted between a pair of fluorescent proteins that undergo FRET. As this whole sensor system is protein based, it can be genetically fused into a protein of interest. The insertion site is chosen at the region where the target protein function can still be maintained and a sharp FRET efficiency change responds to the force loading. Typically, more than 20 final constructs are designed and tested to identify the optimal probe. Protocols have been published with detailed instructions of designing such sensors.[107, 108] With a successful construct, force transmitted through the interested proteins can be visualized by measuring fluorescence or fluorescence lifetime.

The first reported genetically encoded tension probe was designed with Cerulean and Venus fluorescent proteins separated by a 5 nm α-helix.[109] It was inserted into spectrin, α-actin and filamin A and expressed in cultured cells. This sensor showed that the trailing edge of the cell displays lower force. This α-helix sensor was further calibrated and the dynamic range was reported to be 5-7 pN.[110, 111]
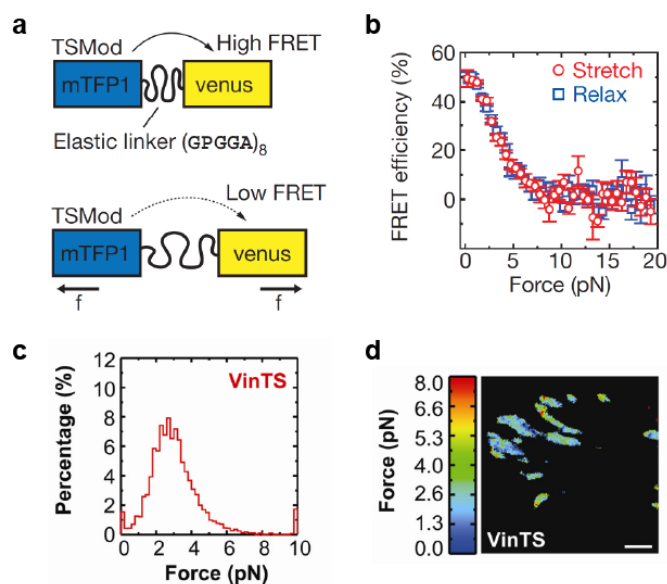
Figure 1.4 Vinculin tension sensor constructs. (a) The tension sensor module consists of two fluorophores separated by a (GPGGA)8 linker. Force (f) across TSMod extends the elastic linker, resulting in decreased FRET efficiency. (b) Averaged FRET–force curves from TSMod show reversible stretching and relaxing between 0.25 and 19 pN. (c) Force distribution across vinculin tension sensor (VinTS) in FAs. (d) The average force per vinculin measured by TSMod. Reprinted from reference 72 with permission of the publisher.

Grashoff et al. designed a tension sensor module (TSMod) with the mTFP-1 and Venus donor-acceptor pair and (GPGGA)$_8$ elastic linker to measure vinculin tension (Figure 1.4).[72] The key point in this work was that they used optical tweezer and single-molecule fluorescence microscopy techniques to calibrate this 40-amino acid linker. The dynamic range for this sensor was reported from 0 to 10 pN and the force transmitted through vinculin was about 2.5 pN. This TsMod design has been adopted by many research groups to study other cell adhesion molecules, such as E-cadherin, VE-cadherin, and PECAM-1.[35, 112, 113] TSMod was also used to characterize the compression of the glycocalyx and the effect of the glycocalyx compression on integrin activation in cancer cells.[114]

The limitations of this genetically encoded tension sensor should also be noted. First, this

type of tension sensor is sensitive to forces less than 10 pN. This is determined by the FRET

efficiency of fluorescent protein pairs and the peptide mechanical properties. The typical R_0 for

such fluorescent protein FRET pairs is 5-6 nm, suggesting that accurate measurements of distance

displacement from 3 to 8 nm.[115] Single molecule experiments using tweezers revealed that the

forces needed to unfold small protein domains are around 5-30 pN, which is also loading

rate-dependent.[116-118] The combination of these factors, implies that genetically encoded tension

sensors are only suitable to measure forces that are less than 10 pN. Second, as fluorescence

images are acquired and analyzed, other factors, such as cellular autofluorescence, affect the

signal intensities.
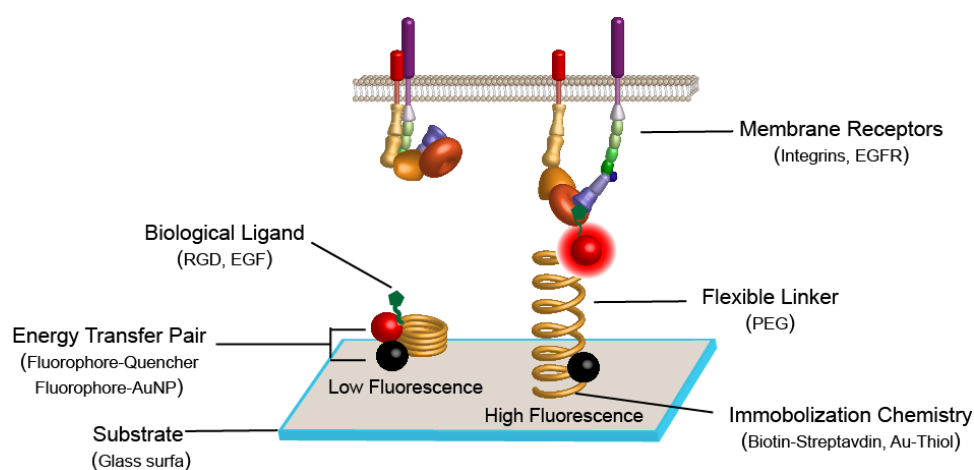
Figure 1.5   Schematic of surface immobilized FRET tension sensors.

1.2.3.3 Surface immobilized FRET tension sensors

Our lab and others have developed the surface immobilized FRET tension sensor, allowing

the measurement of force between cell membrane receptors and their extracellular matrix ligands.

Surfaces decorated with these tension sensors serve as molecular reporters of receptor forces as

cells adhere, spread and migrate. When CAMs associate with those tension probes, fluorescence

signal increases to report the applied forces.

Probes for molecular tension-based fluorescence microscopy (MTFM) require a flexible linker with defined mechanical properties, a biological ligand that interacts with cell membrane receptors and a donor-acceptor/quencher pair that reports the displacement of the linker caused by applied forces (Figure 1.5).
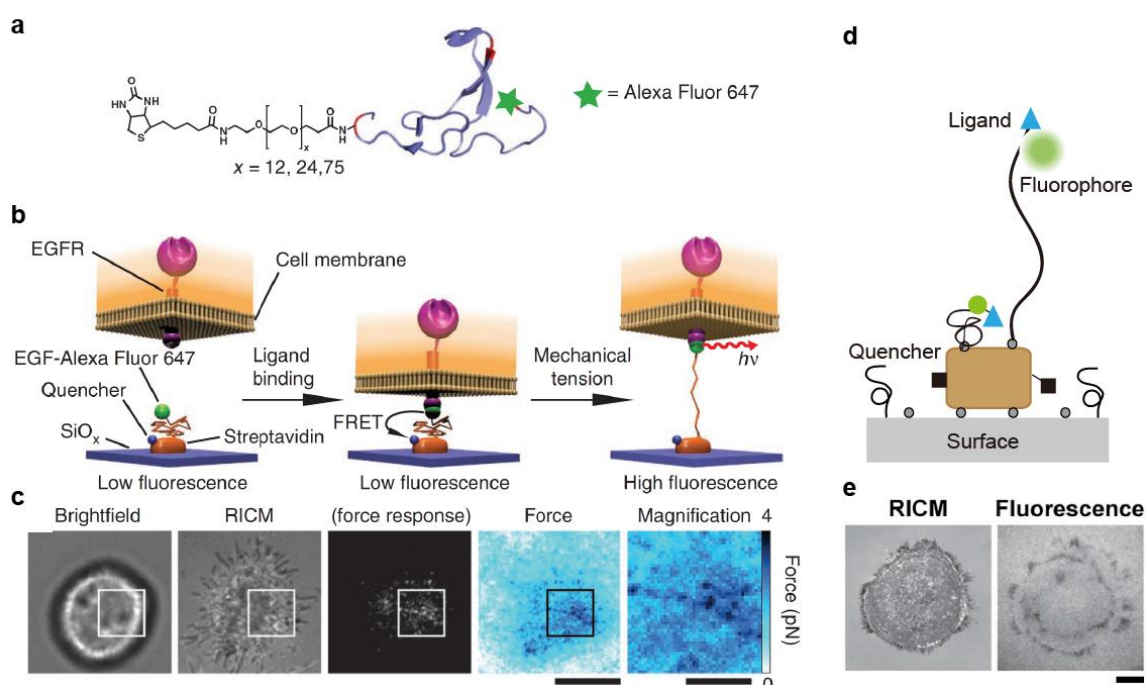
Figure 1.6 The principles and applications of the initial PEG-based MTFM probes. (a) Schematic of the EGF-PEG$_{24}$ tension sensor, comprised of a PEG polymer flanked by Alexa Fluor 647 EGF ligand and a biotin for surface immobilization. (b) Schematic of the mechanism of sensor function. When EGFR exerts a force on its ligand, the flexible PEG linker extends. The displacement of the EGF ligand results in an increase in the measured fluorescence intensity, thus reporting the transmission of mechanical tension through the EGF-EGFR complex. hv, emission of a photon. (c) Representative brightfield, RICM and fluorescence response for a cell engaged to an EGF-PEG$_{24}$ force sensor surface. The sensor fluorescence response was converted into a force map by using the extended WLC model for PEG$_{24}$. (d) Schematic of the MTFM integrin force sensor, which is composed of a PEG polymer flanked by a peptide and the Alexa 647 at one terminus, and a quencher-modified streptavidin protein at the other terminus. (e) A decrease in donor signal is observed under the cell perimeter with the construct in (d), suggesting the detachment of the sensor from the surface. Reprinted from reference 119 and 125 with permission of the publisher. Scale bars=10 μm for all the images.

The very initial design of this MTFM probe was published by Stabley et al. in 2011, and was used to visualize the mechanical forces involved in the early stages of endocytosis of the ligand-activated epidermal growth factor receptor (EGFR) (Figure 1.6 a, b and c).[119] The sensor consists of a flexible PEG linker that is covalently conjugated to a EGF ligand at one terminus and the other end is anchored onto a glass slide through a biotin-streptavidin interaction, the most stable non-covalent interaction to ensure that mechanical forces do not result in sensor translocation. The linker is comprised of a polyethylene glycol (PEG) polymer because of its unique properties that include: (1) well-documented and reversible force-extension curves, (2) high biocompatibility and (3) low nonspecific interactions with other biomolecules.[120-123] The Alexa 647-labeled ligand and QSY21-labeled streptavidin serve as fluorophore and quencher molecules that undergo FRET. Cellular forces exerted on the EGF ligand extend the PEG molecule from its relaxed conformation and pull the fluorophore away from the quencher, generating an increased fluorescence intensity. The fluorescent signals are further converted into r in equation (1) and this displacement is used to estimate the mechanical tension using the extended worm-like chain (WLC) model.[120, 121, 124] With such a design, Stabley and coworkers created the first mechanical tension map of EGFR endocytosis. The map revealed a peak force value of approximately 4 pN.

Another sensor based on this initial design was also developed to target the integrin membrane receptor (Figure 1.6 d and e).[125] Cyclic Arg-Gly-Asp-D-Phe-Lys(Cys) (cRGDfK(C)) peptide was coupled with Alexa 647-NHS ester and then with biotin-PEG$_{23}$ through maleimide-thiol crosslinking chemistry. Streptavidin was modified with quencher as well to

quench the fluorescence signal when the sensor is relaxed and to immobilize the whole sensor onto a glass surface. Unexpectedly, the fluorescence signal intensity under the perimeter of most cells was negative. Further experiments indicated that under these conditions biotinylated PEG tension probes were dissociated from the surface. Their observation was surprising given that the streptavidin-biotin interaction is often described as the strongest noncovalent association in nature.[126, 127] Based on their observation, they concluded that integrin-ligand tension is likely to be underestimated using microscopic averaging methods.[128] The estimated force derived from this experiment and calculations should around ~10-20 pN per integrin.

The second generation of the MTFM tension probes utilized a different energy transfer mechanism called nanometal surface energy transfer (NSET).[129] Compared with FRET, energy transfer to a metallic surface follows a very different distance trend and magnitude of interaction (Equation (2)). Compared to molecular quenchers, the effective quenching distance of AuNPs can be as long as several tens of nanometers (Figure 1.7).[130]

$$\text{E} = \frac{d_0^4}{[d_0^4 + r^4]} = 1 - \frac{I_{DA}}{I_D} \qquad (2)$$

Liu et al. targeted the $\alpha_v\beta_3$ integrins using cRGDfK(C), because integrins are the primary CAMs to sustain large force (breaking the biotin-streptavidin interaction) to support cell adhesion and migration.[131, 132] Peptide ligand with a fluorophore was coupled to one end of the PEG linker through click reaction and the other end of the PEG linker was immobilized onto the AuNP by thiol-Au interaction. The sensors were fully calibrated with d_0 of 13.6 nm for Alexa 488 quenched by 10 nm diameter AuNP and 14.5 nm for Cy3B quenched by 9 nm diameter AuNP. For the Cy3B and 9 nm AuNP pair, a force dynamic range that saturated at 27 pN was estimated,

assuming the ability to detect quenching efficiency values from 10 to 90%. This estimate of dynamic range is based on the 14.5 nm NSET radius and the predicted WLC model of PEG_{80}. With such MTFM probes, they reported integrin tension values ranging from 1 to 15 pN.[125] The effect of ligand spacing was also investigated with the combination of MTFM with fabricated nanoarrays of precisely spaced AuNP probes. In these studies, it was concluded that the mechanism of sensing ligand spacing was force-mediated.[132]
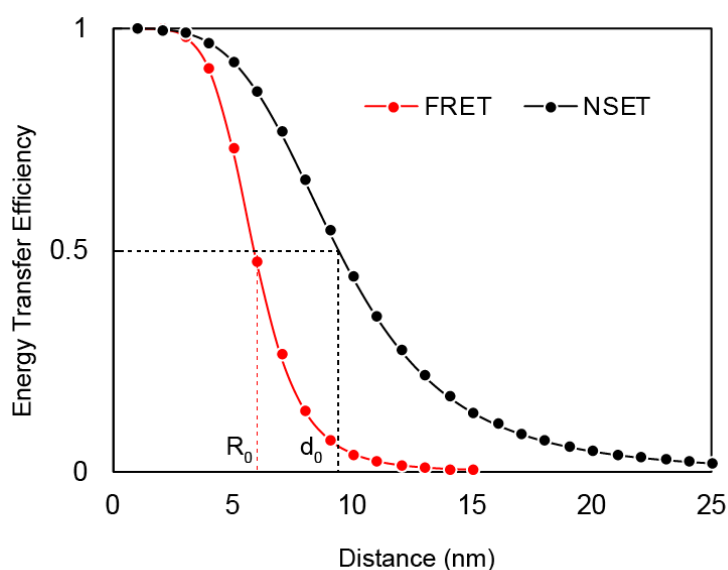
Figure 1.7 Comparison of the experimental energy transfer efficiency values with the theoretical energy transfer efficiency curves for FRET and NSET process. The Förster radius (R_0) is 5.9 nm, while the SET radius (d_0) is 9.4 nm. Data is regenerated from reference 129 with permission of the publisher.

Other groups also developed similar surface immobilized molecular tension probes, which are based on the $(GPGGA)_8$ peptide and biotin-streptavidin interaction.[133] By diluting the sensor density on the glass substrate to 0.5 labeled tension probe per μm^2, single-molecule FRET experiment was performed and the measurement of absolute extension from single tension probe was achieved, avoiding the ensemble averaging problems. However, single molecule

measurements introduce other challenges due to the need for O_2 scavengers and the scarcity of reporters.

1.3 Aims of the dissertation

Current force microscopy techniques have greatly improved our capability of studying cellular forces within living cells. TFM offers a robust system to track the mechanical tension at the single cell level for experiments spanning over several days.[134, 135] MTFM probes target single receptors and provide spatial and force resolution at the molecular level. Chang et al also demonstrated that MTFM can support more than 60 hr of cellular tension measurements.[136] One of the remaining challenges for these techniques is that they report an ensemble averaged force value. The current solution to solving this problem is to use single-molecule fluorescence microscopy with a sparse density of tension probes, which loses much of the rich details associated with thousands of adhesion receptors that are collectively working together. [133] Therefore, new methods are needed that can directly report forces independent of the density of stressed sensors. MTFM also offers the ability to characterize forces alongwith downstream biochemical signals simultaneously, which allows correlation between tension and cellular events.

There are still many questions yet to be answered and this thesis aims to provide new technical platforms with broad applications in the field of CAMs mediated mechanotransduction, specially aiming to understand the role of β_3 integrins. The key questions that will be addressed include:

- How can a MTFM probes report a force without ensemble averaging?

- How do β_3 integrin forces control different signaling pathways in cell adhesion and platelet function?

- How do the mechanical properties (for example, lateral mobility) of ligand molecules affect integrin activation?

- What is the role of mechanical force in integrin activation?

1.4   References

1.   Klein-Nulend, J., Bacabac, R.G. & Bakker, A.D. Mechanical Loading and How It Affects Bone Cells: The Role of the Osteocyte Cytoskeleton in Maintaining Our Skeleton. *Eur Cells Mater* **24**, 278-291 (2012).

2.   Han, M.K. & de Rooij, J. Converging and Unique Mechanisms of Mechanotransduction at Adhesion Sites. *Trends Cell Biol* (2016).

3.   Ingber, D.E. Cellular mechanotransduction: putting all the pieces together again. *Faseb J* **20**, 811-827 (2006).

4.   Polacheck, W.J. & Chen, C.S. Measuring cell-generated forces: a guide to the available tools. *Nat Methods* **13**, 415-423 (2016).

5.   Lodish, H. *et al*. Molecular Cell Biology, Edn. 4th (New York: W. H. Freeman; 2000).

6.   Albelda, S.M. & Buck, C.A. Integrins and other cell adhesion molecules. *Faseb J* **4**, 2868-2880 (1990).

7.   Gumbiner, B.M. Regulation of cadherin-mediated adhesion in morphogenesis. *Nat Rev Mol Cell Biol* **6**, 622-634 (2005).

8.   Hirano, S. & Takeichi, M. Cadherins in brain morphogenesis and wiring. *Physiol Rev* **92**, 597-634 (2012).

9.   Jeanes, A., Gottardi, C.J. & Yap, A.S. Cadherins and cancer: how does cadherin dysfunction promote tumor progression? *Oncogene* **27**, 6920-6929 (2008).

10.   Takeichi, M. Cadherins in cancer: implications for invasion and metastasis. *Curr Opin Cell Biol* **5**, 806-811 (1993).

11.   van Roy, F. & Berx, G. The cell-cell adhesion molecule E-cadherin. *Cell Mol Life Sci* **65**, 3756-3788 (2008).

12.   Pokutta, S. & Weis, W.I. Structure and mechanism of cadherins and catenins in cell-cell contacts. *Annu Rev Cell Dev Biol* **23**, 237-261 (2007).

13.   Chu, Y.S. *et al.* Force measurements in E-cadherin-mediated cell doublets reveal rapid adhesion strengthened by actin cytoskeleton remodeling through Rac and Cdc42. *J Cell Biol* **167**, 1183-1194 (2004).

14.   Wijnhoven, B.P., Dinjens, W.N. & Pignatelli, M. E-cadherin-catenin cell-cell adhesion complex and human cancer. *Br J Surg* **87**, 992-1005 (2000).

15.   le Duc, Q. *et al.* Vinculin potentiates E-cadherin mechanosensing and is recruited to actin-anchored sites within adherens junctions in a myosin II-dependent manner. *J Cell Biol* **191**, 891-891 (2010).

16.   Bajpai, S., Feng, Y.F., Krishnamurthy, R., Longmore, G.D. & Wirtz, D. Loss of alpha-Catenin Decreases the Strength of Single E-cadherin Bonds between Human Cancer Cells. *J Biol Chem* **284**, 18252-18259 (2009).

17. Buckley, C.D. *et al.* Cell adhesion. The minimal cadherin-catenin complex binds to actin filaments under force. *Science* **346**, 1254211 (2014).

18. Cambi, A. & Figdor, C.G. Dual function of C-type lectin-like receptors in the immune system. *Curr Opin Cell Biol* **15**, 539-546 (2003).

19. Blann, A.D., Nadar, S.K. & Lip, G.Y. The adhesion molecule P-selectin and cardiovascular disease. *Eur Heart J* **24**, 2166-2179 (2003).

20. McEver, R.P., Moore, K.L. & Cummings, R.D. Leukocyte trafficking mediated by selectin-carbohydrate interactions. *J Biol Chem* **270**, 11025-11028 (1995).

21. Moore, K.L. *et al.* P-selectin glycoprotein ligand-1 mediates rolling of human neutrophils on P-selectin. *J Cell Biol* **128**, 661-671 (1995).

22. Fritz, J., Katopodis, A.G., Kolbinger, F. & Anselmetti, D. Force-mediated kinetics of single P-selectin/ligand complexes observed by atomic force microscopy. *Proc Natl Acad Sci USA* **95**, 12283-12288 (1998).

23. Alon, R., Hammer, D.A. & Springer, T.A. Lifetime of the P-selectin-carbohydrate bond and its response to tensile force in hydrodynamic flow. *Nature* **374**, 539-542 (1995).

24. Marshall, B.T. *et al.* Direct observation of catch bonds involving cell-adhesion molecules. *Nature* **423**, 190-193 (2003).

25. Sarangapani, K.K. *et al.* Low force decelerates L-selectin dissociation from P-selectin glycoprotein ligand-1 and endoglycan. *J Biol Chem* **279**, 2291-2298 (2004).

26. Dermody, T.S., Kirchner, E., Guglielmi, K.M. & Stehle, T. Immunoglobulin superfamily virus receptors and the evolution of adaptive immunity. *PLoS Pathog* **5**, e1000481

(2009).

27. Brummendorf, T. & Lemmon, V. Immunoglobulin superfamily receptors: cis-interactions, intracellular adapters and alternative splicing regulate adhesion. *Curr Opin Cell Biol* **13**, 611-618 (2001).

28. Miyahara, M. *et al.* Interaction of nectin with afadin is necessary for its clustering at cell-cell contact sites but not for its cis dimerization or trans interaction. *J Biol Chem* **275**, 613-618 (2000).

29. Newman, P.J. & Newman, D.K. Signal transduction pathways mediated by PECAM-1: new roles for an old molecule in platelet and vascular cell biology. *Arterioscler Thromb Vasc Biol* **23**, 953-964 (2003).

30. Ilan, N. & Madri, J.A. PECAM-1: old friend, new partners. *Curr Opin Cell Biol* **15**, 515-524 (2003).

31. Privratsky, J.R., Newman, D.K. & Newman, P.J. PECAM-1: conflicts of interest in inflammation. *Life Sci* **87**, 69-82 (2010).

32. Osawa, M., Masuda, M., Harada, N., Lopes, R.B. & Fujiwara, K. Tyrosine phosphorylation of platelet endothelial cell adhesion molecule-1 (PECAM-1, CD31) in mechanically stimulated vascular endothelial cells. *Eur J Cell Biol* **72**, 229-237 (1997).

33. Osawa, M., Masuda, M., Kusano, K. & Fujiwara, K. Evidence for a role of platelet endothelial cell adhesion molecule-1 in endothelial cell mechanosignal transduction: is it a mechanoresponsive molecule? *J Cell Biol* **158**, 773-785 (2002).

34. Tzima, E. *et al.* A mechanosensory complex that mediates the endothelial cell response to

fluid shear stress. *Nature* **437**, 426-431 (2005).

35.   Conway, D.E. *et al.* Fluid shear stress on endothelial cells modulates mechanical tension

across VE-cadherin and PECAM-1. *Curr Biol* **23**, 1024-1030 (2013).

36.   Conway, D.E. & Schwartz, M.A. Mechanotransduction of shear stress occurs through

changes in VE-cadherin and PECAM-1 tension: implications for cell migration. *Cell Adh*

Migr **9**, 335-339 (2015).

37.   Collins, C. *et al.* Localized tensional forces on PECAM-1 elicit a global

mechanotransduction response via the integrin-RhoA pathway. *Curr Biol* **22**, 2087-2094

(2012).

38.   Humphries, J.D., Byron, A. & Humphries, M.J. Integrin ligands at a glance. *J Cell Sci*

119, 3901-3903 (2006).

39.   Barczyk, M., Carracedo, S. & Gullberg, D. Integrins. *Cell Tissue Res* **339**, 269-280

(2010).

40.   Danhier, F., Le Breton, A. & Preat, V. RGD-based strategies to target alpha(v) beta(3)

integrin in cancer therapy and diagnosis. *Mol Pharm* **9**, 2961-2973 (2012).

41.   Bennett, J.S., Berger, B.W. & Billings, P.C. The structure and function of platelet

integrins. *J Thromb Haemost* **7 Suppl 1**, 200-205 (2009).

42.   Ma, Y.Q., Qin, J. & Plow, E.F. Platelet integrin alpha(IIb)beta(3): activation mechanisms.

J Thromb Haemost **5**, 1345-1352 (2007).

43.   Arnaout, M.A., Goodman, S.L. & Xiong, J.P. Structure and mechanics of integrin-based

cell adhesion. *Curr Opin Cell Biol* **19**, 495-507 (2007).

44.   Xiong, J.P. *et al.* Crystal structure of the extracellular segment of integrin alpha Vbeta3. *Science* **294**, 339-345 (2001).

45.   Xiong, J.P. *et al.* Crystal structure of the extracellular segment of integrin alpha Vbeta3 in complex with an Arg-Gly-Asp ligand. *Science* **296**, 151-155 (2002).

46.   Xiao, T., Takagi, J., Coller, B.S., Wang, J.H. & Springer, T.A. Structural basis for allostery in integrins and binding to fibrinogen-mimetic therapeutics. *Nature* **432**, 59-67 (2004).

47.   Humphries, M.J., Symonds, E.J. & Mould, A.P. Mapping functional residues onto integrin crystal structures. *Curr Opin Struct Biol* **13**, 236-243 (2003).

48.   Campbell, I.D. & Humphries, M.J. Integrin structure, activation, and interactions. *Cold Spring Harb Perspect Biol* **3** (2011).

49.   Wegener, K.L. & Campbell, I.D. Transmembrane and cytoplasmic domains in integrin activation and protein-protein interactions (review). *Mol Membr Biol* **25**, 376-387 (2008).

50.   Lau, T.L., Dua, V. & Ulmer, T.S. Structure of the integrin alphaIIb transmembrane segment. *J Biol Chem* **283**, 16162-16168 (2008).

51.   Lau, T.L., Partridge, A.W., Ginsberg, M.H. & Ulmer, T.S. Structure of the integrin beta3 transmembrane segment in phospholipid bicelles and detergent micelles. *Biochemistry* **47**, 4008-4016 (2008).

52.   Zhu, J. *et al.* The structure of a receptor with two associating transmembrane domains on the cell surface: integrin alphaIIbbeta3. *Mol Cell* **34**, 234-249 (2009).

53.   Yang, J. *et al.* Structure of an integrin alphaIIb beta3 transmembrane-cytoplasmic

heterocomplex provides insight into integrin activation. *Proc Natl Acad Sci USA* **106**, 17729-17734 (2009).

54. Takagi, J., Petre, B.M., Walz, T. & Springer, T.A. Global conformational rearrangements in integrin extracellular domains in outside-in and inside-out signaling. *Cell* **110**, 599-511 (2002).

55. Parise, L.V., Helgerson, S.L., Steiner, B., Nannizzi, L. & Phillips, D.R. Synthetic peptides derived from fibrinogen and fibronectin change the conformation of purified platelet glycoprotein IIb-IIIa. *J Biol Chem* **262**, 12597-12602 (1987).

56. Adair, B.D. *et al.* Three-dimensional EM structure of the ectodomain of integrin {alpha}V{beta}3 in a complex with fibronectin. *J Cell Biol* **168**, 1109-1118 (2005).

57. Xiong, J.P., Stehle, T., Goodman, S.L. & Arnaout, M.A. New insights into the structural basis of integrin activation. *Blood* **102**, 1155-1159 (2003).

58. Zhu, J., Boylan, B., Luo, B.H., Newman, P.J. & Springer, T.A. Tests of the extension and deadbolt models of integrin activation. *J Biol Chem* **282**, 11914-11920 (2007).

59. Chigaev, A., Buranda, T., Dwyer, D.C., Prossnitz, E.R. & Sklar, L.A. FRET detection of cellular alpha4-integrin conformational activation. *Biophys J* **85**, 3951-3962 (2003).

60. Takagi, J. & Springer, T.A. Integrin activation and structural rearrangement. *Immunol Rev* **186**, 141-163 (2002).

61. Hynes, R.O. Integrins: bidirectional, allosteric signaling machines. *Cell* **110**, 673-687 (2002).

62. Tadokoro, S. *et al.* Talin binding to integrin beta tails: a final common step in integrin

activation. *Science* **302**, 103-106 (2003).

63.   Puklin-Faucher, E., Gao, M., Schulten, K. & Vogel, V. How the headpiece hinge angle is

opened: new insights into the dynamics of integrin activation. *J Cell Biol* **175**, 349-360

(2006).

64.   Friedland, J.C., Lee, M.H. & Boettiger, D. Mechanically activated integrin switch

controls alpha5beta1 function. *Science* **323**, 642-644 (2009).

65.   Cavalcanti-Adam, E.A. *et al.* Cell spreading and focal adhesion dynamics are regulated

by spacing of integrin ligands. *Biophys J* **92**, 2964-2974 (2007).

66.   Selhuber-Unkel, C., Lopez-Garcia, M., Kessler, H. & Spatz, J.P. Cooperativity in

adhesion cluster formation during initial cell adhesion. *Biophys J* **95**, 5424-5431 (2008).

67.   Liu, Y. *et al.* Nanoparticle Tension Probes Patterned at the Nanoscale: Impact of Integrin

Clustering on Force Transmission. *Nano Lett* **14**, 5539-5546 (2014).

68.   Puklin-Faucher, E. & Sheetz, M.P. The mechanical integrin cycle. *J Cell Sci* **122**, 179-186

(2009).

69.   Roca-Cusachs, P. *et al.* Integrin-dependent force transmission to the extracellular matrix

by alpha-actinin triggers adhesion maturation. *Proc Natl Acad Sci USA* **110**, E1361-1370

(2013).

70.   del Rio, A. *et al.* Stretching single talin rod molecules activates vinculin binding. *Science*

323, 638-641 (2009).

71.   Galbraith, C.G., Yamada, K.M. & Sheetz, M.P. The relationship between force and focal

complex development. *J Cell Biol* **159**, 695-705 (2002).

72. Grashoff, C. *et al.* Measuring mechanical tension across vinculin reveals regulation of focal adhesion dynamics. *Nature* **466**, 263-266 (2010).

73. Reedquist, K.A. *et al.* The small GTPase, Rap1, mediates CD31-induced integrin adhesion. *J Cell Biol* **148**, 1151-1158 (2000).

74. Harburger, D.S. & Calderwood, D.A. Integrin signalling at a glance. *J Cell Sci* **122**, 159-163 (2009).

75. Widmaier, M., Rognoni, E., Radovanac, K., Azimifar, S.B. & Fassler, R. Integrin-linked kinase at a glance. *J Cell Sci* **125**, 1839-1843 (2012).

76. Vestweber, D. How leukocytes cross the vascular endothelium. *Nat Rev Immunol* **15**, 692-704 (2015).

77. Vestweber, D. Control of Leukocyte Extravasation and Vascular Permeability by Endothelial Junctions. *J Vasc Res* **52**, 83-83 (2015).

78. Li, F., Redick, S.D., Erickson, H.P. & Moy, V.T. Force measurements of the alpha5beta1 integrin-fibronectin interaction. *Biophys J* **84**, 1252-1262 (2003).

79. Sun, Z. *et al.* Mechanical properties of the interaction between fibronectin and alpha(5)beta(1)-integrin on vascular smooth muscle cells studied using atomic force microscopy. *Am J Physiol-Heart C* **289**, H2526-H2535 (2005).

80. Matthews, B.D., Overby, D.R., Mannix, R. & Ingber, D.E. Cellular adaptation to mechanical stress: role of integrins, Rho, cytoskeletal tension and mechanosensitive ion channels. *J Cell Sci* **119**, 508-518 (2006).

81. Roca-Cusachs, P., Gauthier, N.C., del Rio, A. & Sheetz, M.P. Clustering of alpha(5)beta(1)

integrins determines adhesion strength whereas alpha(v)beta(3) and talin enable mechanotransduction. *P Natl Acad Sci USA* **106**, 16245-16250 (2009).

82.   Schwingel, M. & Bastmeyer, M. Force mapping during the formation and maturation of cell adhesion sites with multiple optical tweezers. *PLoS One* **8**, e54850 (2013).

83.   Jiang, G.Y., Giannone, G., Critchley, D.R., Fukumoto, E. & Sheetz, M.P. Two-piconewton slip bond between fibronectin and the cytoskeleton depends on talin. *Nature* **424**, 334-337 (2003).

84.   Kong, F. *et al.* Cyclic Mechanical Reinforcement of Integrin-Ligand Interactions. *Molecular Cell* **49**, 1060-1068 (2013).

85.   Chen, W., Lou, J., Evans, E.A. & Zhu, C. Observing force-regulated conformational changes and ligand dissociation from a single integrin on cells. *J Cell Biol* **199**, 497-512 (2012).

86.   Neuman, K.C. & Nagy, A. Single-molecule force spectroscopy: optical tweezers, magnetic tweezers and atomic force microscopy. *Nat Methods* **5**, 491-505 (2008).

87.   Chen, Y. *et al.* Fluorescence Biomembrane Force Probe: Concurrent Quantitation of Receptor-ligand Kinetics and Binding-induced Intracellular Signaling on a Single Cell. *J Vis Exp*, e52975 (2015).

88.   Kong, F., Garcia, A.J., Mould, A.P., Humphries, M.J. & Zhu, C. Demonstration of catch bonds between an integrin and its ligand. *J Cell Biol* **185**, 1275-1284 (2009).

89.   Harris, A.K., Wild, P. & Stopak, D. Silicone rubber substrata: a new wrinkle in the study of cell locomotion. *Science* **208**, 177-179 (1980).

90. Beningo, K.A., Dembo, M., Kaverina, I., Small, J.V. & Wang, Y.L. Nascent focal adhesions are responsible for the generation of strong propulsive forces in migrating fibroblasts. *J Cell Biol* **153**, 881-888 (2001).

91. Dembo, M. & Wang, Y.L. Stresses at the cell-to-substrate interface during locomotion of fibroblasts. *Biophys J* **76**, 2307-2316 (1999).

92. Plotnikov, S.V., Pasapera, A.M., Sabass, B. & Waterman, C.M. Force fluctuations within focal adhesions mediate ECM-rigidity sensing to guide directed cell migration. *Cell* **151**, 1513-1527 (2012).

93. Plotnikov, S.V., Sabass, B., Schwarz, U.S. & Waterman, C.M. in Methods in Cell Biology, Vol. 123 (2014).

94. Balaban, N.Q. *et al.* Force and focal adhesion assembly: a close relationship studied using elastic micropatterned substrates. *Nat Cell Biol* **3**, 466-472 (2001).

95. Yang, M.T., Fu, J., Wang, Y.K., Desai, R.A. & Chen, C.S. Assaying stem cell mechanobiology on microfabricated elastomeric substrates with geometrically modulated rigidity. *Nat Protoc* **6**, 187-213 (2011).

96. Fu, J. *et al.* Mechanical regulation of cell function with geometrically modulated elastomeric substrates. *Nat Methods* **7**, 733-736 (2010).

97. Wells, R.G. The role of matrix stiffness in regulating cell behavior. *Hepatology* **47**, 1394-1400 (2008).

98. Haage, A. & Schneider, I.C. Cellular contractility and extracellular matrix stiffness regulate matrix metalloproteinase activity in pancreatic cancer cells. *FASEB J* **28**,

3589-3599 (2014).

99.   Sabass, B., Gardel, M.L., Waterman, C.M. & Schwarz, U.S. High resolution traction force microscopy based on experimental and computational advances. *Biophys J* **94**, 207-220 (2008).

100.   Agnihotri, A., Soman, P. & Siedlecki, C.A. AFM measurements of interactions between the platelet integrin receptor GPIIbIIIa and fibrinogen. *Colloids Surface B* **71**, 138-147 (2009).

101.   Wang, K. *et al.* Molecular engineering of DNA: molecular beacons. *Angew Chem Int Ed Engl* **48**, 856-870 (2009).

102.   Heyduk, T. Measuring protein conformational changes by FRET/LRET. *Curr Opin Biotechnol* **13**, 292-296 (2002).

103.   Ermolenko, D.N. *et al.* Observation of intersubunit movement of the ribosome in solution using FRET. *J Mol Biol* **370**, 530-540 (2007).

104.   Piston, D.W. & Kremers, G.J. Fluorescent protein FRET: the good, the bad and the ugly. *Trends Biochem Sci* **32**, 407-414 (2007).

105.   Thermofisher (https://www.thermofisher.com/us/en/home/references/molecular-probes-the-handbook/tables/r0-values-for-some-alexa-fluor-dyes.html).

106.   Atto-tec.com   (http://www.atto-tec.com/index.php?id=65&L=1).

107.   LaCroix, A.S., Rothenberg, K.E., Berginski, M.E., Urs, A.N. & Hoffman, B.D. Construction, imaging, and analysis of FRET-based tension sensors in living cells.

Methods Cell Biol **125**, 161-186 (2015).

108.   Guo, J., Sachs, F. & Meng, F. Fluorescence-based force/tension sensors: a novel tool to

visualize mechanical forces in structural proteins in live cells. *Antioxid Redox Signal* **20**,

986-999 (2014).

109.   Meng, F., Suchyna, T.M. & Sachs, F. A fluorescence energy transfer-based mechanical

stress sensor for specific proteins in situ. *FEBS J* **275**, 3072-3087 (2008).

110.   Meng, F., Suchyna, T.M., Lazakovitch, E., Gronostajski, R.M. & Sachs, F. Real Time

FRET Based Detection of Mechanical Stress in Cytoskeletal and Extracellular Matrix

Proteins. *Cell Mol Bioeng* **4**, 148-159 (2011).

111.   Meng, F. & Sachs, F. Visualizing dynamic cytoplasmic forces with a compliance-matched

FRET sensor. *J Cell Sci* **124**, 261-269 (2011).

112.   Borghi, N. *et al.* E-cadherin is under constitutive actomyosin-generated tension that is

increased at cell-cell contacts upon externally applied stretch (vol 109, 12568, 2012). *P

Natl Acad Sci USA* **109**, 19034-19034 (2012).

113.   Cai, D.F. *et al.* Mechanical Feedback through E-Cadherin Promotes Direction Sensing

during Collective Cell Migration. *Cell* **157**, 1146-1159 (2014).

114.   Paszek, M.J. *et al.* The cancer glycocalyx mechanically primes integrin-mediated growth

and survival. *Nature* **511**, 319-+ (2014).

115.   Lam, A.J. *et al.* Improving FRET dynamic range with bright green and red fluorescent

proteins. *Nat Methods* **9**, 1005-1012 (2012).

116.   Chen, H. *et al.* Dynamics of equilibrium folding and unfolding transitions of titin

immunoglobulin domain under constant forces. *J Am Chem Soc* **137**, 3540-3546 (2015).

117. Yao, M.X., Chen, H. & Yan, J. Thermodynamics of force-dependent folding and unfolding of small protein and nucleic acid structures. *Integr Biol-Uk* **7**, 1154-1160 (2015).

118. Jagannathan, B. & Marqusee, S. Protein folding and unfolding under force. *Biopolymers* **99**, 860-869 (2013).

119. Stabley, D.R., Jurchenko, C., Marshall, S.S. & Salaita, K.S. Visualizing mechanical tension across membrane receptors with a fluorescent sensor. *Nat Methods* **9**, 64-67 (2012).

120. Oesterhelt, F., Rief, M. & Gaub, H.E. Single molecule force spectroscopy by AFM indicates helical structure of poly(ethylene-glycol) in water. *N J Physics* **1**, 6 (1999).

121. Kienberger, F. *et al.* Static and Dynamical Properties of Single Poly(Ethylene Glycol) Molecules Investigated by Force Spectroscopy. *Single Molecules* **1**, 123-128 (2000).

122. Roberts, M.J., Bentley, M.D. & Harris, J.M. Chemistry for peptide and protein PEGylation. *Adv Drug Deliv Rev* **54**, 459-476 (2002).

123. Harder, P., Grunze, M., Dahint, R., Whitesides, G.M. & Laibinis, P.E. Molecular Conformation in Oligo(ethylene glycol)-Terminated Self-Assembled Monolayers on Gold and Silver Surfaces Determines Their Ability To Resist Protein Adsorption. *J Phys Chem B* **102**, 426-436 (1998).

124. Bouchiat, C. *et al.* Estimating the Persistence Length of a Worm-Like Chain Molecule from Force-Extension Measurements. *Biophys J* **76**, 409-413.

125. Jurchenko, C., Chang, Y., Narui, Y., Zhang, Y. & Salaita, K.S. Integrin-generated forces lead to streptavidin-biotin unbinding in cellular adhesions. *Biophys J* **106**, 1436-1446 (2014).

126. General, I.J., Dragomirova, R. & Meirovitch, H. Absolute free energy of binding of avidin/biotin, revisited. *J Phys Chem B* **116**, 6628-6636 (2012).

127. Moy, V.T., Florin, E.L. & Gaub, H.E. Intermolecular forces and energies between ligands and receptors. *Science* **266**, 257-259 (1994).

128. Tan, J.L. *et al.* Cells lying on a bed of microneedles: an approach to isolate mechanical force. *Proc Natl Acad Sci USA* **100**, 1484-1489 (2003).

129. Yun, C.S. *et al.* Nanometal surface energy transfer in optical rulers, breaking the FRET barrier. *J Am Chem Soc* **127**, 3115-3119 (2005).

130. Chhabra, R. *et al.* Distance-dependent interactions between gold nanoparticles and fluorescent molecules with DNA as tunable spacers. *Nanotechnology* **20**, 485201 (2009).

131. Liu, Y., Yehl, K., Narui, Y. & Salaita, K. Tension sensing nanoparticles for mechano-imaging at the living/nonliving interface. *J Am Chem Soc* **135**, 5320-5323 (2013).

132. Liu, Y. *et al.* Nanoparticle tension probes patterned at the nanoscale: impact of integrin clustering on force transmission. *Nano Lett* **14**, 5539-5546 (2014).

133. Morimatsu, M., Mekhdjian, A.H., Adhikari, A.S. & Dunn, A.R. Molecular tension sensors report forces generated by single integrin molecules in living cells. *Nano Lett* **13**, 3985-3989 (2013).

134. Shi, P., Shen, K., Ghassemi, S., Hone, J. & Kam, L.C. Dynamic Force Generation by Neural Stem Cells. *Cell Mol Bioeng* **2**, 464-474 (2009).

135. Mann, C. & Leckband, D. Measuring Traction Forces in Long-Term Cell Cultures. *Cell Mol Bioeng* **3**, 40-49 (2010).

136. Chang, Y. *et al.* A General Approach for Generating Fluorescent Probes to Visualize Piconewton Forces at the Cell Surface. *J Am Chem Soc* **138**, 2901-2904 (2016).

Chapter 2   Design and synthesis of DNA-based molecular tension probes to study integrin forces during early cell adhesion.

Adapted from Zhang, Y.; Ge, C.; Zhu, C.; Salaita, K.S. DNA-based digital tension probes reveal integrin forces during early cell adhesion. *Nature Communications* 2014, **5**, 5167, used with permission.

2.1   Introduction

The integrin family of transmembrane proteins constitute one of the major force transducing receptors in cells.[1] These receptors provide a mechanical bridge linking the ECM to the cytoskeleton. After binding their ligands, groups of integrin receptors often nucleate the formation of FAs, which are multi-micron scale structures comprised of hundreds of different adaptor and signaling proteins, such as talin, vinculin, and paxillin, that take part in mechanosensing.[2] Given that the majority of integrin functions, including ligand recognition, are force modulated, it is imperative to develop approaches to report the molecular forces experienced by integrin receptors within FA assemblies.[3] Accordingly, cellular traction forces are typically imaged at the scale of FAs by using techniques that track substrate deformation, such as TFM and mPADs.[4-7] These methods underpin our current understanding of FA mechanobiology, demonstrating the existence of force oscillations and revealing the mechanotransducing role of adaptor proteins, such as vinculin.[8] However, deformable substrates alter cell biology, are either computationally intensive to use or challenging to fabricate, and ultimately hinder high-resolution imaging.[9, 10] Moreover, the forces experienced by individual integrins are three-orders of magnitude smaller than the force sensitivity and spatial resolution of TFM and mPADs, thus hampering more detailed elucidation of the molecular mechanisms of mechanotransduction.[11, 12] Genetically-encoded protein tension sensors have also been developed to study the mechano-response of vinculin, E-cadherin, and PECAM-1.[13-16] While successful in these applications, protein engineering requires careful screening of insertion sites to ensure that localization and biological function are maintained since many proteins may not tolerate insertion of a ~500 amino acid sequence. In

addition, the optical response of genetically encoded probes is fixed to forces ranging from ~2 to

~6 pN which is limiting given that biological forces have been estimated to exceed ~50 pN in

certain processes.[17]
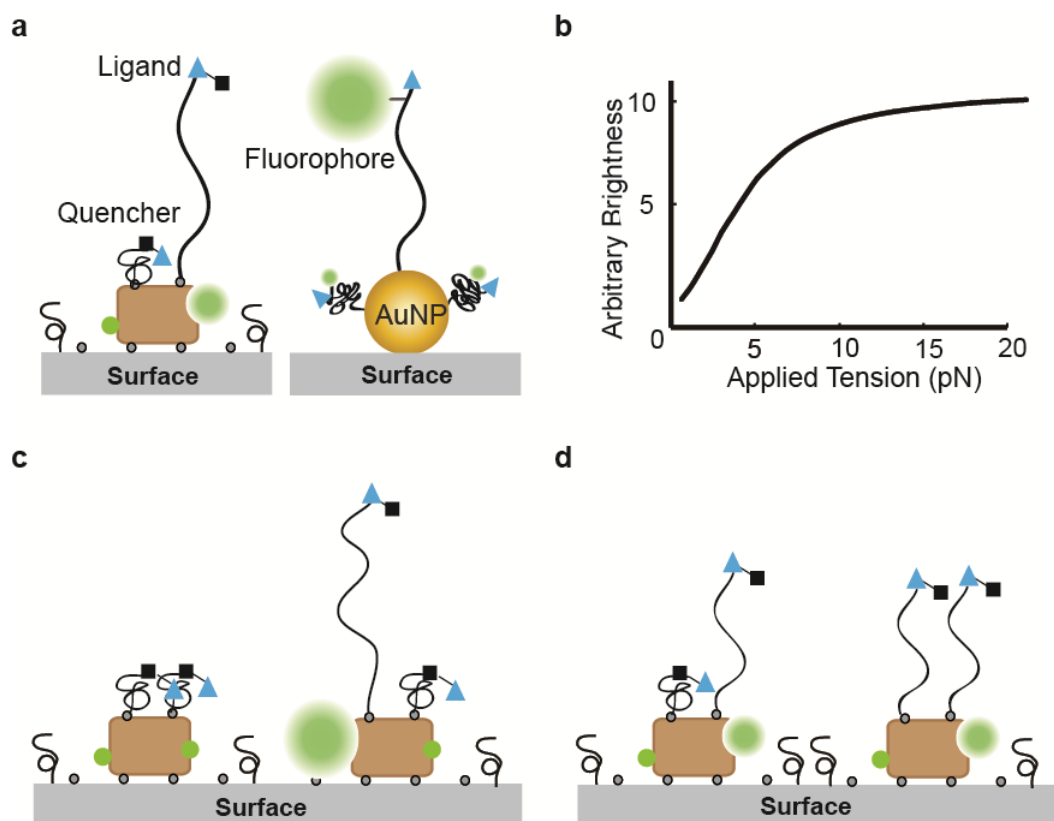
Figure 2.1 Issues associated with PEG-based MTFM probes. (a) Schematic of PEG based MTFM probes. (b) Analog response of PEG-based MTFM tension probes. (c) Schematic of the situation where only one of four sensors is stretched with a large force generating bright signal. (d) Schematic of the situation where three of four sensors are pulled by smaller forces. (c) and (d) is possible to generate similar fluorescent signals under microscope. Adapted with permission from reference 19 and 20.

Our lab invented molecular tension-based fluorescence microscopy (MTFM) to visualize

pN-forces exerted by cell surface receptors, including integrin receptors.[18-20] In MTFM, we

typically use a flexible polyethylene glycol (PEG) entropic spring that is flanked by a

fluorophore-quencher pair to report cellular forces that stretch the polymer (Figure 2.1a). Because

the PEG-based tension probes provide a graded "analog" response from an ensemble of molecules, it is difficult to obtain the absolute magnitude of tension per receptor and to decouple this from the density of mechanically strained receptors (Figure 2.1b, c and d). Dunn and colleagues tried to address this issue by using single molecule imaging of sparsely labeled integrin tension probes (~0.5 probes/μm^2).[21] Unfortunately, single molecule imaging requires the combination of oxygen-scavengers and triplet state quenchers which are deleterious to cells.[22, 23] Also, FAs contain thousands of integrin receptors that dynamically transmit mechanical signals, and thus the sparse density of reporters is limiting.

To this end, we report a new class of molecular tension probes that employs a DNA-hairpin as a "switch" element, thus unfolding at a threshold force and reporting tension in a digital rather than analog fashion (Figure 2.2a). DNA is ideally-suited for this purpose because an oligonucleotide's nucleobase sequence can be used to rationally tune its force-response function. Probes were designed to be highly adaptable, consisting of three oligonucleotides assembled through hybridization of 21-mer handles (Figure 2.2b): a stem-loop DNA hairpin that is unmodified (black), a peptide-displaying ligand strand conjugated to a fluorophore (green), and a surface-anchor strand that is tagged with a quencher (blue). The apposing termini of the ligand and anchor oligonucleotides were modified with a fluorophore-quencher pair, such that a sufficient force leads to hairpin unfolding accompanied by a drastic increase in fluorescence intensity.

Because each probe engages only a single receptor, the signal intensity from an ensemble of digital tension reporters is linearly proportional to the number of integrin molecules exceeding a

threshold force. This relationship overcomes the challenges of inferring single receptor forces from an ensemble fluorescence measurement; *i.e.* de-convoluting the relationship between probe density and the magnitude of tension per probe. Therefore, these reversible DNA-based probes obviate the need for estimating the average minimum force per receptor or conducting single molecule measurements.

ID	22% GC	77% GC	100% GC
Length (mer)	25	25	28
ΔG (kJ/mol)	21.9	49.6	95.2
Calc. $F_{1/2}$(pN)	4.2	9.6	16.0
Calib. $F_{1/2}$(pN)	4.7±1.7	------	13.1±2.1
$QE_{Cy3B-BHQ1}$ %	95.3±0.1	95.2±0.1	97.1±0.5
$QE_{Cy5-QSY21}$ %	94.1±0.2	95.3±0.3	94.8±0.3
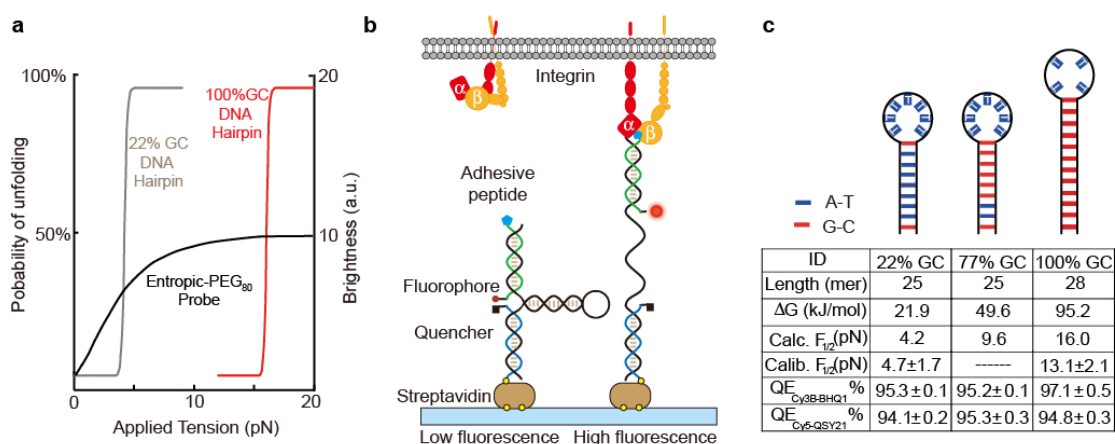
Figure 2.2 DNA-based digital tension probes. (a) Theoretical plot showing the expected increase in fluorescence signal as a function of applied force for the 100% and 22% GC-content hairpin probes and the PEG-based tension probe. DNA-hairpin tension probe response was obtained by fitting into a two-state Boltzmann distribution. The response of the PEG-based tension probe was based on experimental parameters obtained from reference 19. (b) Schematic of the integrin tension sensor, which is comprised of an anchor strand immobilized onto a surface (blue), a hairpin strand that unfolds under sufficient tension (black), and a ligand strand presenting an adhesive peptide (green). At the apposing termini of the ligand and anchoring strands, a fluorophore and quencher were coupled to report the force-induced unfolding of the hairpin. (c) Schematic showing the predicted secondary structure of the folded hairpin (top). Table summarizes the calculated and measured $F_{1/2}$ values, GC content, and the calculated free energy of hybridization of all hairpins used in this study. The quenching efficiency (QE) for Cy3B-BHQ1 and Cy5-QSY21 fluorophore-quencher reporters was measured on supported lipid membrane and is also included in the table. Error represents the standard deviation from three different pairs of samples.

2.2   Results

2.2.1 Design and synthesis of DNA-based tension probes
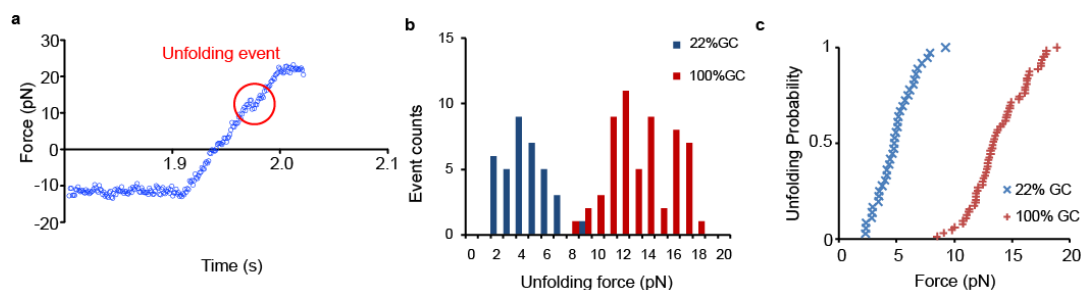
Figure 2.3 22% and 100% GC content hairpin probe calibration by BFP. (a) Example of an unfolding event measured by pulling of a 100% GC content hairpin probe. (b) Histogram of unfolding events for the two DNA-based probes that were tested n = 99 hairpins tested). Each event corresponds to the denaturation of a single DNA hairpin probe. (c) Cumulative histograms for the 22% and 100% GC content hairpin tension sensor unfolding probability.

We synthesized a small library of hairpin sensors with different GC contents, stem lengths and loop sizes to tune their stability and their $F_{1/2}$, the force at which 50% of hairpins unfold (Figure 2.2c, Figure A2.1-A2.3, Table 2.1, Table A2.1, Methods). The value of $F_{1/2}$ was initially estimated using the free energy of hairpin unfolding at zero force, as well as the free energy required to stretch ssDNA based on the WLC model (Methods, Table A2.2 and A2.3, Figure A2.4).[24, 25] The 22% and 100% GC content probes were further calibrated by using BFP, which is a single molecule force spectroscopy technique based on optically monitoring the displacement of the interface between a microparticle and a red blood cell.[26] Using a loading rate of 500 pN/s, we found that the experimental $F_{1/2}$ of the 22% and 100% GC probes was 4.7 ± 1.7 pN (*n* = 36 unfolding events), and 13.1 ± 2.4 pN (*n* = 63 unfolding events), respectively (Methods and Figure 2.3). Note that while the calculated and experimentally determined $F_{1/2}$ values generally agree, there is a greater difference for the larger sized hairpins. Also, broadening of the unfolding probability compared to the expected Boltzmann distribution is likely due to thermal noise and the heterogeneity in the orientations of the molecules probed.

To identify the most sensitive fluorescent reporters, a series of probes with different

fluorophore-quencher pairs were synthesized and characterized to determine the quenching

efficiency (QE) at 37 °C in PBS. We found that Cy3B-BHQ1, Atto647N-QSY21 and Cy5-QSY21

showed the greatest QEs (~95%) among the dye-quencher pairs tested, and fully recover their

fluorescence upon opening the hairpin with a complementary DNA strand (Figure 2.2c, Methods,

Figure A2.5, Table A2.4). Importantly, these QE values (95-97%) are greater than those reported

for any molecular tension probe, yielding a 20-30 fold increase in signal over background, which

represents a two- to three-fold improvement over PEG-based entropic spring reporters (Figure

2.2a).[18-20]

2.2.2 Visualizing integrin tension
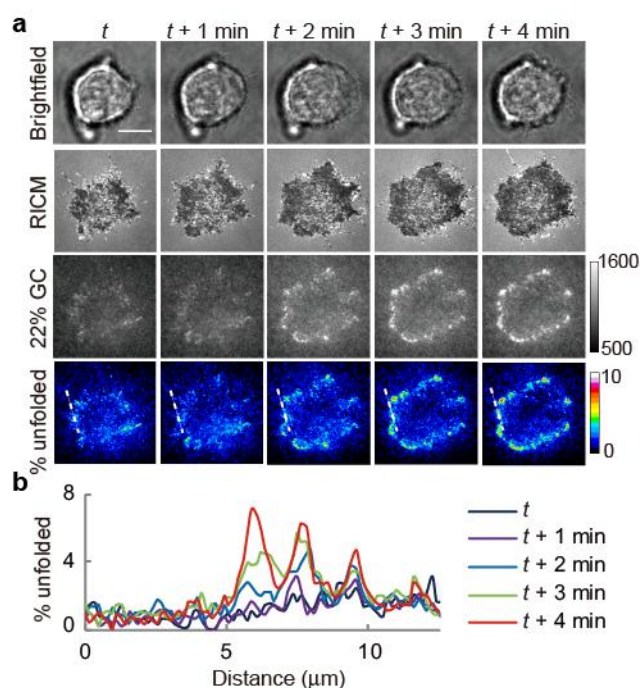
Figure 2.4 Visualizing integrin tension with DNA-based MTFM probes. (a) Representative brightfield, RICM, and MTFM (22% GC content hairpin probe) timelapse images at the indicated time points showing the initial stage of cell spreading and adhesion. The intensity of the 22% GC probe channel is in raw arbitrary units. The % unfolded channel indicates the fraction of the 22% GC hairpins that have been unfolded within each pixel. (b) Linescan analysis plot of the region highlighted with dashed white line in (a) shows the dynamic growth of tension within three

growing adhesions. Scale bar = 10 μm.

The DNA surface density on glass coverslips was empirically tuned (~400 molecules/mm^2, Methods and Figure A2.6) to support cell adhesion while limiting the background fluorescence. Breast cancer cells (HCC1143) were plated onto the 22% GC ($F_{1/2}$ = 4.7 pN) hairpin probe surface displaying cRGDfK and then timelapse videos were acquired as cells initiated spreading and adhesion (Figure 2.4). Initially, the tension signal was diffuse and included puncta of higher intensity. Within minutes, the tension signal localized to the cell edges and rapidly increased in intensity (up to 9% of probes were unfolded), which indicated that a larger density of hairpins were ruptured at those regions (force ≥ 4.7 pN). We determined the percentage of unfolded tension probes by calculating the fluorescence intensity of de-quenched dye corresponding to a fully opened hairpin probe, and assuming a linear relationship between the fraction of hairpins unfolded and the fluorescence intensity (Methods, Figure A2.7 and A2.8, Table A2.5-A2.9). Linescan analysis shows the progression of cellular forces across three nascent adhesions over a 5 min time period (Figure 2.4). This timelapse sequence shows that cell adhesion forces are highly dynamic, heterogeneous, and rapidly exceed the estimated 4.7 pN $F_{1/2}$ during initial cell spreading.
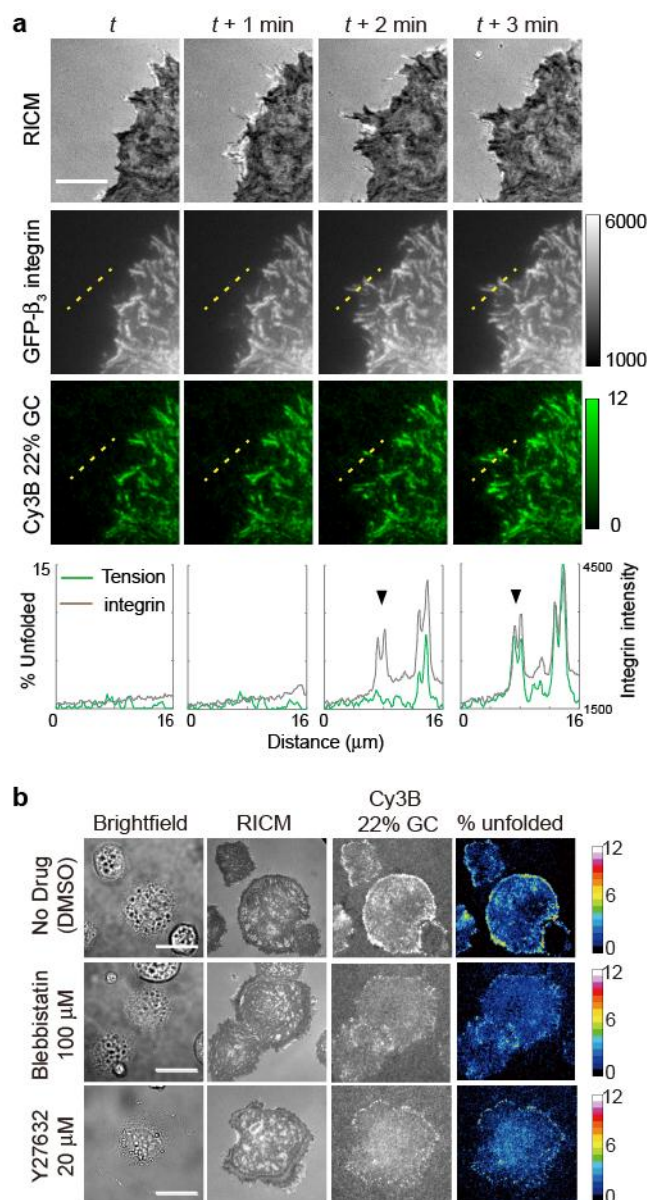
Figure 2.5 Control experiments show that tension sensor response is mechanically mediated by integrin receptors. (a) Colocalization of the integrin tension signal with GFP-β₃-integrin fluorescence. The images show RICM, GFP and Cy3B channels acquired over four timepoints. Linescan analysis of the three fluorescence channels is shown below each timepoint and show the arrival of the integrin receptors followed by the increase of integrin tension. This indicates that the majority of observed tension signal is transduced through the β₃-integrin receptor. Scale bar: 10 μm. (b) Blocking myosin II activity modulates integrin mechanical tension during initial cell spreading and adhesion. Representative images in brightfield, RICM, and Cy3B channels for control cells as well as cells treated with myosin II inhibitors blebbistatin and the ROCK inhibitor Y27632. Scale bar: 10 μm

To confirm that hairpin unfolding is mechanically mediated through integrin receptors, we

plated rat embryonic fibroblasts (REFs) expressing GFP-β_3-integrin on 22% GC probes surface

(Figure 2.5a). Timelapse total internal reflection fluorescence microscopy (TIRFM) showed

tension signal colocalization with GFP, confirming that forces were primarily exerted through the

β_3 integrin receptors[27, 28], and that tension increases following recruitment of β_3-integrin.

Treatment of cells with latrunculin B, an inhibitor of actin polymerization, led to complete and

rapid (1-3 min) decay of the tension signal, confirming that the signal is reversible and F-actin

dependent. In contrast, myosin II inhibition using blebbistatin or the ROCK inhibitor, Y27632,

did not abolish integrin tension, but led to a lower density of unfolded probes (Figure 2.5b).

Control experiments in which cells were seeded onto RGD-lacking DNA probes, either with or

without the hairpin structure, did not show any cell attachment or sensor activation (Figure A2.9a

and b). Importantly, cells plated on a binary mixture of DNA sensors, one that lacked the RGD

peptide, while the second lacking the dye-quencher pair, showed that the cells spread but failed to

generate a fluorescence response (Figure A2.9c). Together, these results unambiguously

demonstrate that hairpin probes report integrin-specific and cytoskeletal-mediated forces.

At later time points (~40 min) following cell seeding, we found that the fluorescence

intensity under cells decreased to levels below that of the quenched sensor background, for both

cyclic and linear RGD ligand (Figure A2.10). This loss in fluorescence was mainly due to

force-induced dissociation of the ligand strand (Figure A2.11), rather than nuclease activity, or

biotin-streptavidin dissociation, as observed with PEG-based MTFM probes.[20] Shearing of the

fluorescent ligand presenting strand is in agreement with recent results obtained using tension

gauge tethers.[17] Although ligand strand shearing at later time points simply reduces fluorescence

and does not lead to false positive signal, the current probe design is better suited for imaging early FA mechanics, and for imaging weaker receptor-mediated forces such EGF endocytosis and Notch activation.[17, 18, 29].

2.2.3 Selective mechanical response toward linear and cyclic RGD.

Given the molecular specificity of these probes, we next wondered whether integrin receptors would display mechanical selectivity when presented with a mixture of ligands. This is an important question because the ECM is comprised of nanoscale fibrillar protein assemblies that are chemically heterogeneous. For example, conventional techniques such as traction force microscopy report the average nN force from micron-sized elements, thus obscuring molecular specificity of tension in a complex mixture of ECM ligands.[4] We generated cRGDfK- and linear GRGDS-modified tension probes that were spectrally encoded by Cy3B-BHQ1 and Cy5-QSY21 reporters, respectively (Figure 2.6a). Both ligand strands were hybridized to the 77% GC content sensors and anchored to a substrate in 1:1 molar ratio. Cells plated onto this multiplexed surface generated signals that were highly localized at the lamella in the two fluorescence channels (Figure 2.6b). However, the intensity of the linear peptide channel was significantly weaker, and showed at least a 2-fold smaller number of unfolded hairpins when compared to cRGDfK ligands and also when compared to the signal generated by surfaces exclusively presenting the linear GRGDS 77% GC content sensor (Figure A2.12). To exclude the possibility that this difference was due to fluorophore photophysics and other artifacts (Figure A2.13-A2.15), we swapped the dye-quenchers pair encoding and observed the same trend (Figure 2.6c). These results show that integrin-ligand mechanical selectivity acts at the individual ligand level, whereby RGD ligand

variants experience differential magnitudes of tension regardless of their spatial proximity. The

mechanism for this selectively is likely due to lower integrin affinity for linear RGD ligands

when compared to cyclic RGD peptides.[23] These results demonstrate how integrin receptors

would mechanically respond when presented with chemically heterogeneous ECM ligands in

more physiologically relevant settings.
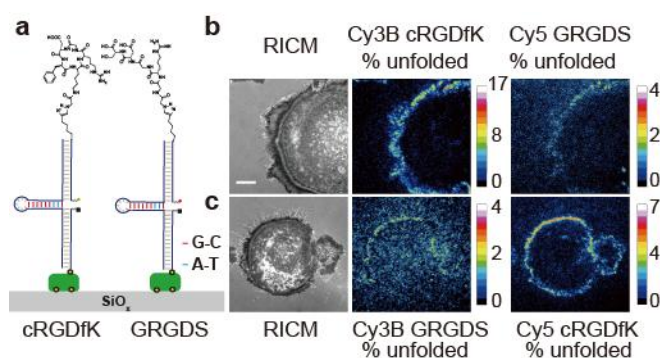
Figure 2.6 Integrin mechanical response specificity using spectrally-encoded hairpin probes presenting different ligand types. (a) Schematic of multiplexed tension probes modified with cyclic RGDfK and linear GRGDS peptides that were coupled to sensors employing identical hairpins (77% GC content), and encoded using different fluorophore-quencher reporters. (b) Representative RICM and % unfolded maps for cells cultured on substrates shown in (a). The fluorophore-quencher encoding was reversed in (c) to exclude potential imaging artifacts. (b) and (c) show that at least a 2-fold greater population of cyclic RGDfK peptide sensors were unfolded compared to the linear GRGDS peptides. Scale bar = 10 μm.

2.2.4 $F_{1/2}$-encoded probes to analyze force distribution within FAs

To analyze the spatial distribution of forces within individual growing adhesions, we spectrally

encoded a binary mixture of cRGDfK tension probes with the 100% and 22% GC hairpins using

the Atto647N and Cy3B dyes (Figure 2.7a). As expected, cells attached and spread onto this 1:1

ratio multiplexed sensor surface, generating similar signals in both fluorescence channels (Figure

2.7a). Timelapse imaging showed that both probes displayed similar dynamics, spatial

localization, and intensities (unfolding percentage per unit area) during cell spreading and FA

formation (Figure 2.7a-c). This trend was maintained when the encoding was swapped or when both channels were encoded using the same 100% GC content probe. This general agreement between the two channels indicates that most engaged integrin receptors exerted tension that was greater than or equal to 13.1 pN.

Upon closer inspection of the data, we noted two additional features. The first was that a subset of FAs appeared larger and more intense in the 22% GC probe channel than the 100% GC probe channel (Figure 2.7b). To quantify this observation, we measured the ratio of the signal intensity when the 100% and 22% GC content probes were encoded with Atto647N and Cy3B, respectively, and compared this to experiments with reversed encoding as well as control experiments where both probes used the 100% GC hairpin (Figure 2.7d, $n = 15$ cells; Figure A2.16). This confirms that a subset of integrins exert tension that is lower than 13.1 pN but greater than 4.7 pN. The existence of such a subpopulation is expected, as the tension must gradually rise per integrin during FA maturation.

The second observation was that a subset of FAs near the cell edge preferentially triggered the 100% GC probe over the 22% GC probe specifically at the tips of these adhesions (Figure 2.7c and 2.7e). To verify the statistical significance of this observation, we measured the offset between the start positions of tension signal in the two fluorescence channels when each channel encoded different hairpins and when each channel encoded the same 100% GC hairpin (as a control). Histogram analysis of 221 adhesions from 17 cells indicated that there is a subset of FAs where the 100% GC hairpin probe was triggered ~0.5 microns ahead of the 22% GC probe (Figure 2.7e, and Figure A2.17 and A2.18). This small population of FAs with an offset is not

observed in the control experiment and is counterintuitive, as both probes are chemically identical and the 22% GC probes mechanically denature at significantly lower forces than the 100% GC probes. Thus, one would expect to observe the opposite phenomenon, *i.e.* the 22% GC probe should be triggered closer to the cell edge because the integrin-ligand association rates are identical for both probes and initial adhesions likely exert lower magnitude forces that may not be sufficient to trigger the 100% GC content probes. Therefore, the offset in the start position of tension indicates that there is a small differential preference for integrins to remain bound to the more rigid 100% GC probes that can support higher forces before yielding, thus suggesting a molecular basis for cellular rigidity sensing of the substrate. Although further work is needed to fully elucidate the molecular underpinnings of the observed preference, the results obtained from multiplexed sensors highlight the unique capabilities of DNA-tension probes, providing a new approach to investigate differential integrin forces in a manner dependent on chemo-mechanical properties of individual ligand molecules.
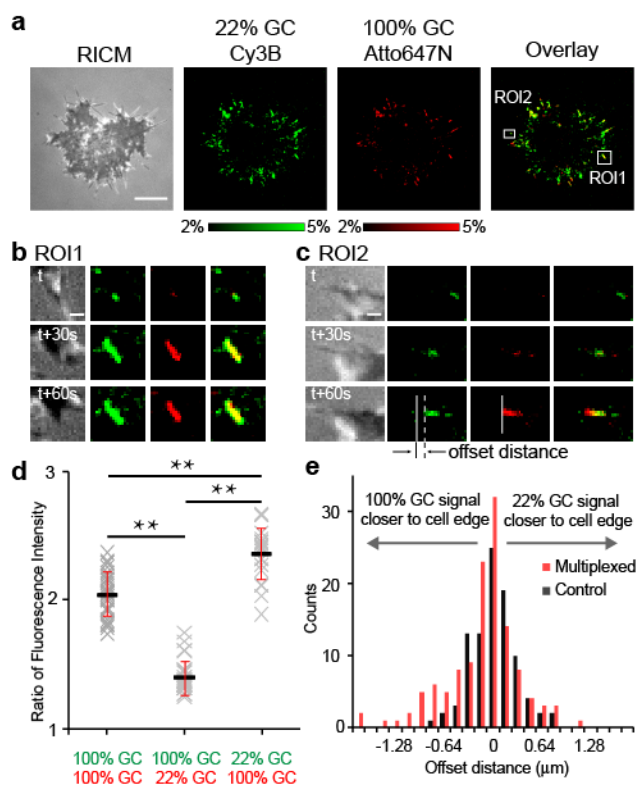
Figure 2.7 Investigating the force distribution within integrin clusters using spectrally-encoded tension probes with different $F_{1/2}$. (a) Representative RICM and % unfolded maps of the 22% GC hairpin probe (Cy3B-BHQ1, green), 100% GC hairpin probe (Atto647N-QSY21, red), and the overlay channel of a single cell during initial spreading. Scale bar = 10 μm. (b) Zoom-in of region of interest 1 (ROI1) showing the dynamics of a growing adhesion where the 22% GC probe signal was greater than that of the 100% GC probe. Scale bar = 2 μm. (c) Zoom-in of ROI2 showing the dynamics of a growing adhesion where the start point of the adhesion appeared closer to the cell edge in the 100% GC probe channel compared to the 22% GC probe channel (offset). Scale bar = 2 μm. (d) Plot showing the ratio of the intensities of the Cy3B and Atto647 fluorescence channels when the encoding was as follows: Cy3B-100% GC and Atto647N-100% GC; Cy3B-100% GC and Atto647N-22% GC; Cy3B-22% GC and Atto647N-100% GC. The data was collected from $n = 15$ cells, error bars represent the standard error of the mean (SEM). ** indicates a P-value < 0.01 in *t*-test. (e) Histogram analysis of the offset between the 100% GC and 22% GC hairpin probe signal at the cell edge (221 adhesions from $n = 17$ cells). Data analysis is described in Figure A2.17 and A2.18. The black bars represent the control where both channels were encoded using the 100% GC hairpin, while the red bars represent experiments where each channel encoded either the 100% or 22% GC probes. The control histogram was best fit using a single Gaussian peak, while the multiplexed histogram was best fit to two Gaussian peaks.

2.3   *Discussion*

DNA-based tension probes confer several advantages. First, the predictable secondary

structure places the fluorophore-quencher pair in a well-defined position, thus lowering background signal and increasing the signal-to-noise ratio (~20-30 fold over background). This design strategy is widely used by molecular beacon based assays.[30] Accordingly, the $F_{1/2}$ is highly tailorable, and the hairpin can be precisely tuned to generate a clear binary response at a desired threshold tension (~1-20 pN).[24] Second, by employing a three-strand system, we circumvent chemical modification of the hairpin oligonucleotide, and therefore, existing models can be used to estimate the $F_{1/2}$. The three-strand design is also advantageous because it allows one to tune libraries of $F_{1/2}$ values while avoiding re-synthesis of the anchor and ligand strands. In principle, the anchoring strand (and DNA-probes) can be attached to virtually any type of material, including three-dimensional matrices that better mimic the ECM, which is of great interest to the community. The caveat of the three-strand design pertains to force-induced shearing of the probe from the surface, which is a unique problem associated with the large mechanical loads in integrin-based mechanotransduction processes. Third, although an ensemble of DNA tension probes are engaged and activated within each diffraction limited region, which is necessary to support cell adhesion, we extract molecular details because each sensor functions as a digital switch for well-defined thresholds of force. Finally, the growing availability of inexpensive and rapid oligonucleotide synthesis allows one to easily generate and systematically test libraries of tension probes with tunable force sensitivity, thus ensuring the broad dissemination of this method.

2.4   Materials and methods

2.4.1 Materials

The fluorescent dye Cy5 NHS ester (Cat. # 23020) was purchased from Lumiprobe corporation (Hallandale Beach, FL). The fluorescent dye Cy3B NHS ester (Product code: PA63101) was purchased from GE Healthcare Life Science (Pittsburgh, PA). Quencher QSY21 succinimidyl ester (Cat. # Q-20132) was purchased from Life Technologies (Carlsbad, CA). The fluorescent dye Atto 647N NHS ester was purchased from Sigma-Aldrich (St. Louis, MO). Cyclo [Arg-Gly-Asp-d-Phe-Lys(PEG-PEG)] (Product code: PCI-3696-PI, c(RGDfK(PEG-PEG)), PEG = 8-amino-3,6-dioxaoctanoic acid) was acquired from Peptides International (Louisville, KY). Gly-Arg-Gly-Asp-Ser (Cat. # G4391) was purchased from Sigma-Aldrich (St. Louis, MO). Glass coverslips (number 2, 25 mm diameter) were acquired from VWR. The heterobifunctional linkers NHS-azide (#88902) and NHS-biotin (#20217) were purchased from Thermo Fisher Scientific (Rockford, IL). Ascorbic acid (>99.0%) and 96-well plates were purchased from Fisher Chemical & Scientific (Pittsburg, PA). DMF (>99.5%), DMSO (99.5%) and sodium bicarbonate (99.0%) were acquired from EMD chemicals (Philadelphia, PA). Sulfuric acid was acquired from Avantor Performance Materials (Center Valley, PA). Ethyl alcohol (EtOH) (200 proof) was purchased from Decon Labs (King of Prussia, PA). 3-aminopropyltriethoxysilane (APTES) and $CH_3(CH_2CH_2O)_{9-12}(CH_2)_3Si(OCH_3)_3$ (mPEG) were acquired from Gelest (Morrisville, PA). Unless otherwise stated, all the other starting materials and reagents were purchased from Sigma-Aldrich and used without further purification. All buffers were made with Nanopure water (18.2 MΩ) and passed through a 0.2 μm filtration system.

2.4.2 DNA-based tension probes

All oligonucleotides were custom synthesized and purified by Integrated DNA Technologies

(Coralville, IA), unless otherwise noted. All the sequences are listed in **Table 2.1**. This design

consisted of a single strand DNA hairpin hybridized through two 21-mer DNA handles to the

ligand and anchor strands . Poly(T) was used for the hairpin loop sequence to avoid secondary

structures and base stacking. The 3' terminus of the anchor strand was modified with a biotin

group to immobilize the oligonucleotide to a streptavidin surface. The alkyne group at the 5'

terminus of the ligand strand was used in a 1',3' dipolar cycloaddition click reaction to couple the

appropriate RGD peptides. To generate multiplexed tension probe surfaces, each hairpin sensor

was folded separately and then mixed at 1:1 ratio and added to the streptavidin surface.

Table 2.1 Oligonucleotide sequences

ID	DNA Sequence
Anchor strand	5'-/5AmMC6/-CGC ATC TGT GCG GTA TTT CAC TTT – /3BioTEG/-3'
Anchor strand with BHQ-1*	5'-/BHQ 1/-CGC ATC TGT GCG GTA TTT CAC TTT-/ Biotin/-3'
Ligand strand	5'-/5Hexynyl/-TTT GCT GGG CTA CGT GGC GCT CTT– /3AmMO/-3'
22% GC	5'-GTG AAA TAC CGC ACA GAT GCG TTT- <u>GTA TAA ATG TTT TTT TCA TTT ATA C</u> -TTT AAG AGC GCC ACG TAG CCC AGC -3'
77% GC	5'-GTG AAA TAC CGC ACA GAT GCG TTT- <u>GTA CGC GCG TTT TTT TCG CGC GTA C</u>-TTT AAG AGC GCC ACG TAG CCC AGC -3'
Complementary sequence to 77% GC hairpin	5'- AAA GTA CGC GCG AAA AAA ACG CGC GTA CAAA -3'
100% GC	5'-GTG AAA TAC CGC ACA GAT GCG TTT- <u>GCG CGC GCG CGC TTT TGC GCG CGC GCG C</u>-TTT AAG AGC GCC ACG TAG CCC AGC -3'
Complementary sequence to 100% GC hairpin	5'-AAA GCG CGC GCG CGC AAA AGC GCG CGC GCG CAA A-3'
H45	5'-GTG AAA TAC CGC ACA GAT GCG TTT- <u>CGA TAA CTT</u>

	TTT TTT TTT TTT TTT TTT TTT TTG TTA TCG –TTT AAG AGC GCC ACG TAG CCC AGC -3'
Complementary sequence to H45	5'- AAA CGA TAA CAA AAA AAA AAA AAA AAA AAA AAA AAG TTA TCG AAA-3'

*Anchor strand with BHQ-1 was purchased from Biosearch Technology (Novato, CA). Underlined sequences represent regions that are expected to fold into hairpin structures.

2.4.3 $F_{1/2}$ calculation for DNA hairpin

The following $F_{1/2}$ calculation was primarily based on the assumptions and measurements used by Woodside et al [24]. The total free energy of the hairpin can be described as follows:

$$\Delta G(F,x) = \Delta G_{fold} + \Delta G_{stretch} + F \cdot x \tag{1}$$

where ΔG_{fold} is the free energy of unfolding the hairpin at F= 0, F is the externally exerted force, x is the hairpin extension, and $\Delta G_{stretch}$ is the free energy of stretching the ssDNA from F=0 to F= $F_{1/2}$, and can be calculated from worm-like chain model (WLC) as follows[24]:

$$\Delta G_{stretch} = \frac{k_B T}{L_p} \frac{L_0}{4(1-x/L_0)} [3(x/L_0)^2 - 2(x/L_0)^3] \tag{2}$$

where L_p is the persistence length of ssDNA (~1.3 nm), L_0 is the contour length of ssDNA (~0.63 nm per nucleotide), x is the hairpin extension from equilibrium and was calculated by using $(0.44 \times (n-1))$ nm, and k_B is the Boltzmann constant, and T is temperature.

To use these equations and estimate the $F_{1/2}$ for each hairpin probe, we determined the sum of ΔG_{fold} and $\Delta G_{stretch}$, and estimated the hairpin displacement needed for unfolding, Δx, by using $((0.44 \times (n-1))-2)$ nm, where n represents the number of bases comprising the hairpin. Note that we subtract a distance of 2 nm because this corresponds to the initial separation between the hairpin termini, which is set by the diameter of the hairpin stem duplex (effective helix width)[24]. When F=$F_{1/2}$, then the free energy of the transition equals zero and the $F_{1/2}$ can be rearranged as follows:

$$F_{1/2} = \frac{\Delta G_{fold} + \Delta G_{stretch}}{\Delta x} \qquad (3])$$

In our calculations, $\Delta G_{stretch}$ was determined using Equation S2 without modification. ΔG_{fold} was determined using nearest neighbor free energy parameters obtained from the IDT oligoanalyzer 3.1, which uses the UNAfold software package, and will now be referred to as ΔG_{IDT}. Equation (3) was used to infer the $F_{1/2}$ for tension probes at experimental conditions (37 °C, 140.5 mM Na$^+$ and 0.4 mM Mg^{2+}), and this data is summarized in Table A2.2.

2.4.4 Force probes calibration by biomembrane force probe (BFP)

The BFP measurement was based on previous work, which has been described in detail elsewhere[26]. In the BFP setup, a biotinylated red blood cell (RBC) was first aspirated by a micropipette. A streptavidinylated glass bead was then attached to the apex of the RBC to form an ultra-sensitive force probe.   On the opposite side, a bead coated with our DNA force probe was aspirated by a target micropipette. A piezoelectric translator (Physical Instrument, MA) drove the target pipette with sub-nanometer precision via a capacitive sensor feedback control. The beads were assembled in a cell chamber filled with L15 media supplemented with 5 mM HEPES and 1% BSA and observed under an inverted microscope (Nikon TiE, Nikon) through two cameras. One camera (GC1290, Procilica, MA) captured real-time images at 30 frames per second (fps), while the other (GE680, Proscilica, MA) recorded at 1,600 fps as the region of interest was confined to the contact interface between the RBC and the bead. A customized LabView (National Instrument, TX) program analyzed the image and tracked in real-time the position of the bead with a 3-nm displacement precision [31]. The BFP spring constant was set to ~0.3 pN/nm, and it was determined from the suction pressure inside the probe pipette that held the RBC, the radius of the probe

pipette, the diameter of the spherical portion of the RBC outside of the pipette, and the contact area between the RBC and the probe bead[31, 32].

Briefly, in a measurement cycle, a DNA-coated 5-micron silica bead was brought into contact with the probe bead with a 20 pN impingement force for 0.1 s to allow bond formation. The target pipette was then retracted at 500 pN/s until it reached a 20 pN force level before dropping the force level to ~0 pN by bringing the two beads into close proximity again. The biotin-streptavidin bond was ruptured after 1 s, and the target bead was returned to the original position to start the next cycle. To ensure that most adhesion events were due to single bonds, adhesion frequency (number of adhesions divided by total number of contacts) was controlled to be ≤20% by adjusting the coating density of the DNA force probe[33].

An unfolding event was identified by a dip in force level in the force-ascending phase (Figure 2.3), due to the lengthening of the DNA upon hairpin opening. Similarly, a folding event was identified by a rise in force level in the force-descending phase. The force at which each unfolding event occurred was recorded and the cumulative histogram was plotted in Figure 2.3 to determine the $F_{1/2}$.

2.4.5 Quenching efficiency (QE) measurement for different reporter pairs

To identify the optimal fluorophore-quencher pairs for the DNA-based MTFM probes, we synthesized a series of probes with different reporters and measured their QE (Table A2.3). MTFM probes were anchored to supported lipid membrane, to minimize non-specific binding and ensure a homogeneous and reproducible DNA density across all the tested pairs. Fluorophore labeling was performed as described in Figrue A2.1.

For all these measurements, a 45-mer hairpin (H45, ~15.38 nm, Table 2.1) was used to ensure that the donor was completely dequenched upon hybridization. The fluorescence intensity of the hairpin sensor, I_{DA}, was measured with the closed H45 in triplicate (Figure A2.5). To measure the donor only intensity, I_D, H45 was hybridized to a complementary strand (10-fold molar excess), and then assembled with the DNA handles and anchored to the surface. Based on these measurements, we selected the Cy5-QSY21, Atto647N-QSY21 and Cy3B-BHQ1 pairs given their superior QE when compared to other fluorophore quencher combinations.

2.4.6 Calibration curve and determination of F factor and sensor density

This protocol has been adapted from Galush *et al.*[34], and is briefly described in this section. To calibrate the fluorescence intensity, DOPC supported lipid membranes were doped with TRITC-DHPE lipids with concentrations ranging from 0 to 0.08 mol% and imaged under the same conditions used in live cell imaging (Table A2.6). The number of fluorophore molecules per unit area was estimated from the footprint of DOPC, which was reported at 0.72 nm^2. In order to use the calibration curve, the intensity of the ligand molecules was compared with the lipid-fluorophore standards to obtain the F factor. The F factor is defined as: $F = \frac{I_{bulk(sensor)}}{I_{bulk(TRITC-DHPE)}}$, where $I_{bulk(sensor)}$ and $I_{bulk(TRITC-DHPE)}$ are the intensity of the ligand or lipid molecules in solution after being normalized for concentration. This value was measured on the fluorescence microscope by moving the focal plane (~200 μm) into the center of the sample.

2.4.7 Measurement of QE (1- IDA/ID) on glass substrate

To determine the QE as a function of the hairpin used in DNA-based tension probes, we recorded the fluorescence intensity of the closed hairpin, I_{DA}, on glass substrates at experimental

conditions (37 °C, cell media) (Figure A2.7 a and c). To measure the donor only intensity, I_D, tension probes were hybridized to their complementary strands (10-fold molar excess), and DNA handles (Figure A2.7 b and d). Note that these QE value were in general agreement values obtained on supported lipid membranes in 1X PBS at r.t.

2.4.8 Conversion of IDA/ID to calculate the fraction of unfolded hairpins

To calculate the fraction of hairpins that are unfolded from any given cell experiment, we assumed that the fluorescence intensity of immobilized tension probes at resting (F=0 pN) corresponded to a monolayer of fully folded hairpins (0% unfolded, I_{DA}). Since hairpins that were hybridized with a 10-fold excess of complementary stands are completely dequenched (Figure A2.7), the fluorescence intensity from this surface corresponds to hairpins that are 100% unfolded. Therefore, the fluorescence intensity of the 100% unfolded hairpins corresponds to I_D. Given that there is a linear relationship between the fraction of unfolded hairpins and the quenching efficiency, we used the ratio of I_{DA}/I_D to obtain this linear function (Figure A2.7e). This linear relationsip was then used to convert the fluorescence intensity from the cell experiment to the fraction of unfolded hairpins (% unfolded).

2.4.9 Imaging parameters

Table A2.5- A2.9 summarize all the imaging parameters used in our experiments. Sensors with GC-content of 22% GC and 77% GC have the same length (25mer); therefore these two sensors share the same values for QE, I_{DA}/I_D and conversion function determined from the 77% GC probe surface. We assumed that the QE for each probe remained the same regardless of whether it was displayed in single channel experiment or if it was included as part of a

multiplexed surface with hairpins of different $F_{1/2}$.

2.4.10 Surface preparation

The glass substrates were covalently functionalized with biotin and modified with streptavidin by using previously published literature procedures[18]. Briefly, glass coverslips (number 2, 25-mm diameter; VWR) were sonicated in Nanopure water for 10 min and then etched in piranha (a 3:1 mixture of sulfuric acid (Avantor Performance Materials) and hydrogen peroxide (Sigma)) for 10 min (please take caution: piranha is extremely corrosive and may explode if exposed to organics). The glass coverslips were then washed six times in a beaker of Nanopure water (18.2 mΩ) and placed into three successive wash beakers containing EtOH (Decon Labs) and left in a final fourth beaker containing 1% (3-aminopropyl)triethoxysilane (APTES, Sigma) in EtOH for 1 h. The substrates were then immersed in the EtOH three times and subsequently rinsed with EtOH and dried under nitrogen. Substrates were then baked in an oven (~100 °C) for 10 min. After cooling, the samples were incubated with NHS-biotin (Thermo Fisher) at 2 mg/ml in DMSO (Sigma) overnight. Subsequently, the substrates were washed with EtOH and dried under nitrogen. The substrates were then washed with 1× PBS (3 × 5 ml) and incubated with BSA (EMD Chemicals, 100 μg/μl, 30 min) and washed again with 1× PBS (3 × 5 ml). Streptavidin was then added (1 μg/ml 45 min, room temperature) followed by washing with 1× PBS (3 × 5 ml). The chambers were then incubated with the DNA-based tension sensor (10 nM) for 1 h and rinsed prior to conducting cell experiments and imaging.

2.4.11 Supported lipid membrane preparation

The supported lipid bilayers was prepared by mixing 99.9%

1,2-dioleoyl-*sn*-glycero-3-phosphocholine (DOPC) and 0.1%

1,2-dioleoyl-*sn*-glycero-3-phosphoethanolamine-N-(cap biotinyl) (sodium salt) (DPPE-biotin).

The solution was dried with a rotary evaporator and placed under a stream of N_2 to ensure

complete evaporation of the solvent. These lipid samples were then resuspended in Nanopure

water and subjected to 3 freeze/thaw cycles by alternating immersions in an acetone and dry ice

bath and a warm water bath (40 °C). To obtain small unilamellar vesicles (SUV's), lipids were

extruded through a high-pressure extruder with a 200 nm nanopore membrane (Whatman).

Supported lipid bilayers were assembled by adding SUV's to 1M NaOH etched 96 well plates

with glass-bottomed wells. After blocking with 0.1% BSA for 30 min, bilayer surfaces were

incubated with streptavidin (1 μg/400 μL) for 1h. Wells were rinsed 3 times with 5 mL of 1x PBS,

then incubated with the appropriate DNA hairpin sensors duplex (50 nM) for 1 h and rinsed 3x

with 5 mL of 1x PBS before imaging.

2.4.12 HPLC

All DNA conjugates were purified by using a C18 column (diameter: 4.6 mm; length: 250

mm) in a reverse phase binary pump HPLC that was coupled to a diode array detector (Agilent

1100). The flow rate was generally set to 1 ml/min with a linear gradient of 10 – 60% B over 50

min (A: aqueous 0.1 M triethylammonium acetate buffer; B:acetonitrile (LC-MS Chromasolv,

≥99.9%; Fluka). Unless otherwise noted, this elution gradient was followed by a second gradient

of 60 – 100 % B over 10 min to collect the more hydrophobic fractions.

2.4.13 MALDI-TOF mass spectroscopy

The matrix was prepared by dissolving 20 mg 3-hydroxypicolinic acid (3-HPA) into 1 mL of

matrix solvent (50% acetonitrile, 0.1% TFA, and 10% of a solution of 50 mg/mL ammonium citrate). 2 μL of this mixture was added to each well on the MALDI plate. After allowing the solution to dry for 20 min, the sample was analyzed by a high performance MALDI time-of-flight mass spectrometer (Voyager STR).

2.4.14 Fluorescence microscopy

Live cells were imaged in standard cell media at 37 °C, and fixed cells were imaged in 1% BSA in 1× PBS at room temperature. During imaging, physiological temperature was maintained with a warming apparatus consisting of a sample warmer and an objective warmer (Warner Instruments 641674D and 640375). The microscope was a Nikon Eclipse Ti driven by the Elements software package. The microscope features an Evolve electron multiplying charge coupled device (EMCCD; Photometrics), an Intensilight epifluorescence source (Nikon), a CFI Apo 100× (numerical aperture (NA) 1.49) objective (Nikon) and a TIRF launcher with two laser lines: 488 nm (10 mW) and 638 nm (20 mW). This microscope also includes the Nikon Perfect Focus System, an interferometry-based focus lock that allowed the capture of multipoint and time-lapse images without loss of focus. The microscope was equipped with the following Chroma filter cubes: TIRF 488, TRITC, Epi 640 and reflection interference contrast microscopy (RICM).

2.4.15 Hairpin hybridization

All DNA oligonucleotides were allowed to fold into their hairpin secondary structure in 50 μl PBS at a concentration of 100 nM in a 0.2 ml *Thermowell Tube*. All oligonucleotides were first

denatured at 75 °C for 5 min. This was followed by a renaturation step in which the temperature was allowed to return to room temperature at a rate of 1.3 °C/min.

2.4.16 Cell culture

HCC1143 human breast carcinoma cells were cultured in RPMI 1640 medium (Mediatech) supplemented with 10% FBS (Mediatech), HEPES (9.9 mM, Sigma), sodium pyruvate (1 mM, Sigma), L-glutamine (2.5 mM, Mediatech), penicillin G (100 IU/ml, Mediatech) and streptomycin (100 μg/mL, Mediatech) and were incubated at 37 °C with 5% CO_2. Cells were passaged at 90% confluency and plated at a density of 50% and media renewed every 3 days. NIH 3T3 mouse embryonic fibroblasts and Rat embryonic fibroblasts (REF) expressing GFP-β_3-integrin cells were cultured in DMEM (Mediatech) supplemented with 10% Calf Serum (Mediatech), L-glutamine (2.5 mM, Mediatech), penicillin G (100 IU/ml, Mediatech) and streptomycin (100 μg/mL, Mediatech) at 37 °C with 5% CO_2. Cells were passaged at 80% confluency and plated at a density of 4×10^3 cells/cm^2 (100×10^3 cells/flask) and media renewed every 3 days.

2.5   References

1.   Burridge, K., Fath, K., Kelly, T., Nuckolls, G. & Turner, C. Focal adhesions - Transmembrane junctions between the extracellular-matrix and the cytoskeleton. *Annu Rev Cell Biol* **4**, 487-525 (1988).

2.   Kanchanawong, P. *et al.* Nanoscale architecture of integrin-based cell adhesions. *Nature* **468**, 580-584 (2010).

3.   Schoen, I., Pruitt, B.L. & Vogel, V. The Yin-Yang of Rigidity Sensing: How Forces and Mechanical Properties Regulate the Cellular Response to Materials. *Annu Rev Mater Res* **43**, 589-618 (2013).

4.   Plotnikov, Sergey V., Pasapera, Ana M., Sabass, B. & Waterman, Clare M. Force Fluctuations within Focal Adhesions Mediate ECM-Rigidity Sensing to Guide Directed Cell Migration. *Cell* **151**, 1513-1527 (2012).

5.   Sabass, B., Gardel, M.L., Waterman, C.M. & Schwarz, U.S. High resolution traction force microscopy based on experimental and computational advances. *Biophys J* **94**, 207-220 (2008).

6.   Tan, J.L. *et al.* Cells lying on a bed of microneedles: an approach to isolate mechanical force. *Proc Natl Acad Sci U S A* **100**, 1484-1489 (2003).

7.   Lemmon, C.A. *et al.* Shear force at the cell-matrix interface: enhanced analysis for microfabricated post array detectors. *Mech Chem Biosyst* **2**, 1-16 (2005).

8.   Dumbauld, D.W. *et al.* How vinculin regulates force transmission. *P Natl Acad Sci USA* **110**, 9788-9793 (2013).

9.   Discher, D.E., Janmey, P. & Wang, Y.L. Tissue cells feel and respond to the stiffness of their substrate. *Science* **310**, 1139-1143 (2005).

10.   Ghassemi, S. *et al.* Cells test substrate rigidity by local contractions on submicrometer pillars. *P Natl Acad Sci USA* **109**, 5328-5333 (2012).

11.   Schwarz, U.S. *et al.* Calculation of forces at focal adhesions from elastic substrate data: The effect of localized force and the need for regularization. *Biophys J* **83**, 1380-1394

(2002).

12. Wiseman, P.W. *et al.* Spatial mapping of integrin interactions and dynamics during cell migration by Image Correlation Microscopy. *J Cell Sci* **117**, 5521-5534 (2004).

13. Grashoff, C. *et al.* Measuring mechanical tension across vinculin reveals regulation of focal adhesion dynamics. *Nature* **466**, 263-266 (2010).

14. Cai, D.F. *et al.* Mechanical Feedback through E-Cadherin Promotes Direction Sensing during Collective Cell Migration. *Cell* **157**, 1146-1159 (2014).

15. Conway, D.E. *et al.* Fluid Shear Stress on Endothelial Cells Modulates Mechanical Tension across VE-Cadherin and PECAM-1. *Curr Biol* **23**, 1024-1030 (2013).

16. Borghi, N. *et al.* E-cadherin is under constitutive actomyosin-generated tension that is increased at cell-cell contacts upon externally applied stretch (vol 109, 12568, 2012). *P Natl Acad Sci USA* **109**, 19034-19034 (2012).

17. Wang, X. & Ha, T. Defining single molecular forces required to activate integrin and notch signaling. *Science* **340**, 991-994 (2013).

18. Stabley, D.R., Jurchenko, C., Marshall, S.S. & Salaita, K.S. Visualizing mechanical tension across membrane receptors with a fluorescent sensor. *Nat Methods* **9**, 64-67 (2012).

19. Liu, Y., Yehl, K., Narui, Y. & Salaita, K. Tension Sensing Nanoparticles for Mechano-Imaging at the Living/Nonliving Interface. *J Am Chem Soc* **135**, 5320–5323 (2013).

20. Jurchenko, C., Chang, Y., Narui, Y., Zhang, Y. & K., S. Integrin Generated Forces Lead to

Streptavidin-Biotin Unbinding in Cellular Adhesions. *Biophys J* **106**, 1436-1446 (2014).

21.   Morimatsu, M., Mekhdjian, A.H., Adhikari, A.S. & Dunn, A.R. Molecular Tension Sensors Report Forces Generated by Single Integrin Molecules in Living Cells. *Nano Lett* **13**, 3985-3989 (2013).

22.   Xia, T., Li, N. & Fang, X. Single-molecule fluorescence imaging in living cells. *Annu Rev Phys Chem* **64**, 459-480 (2013).

23.   Henriques, R., Griffiths, C., Rego, E.H. & Mhlanga, M.M. PALM and STORM: Unlocking Live-Cell Super-Resolution. *Biopolymers* **95**, 322-331 (2011).

24.   Woodside, M.T. *et al.* Nanomechanical measurements of the sequence-dependent folding landscapes of single nucleic acid hairpins. *Proc Natl Acad Sci USA* **103**, 6190-6195 (2006).

25.   Liphardt, J., Onoa, B., Smith, S.B., Tinoco, I., Jr. & Bustamante, C. Reversible unfolding of single RNA molecules by mechanical force. *Science* **292**, 733-737 (2001).

26.   Liu, B., Chen, W., Evavold, B.D. & Zhu, C. Accumulation of Dynamic Catch Bonds between TCR and Agonist Peptide-MHC Triggers T Cell Signaling. *Cell* **157**, 357-368 (2014).

27.   Englund, E.A. *et al.* Programmable multivalent display of receptor ligands using peptide nucleic acid nanoscaffolds. *Nat Commun* **3**, 614 (2012).

28.   Liu, S. Radiolabeled Cyclic RGD Peptides as Integrin alpha(v)beta(3)-Targeted Radiotracers: Maximizing Binding Affinity via Bivalency. *Bioconjugate Chem* **20**,

2199-2213 (2009).

29.   Narui, Y. & Salaita, K. Membrane tethered delta activates notch and reveals a role for spatio-mechanical regulation of the signaling pathway. *Biophys J* **105**, 2655-2665 (2013).

30.   Tan, W., Wang, K. & Drake, T.J. Molecular beacons. *Curr Opin Chem Biol* **8**, 547-553 (2004).

31.   Chen, W., Evans, E.A., McEver, R.P. & Zhu, C. Monitoring receptor-ligand interactions between surfaces by thermal fluctuations. *Biophys J* **94**, 694-701 (2008).

32.   Evans, E., Ritchie, K. & Merkel, R. Sensitive Force Technique to Probe Molecular Adhesion and Structural Linkages at Biological Interfaces. *Biophys J* **68**, 2580-2587 (1995).

33.   Chesla, S.E., Selvaraj, P. & Zhu, C. Measuring two-dimensional receptor-ligand binding kinetics by micropipette. *Biophys J* **75**, 1553-1572 (1998).

34.   Galush, W.J., Nye, J.A. & Groves, J.T. Quantitative fluorescence microscopy using supported lipid bilayer standards. *Biophys J* **95**, 2512-2519 (2008).
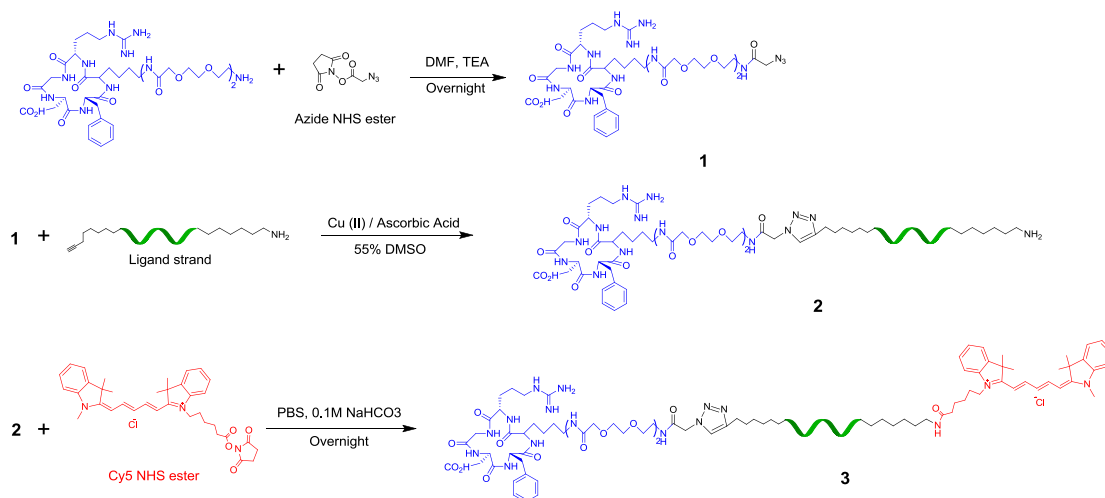
Figure A2.1 Synthesis of the c(RGDfK(PEG-PEG)) ligand strand with Cy5/Cy3B/Atto647N (Cy5 shown as an example). The fluorescently labeled cyclic-peptide-oligonucleotide conjugate was generated in a three-step procedure. In the first step, the primary amine of the c(RGDfK(PEG-PEG)) peptide was activated with an azide group by coupling 100 nmoles of the peptide with 150 nmoles of azide-NHS linker in 10 μL of DMF. To this reaction mixture, 0.1 μL of neat triethylamine was added as an organic base, and the reaction was allowed to proceed for 12 h. The product, **1**, of this reaction was purified by reverse phase HPLC (Figure A2.3a) (flow rate 1 mL/min; solvent A: 0.1 M TEAA, solvent B: 100% acetonitrile; initial condition was 10% B with a gradient of 0.5% per min). The yield of the reaction was determined to be 99% by integrating the HPLC peaks. MALDI-TOF MS was then used to confirm the mass of the product. In the following step, the peptide was coupled to the oligonucleotide using a 1,3-dipolar cycloaddition "click" reaction and following the manufacturer's protocols listed on the Lumiprobe corporation website. Briefly, 20 □L reaction buffer containing 500 mM alkyne-modified ligand strand, 750 mM product **1**, 0.5 mM ascorbic acid, 0.5 mM Cu-TBTA (Tris[(1-benzyl-1H-1,2,3-triazol-4-yl)methyl]amine) complex and 50% DMSO. This reaction was allowed to proceed for 12 h. After purification using a P4 gel, the product, **2**, was separated from unlabeled oligonucleotides by HPLC (Figure A2.3b) (flow rate 1 mL/min; solvent A: 0.1M TEAA, solvent B: 100% acetonitrile; initial condition was 10% B with a gradient of 1% per min), and confirmed by MALDI-TOF MS. In the final step, the fluorescent dye, Cy5-NHS or Cy3B-NHS, was coupled to the 3' amine group of DNA-peptide conjugate, **2,** by adding 1 μL of 1 mM DNA and 1 μL of 1 M sodium bicarbonate to 7 μL of PBS. Then, 1 μL of 10 mM dye-NHS ester (10-fold molar excess) was added to the DNA mixture. The reaction was allowed to incubate at room temperature overnight. After P4 gel purification, the product, **3**, was separated from **2** by HPLC while monitoring channels at 260/640 nm or 260/560 nm (Figure A2.3c) (flow rate 1 mL/min; solvent A: 0.1M TEAA, solvent B: 100% acetonitrile; initial condition was 10% B with a gradient of 1% per min). The final product was verified by MALDI-TOF MS. Synthesis of the

Gly-Arg-Gly-Asp-Ser ligand strand with Cy5/Cy3B/Atto647N was generated using a similar procedure to that used for the cyclic peptide coupling (*vide supra*). HPLC and MALDI-TOF were used to verify the final product. The quencher-oligonucleotide conjugate was generated using a similar procedure to that used for generating the Cy5/Cy3B coupled oligonucleotides. HPLC and MALDI-TOF were used to verify the final product (Table A2.1).
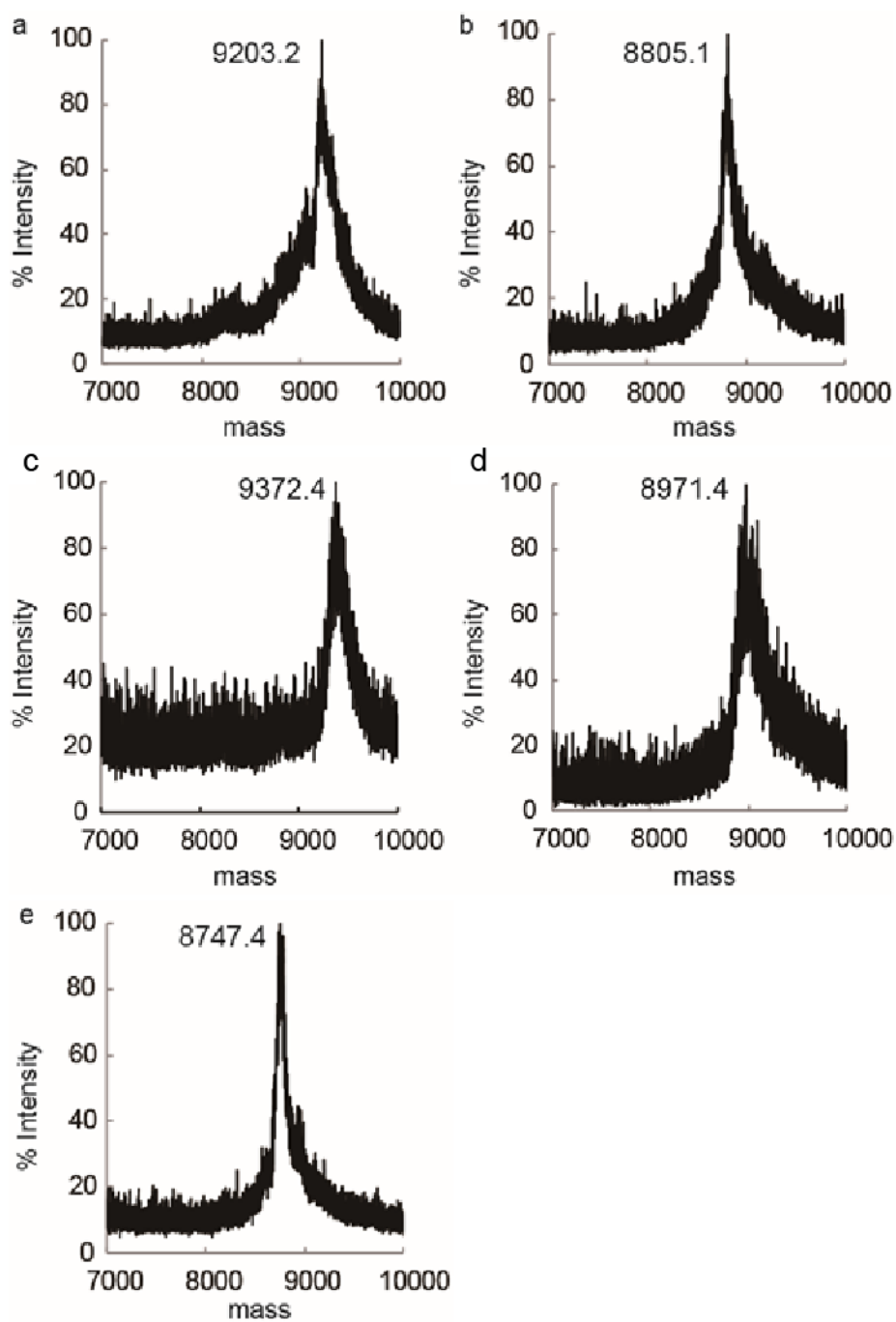
Figure A2.2 Representative MALDI-TOF spectra. (a) c(RGDfK(PEG-PEG))-ligand strand-Cy5, (b) Gly-Arg-Gly-Asp-Ser-ligand strand-Cy5, (c) c(RGDfK(PEG-PEG))-ligand strand-Cy3B, (d) Gly-Arg-Gly-Asp-Ser-ligand strand-Cy3B, and (e) QSY 21 labeled anchor oligonucleotide strand.
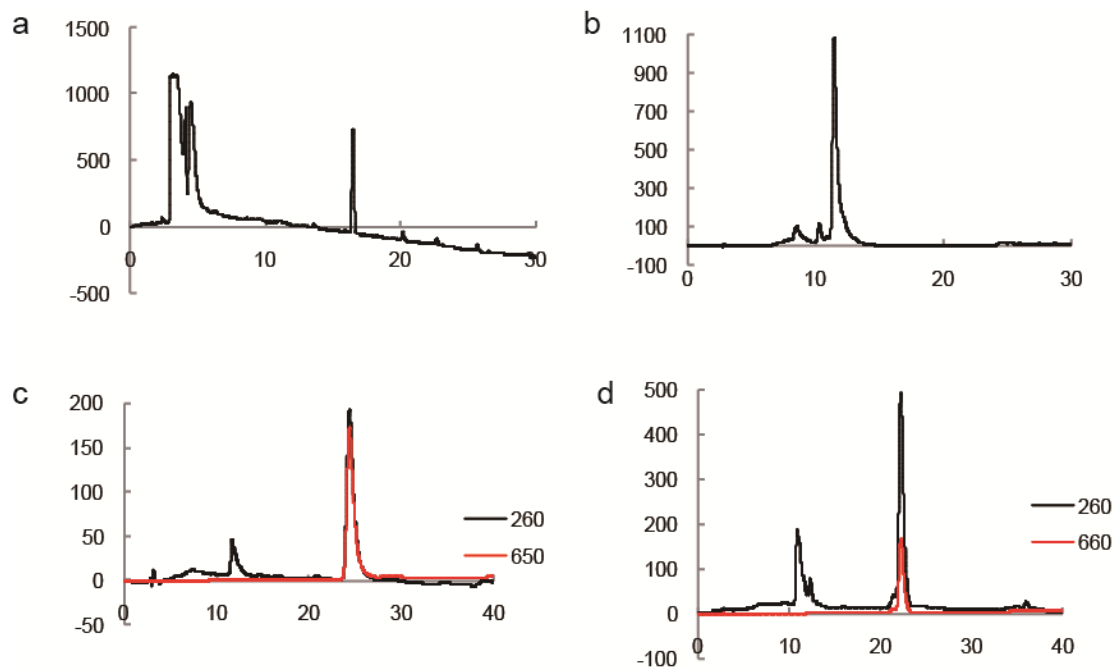
Figure A2.3 Representative HPLC traces of reactions used to generate oligonucleotide conjugates. (a) product 1, (b) product 2, and (c) product 3. HPLC trace in d is representative of the products of the QSY 21 anchor oligonucleotide coupling reaction.
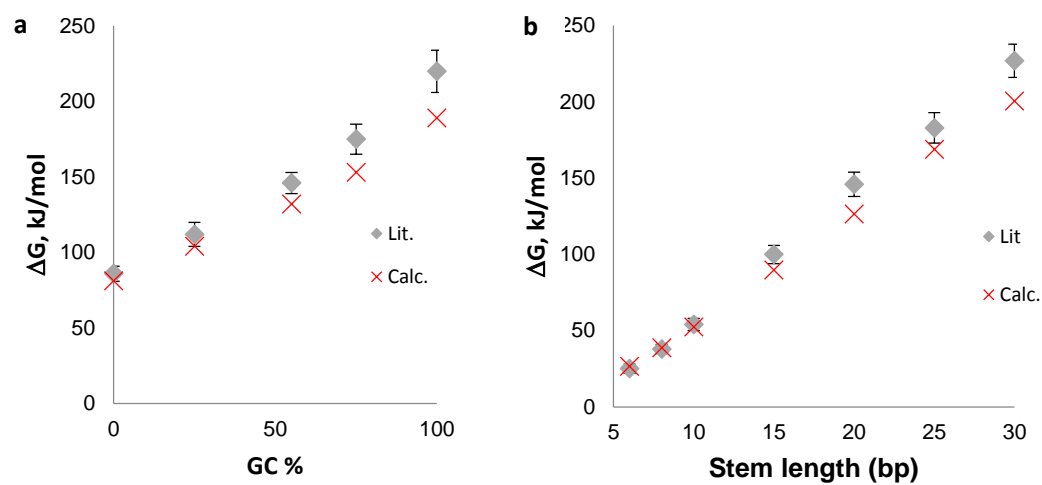
Figure A2.4 Comparisons of calculated total free energy associated with hairpin unfolding using $\Delta G = \Delta G_{IDT} + \Delta G_{stretch}$ with the published data from Woodside et al. Plots showing the total change in free energy of unfolding a hairpin as a function of GC content (a), and stem length (b). Gray diamonds represent the values obtained from Woodside et al., while the red x indicates calculated free energy values in this work.
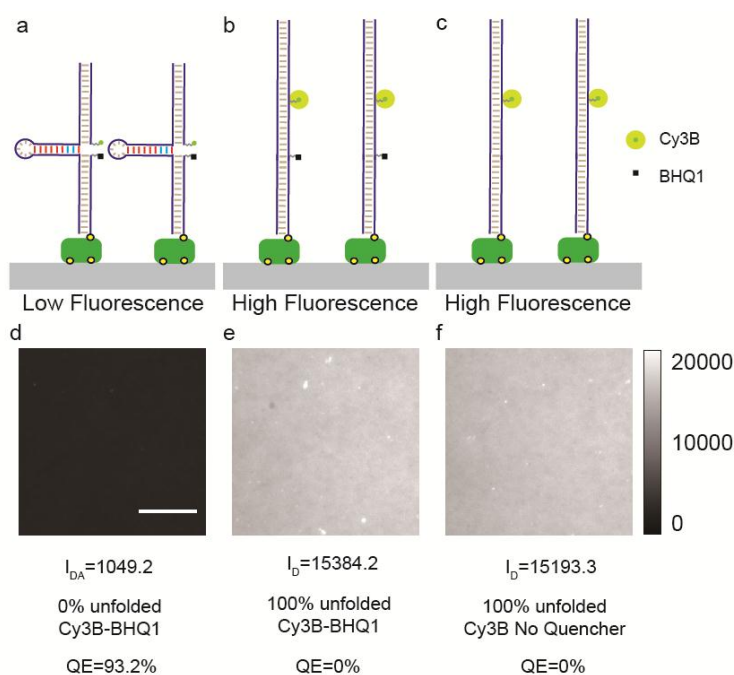
Figure A2.5 Determination of dye quenching efficiency as a function of hairpin folding. To show that the dye is completely dequenched when the hairpin is unfolded, we compared the fluorescence intensity of the probe with and without the quencher. (a, d) Representative fluorescence image of a probe surface with the folded (closed) hairpin tagged using the Cy3B-BHQ1 fluorophore-quencher pair. The quenching efficiency (QE) of this sample was ~93%. (b, e) Representative fluorescence image of an opened (or unfolded) tension probe surface where the Cy3B and BHQ1 fluorophore and quencher pair was separated by hybridization with a complementary strand to the hairpin region. (c, f) Representative fluorescence image of a substrate modified with a probe similar to the one used in (b) but lacking the quencher. By comparing the fluorescence intensity of (b) and (c) we note little difference between samples, indicating that Cy3B is fully dequenched when the hairpin is fully opened. Note that a mechanically-denatured ssDNA hairpin is likely to be extended a greater distance than the duplex probe distance. Therefore, force-induced opening of the tension probes will likely lead to full recovery of the fluorophore intensity.
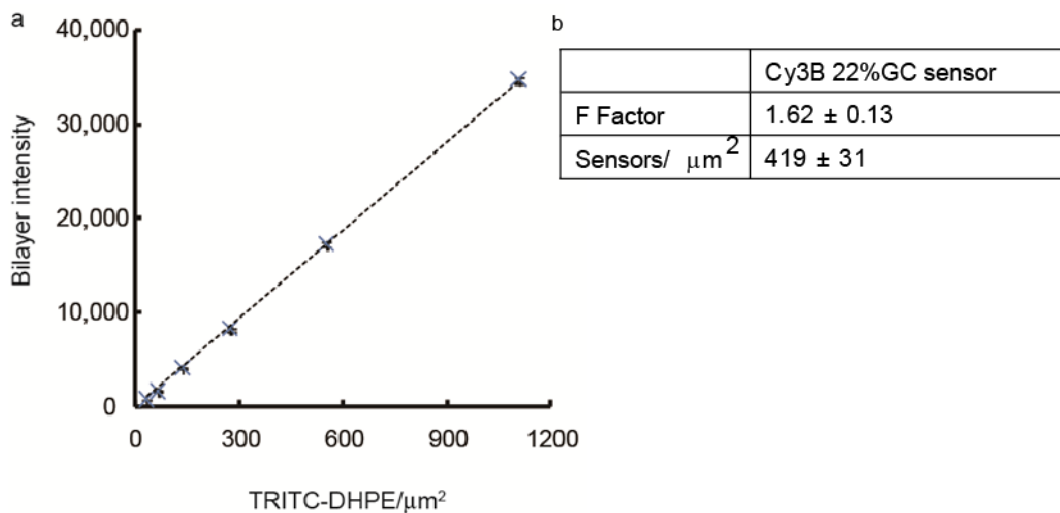
Figure A2.6   Calibration curve for converting fluorescence intensity to molecular density. (a) Plot shows a calibration curve relating the fluorescence intensity of TRITC-DHPE – doped supported lipid membranes to their molecular density. (b) Table showing the F factor value, which relates the brightness of Cy3B 22% GC tension probes to that of TRITC-DHPE using a fluorescence microscope.   By using the calibration curve in (a) and the F factor, we determined that the molecular density of Cy3B 22% GC tension probes was 419 ± 31 sensors/ μm^2. This error represents the standard deviation in molecular density across three different substrates.
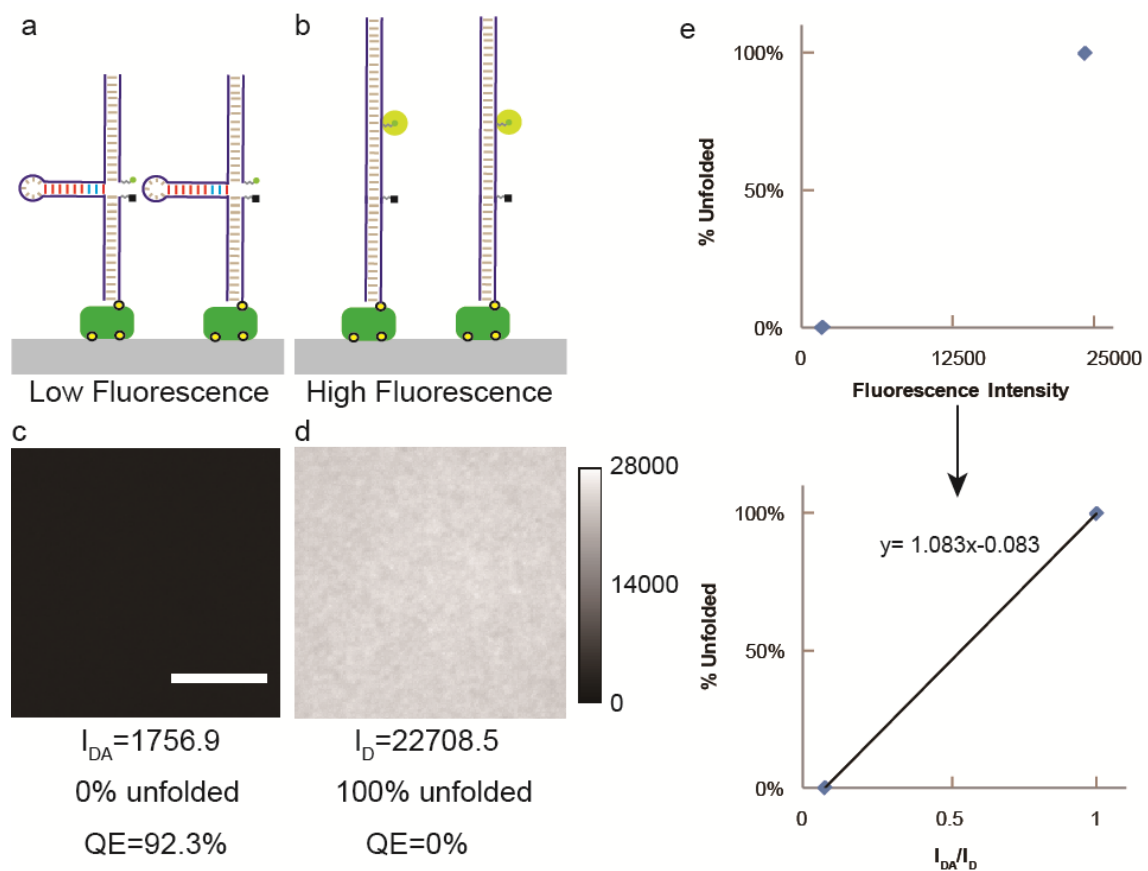
Figure A2.7 Representative example showing how QE (1- I_{DA}/I_D) and % unfolded were determined for tension probes immobilized onto glass substrates. (a, b) Schemes showing closed and open MTFM tension probe surfaces. (c, d) Representative fluorescence images and quantitative intensity scale bar for the probes shown in (a) and (b). Scale bar is 10 μm. The corresponding unfolding percentage and QE values for each image are indicated below. Data was obtained using the Cy3B channel in a multiplexed tension probes experiment displaying different values of $F_{1/2}$. (e) The conversion function was calculated from the data acquired from c and d: % unfolded = (1.083×I_{DA}/I_D - 0.083)×100.
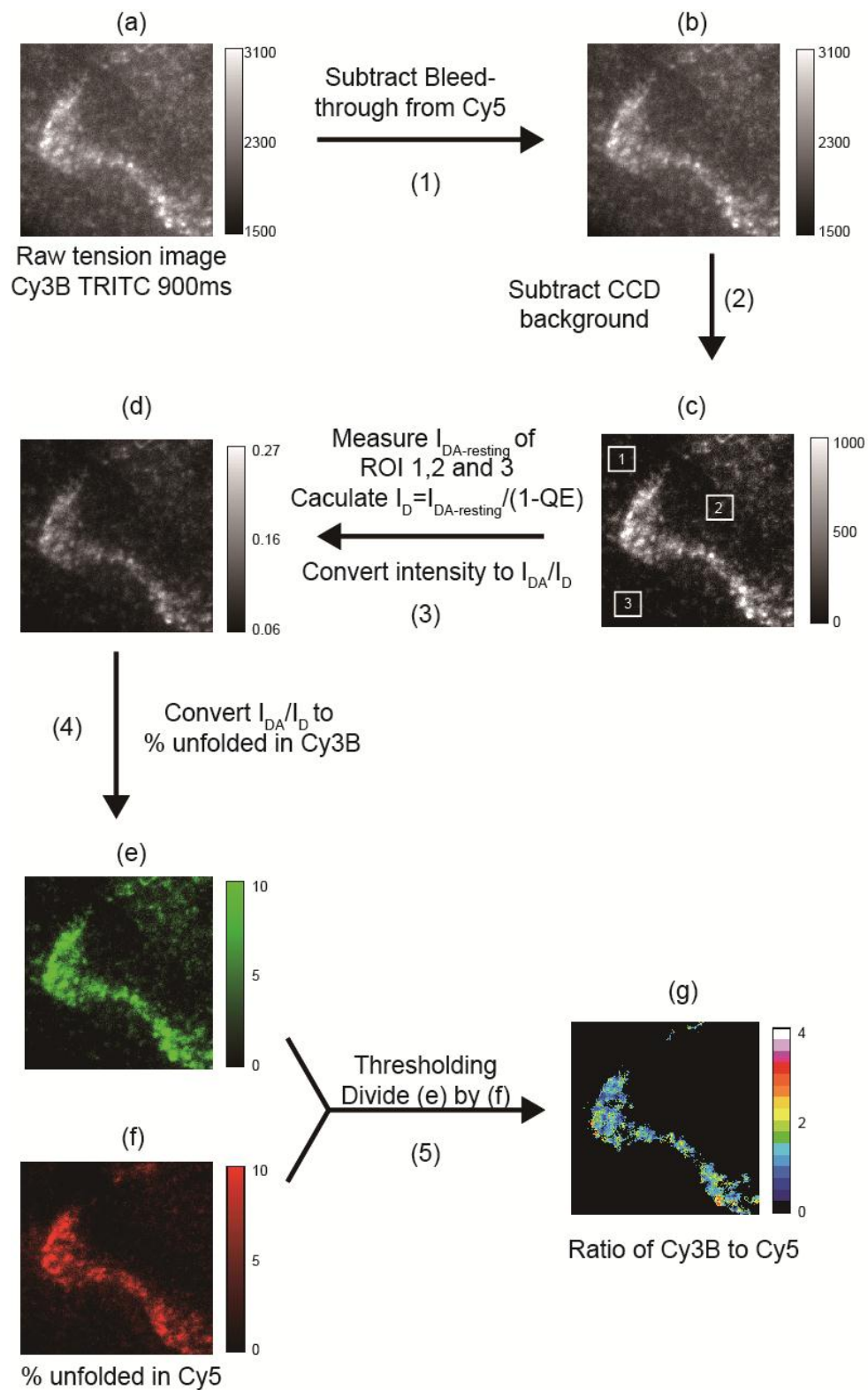
Figure A2.8 Flow chart describing the steps to convert fluorescence intensity to % unfolded. See detailed steps in following section. Scale bar 10 μm.

Fluorescence images were converted to "unfolding percent" images by using the following steps (Figure A2.8):

1) Collect raw fluorescence images of from cells cultured on MTFM DNA-based probes using indicated imaging parameters (see Imaging Parameters section below) (Figure A2.8a).

2) For multiplexed sensors, subtract bleed-through from other dyes yielding Figure A2.8b. A bleed-through coefficient was determined by imaging one fluorescent probe (Cy3B, for example) using the alternate filter cube set (Cy5, for example). The bleed-through coefficients are listed in the Imaging Parameters section below.

3) Subtract EMCCD instrumental background from Figure A2.8b to obtain Figure A2.8c.

4) Determine the fluorescent intensity of the folded hairpin at resting ($I_{DA-resting}$) by averaging three regions of interest (box 1, 2 and 3 within Figure A2.8c). Then, divide $I_{DA-resting}$ by (1-QE), thus yielding the fluorescence intensity of fully de-quenched surface (I_D). Subsequently, divide the fluorescence intensity (Figure A2.8c) by I_D, thus yielding an image with values of I_{DA}/I_D, which is the de-quenching efficiency (Figure A2.8d).

5) Convert I_{DA}/I_D image (Figure A2.8d) to % unfolded by applying predefined conversion function (see Methods Imaging Parameter and Tables A2.5-A2.9).

6) Repeat the steps outlined above for other fluorescence channels in multiplexed probe experiments. Then, threshold the two images and divide to obtain the ratio of unfolded probes in each channel. Typically, the % unfolded from larger magnitude $F_{1/2}$ probes was divided by the % unfolded image from probes with lower values of $F_{1/2}$.
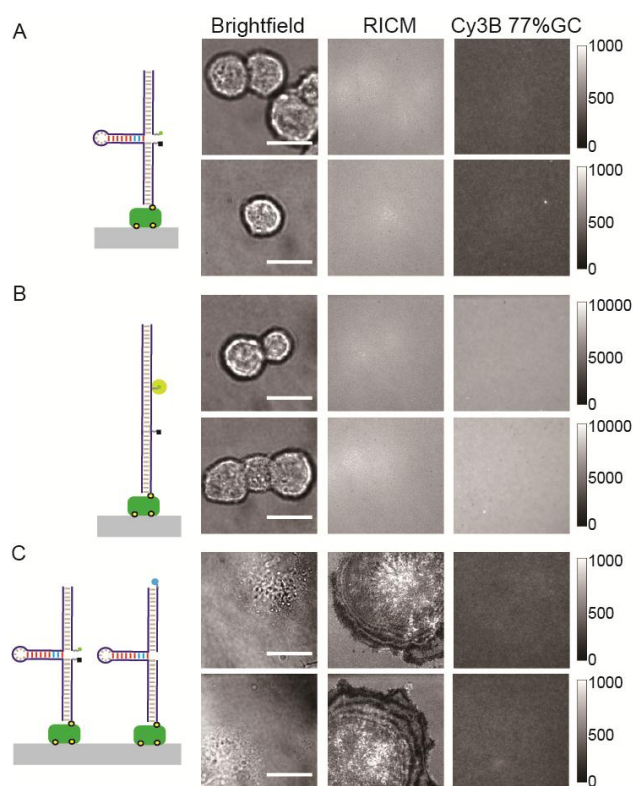
Figure A2.9   Control experiments showing that tension signal is specific to RGD-integrin interactions. (a) Representative brightfield, RICM, and fluorescence images of cells plated on quenched sensors lacking adhesive RGD peptides for 30 min. No RICM signal or increase in fluorescence signal was observed for all cells imaged. (b) Representative brightfield, RICM, and fluorescence images of cells plated on sensors opened by their complementary strands and lacking the RGD peptides. No cell attachment or fluorescence response was observed after 30 minutes of cell incubation. (c) Representative brightfield, RICM, and fluorescence images of cells incubated on a binary mixture of probes, one lacking the RGD peptide, and the second lacking the fluorophore-quencher reporter pair. Cells adhered and spread in this case, but no fluorescence signal was observed after 30 min of cell seeding. Scale bar is 20 μm.
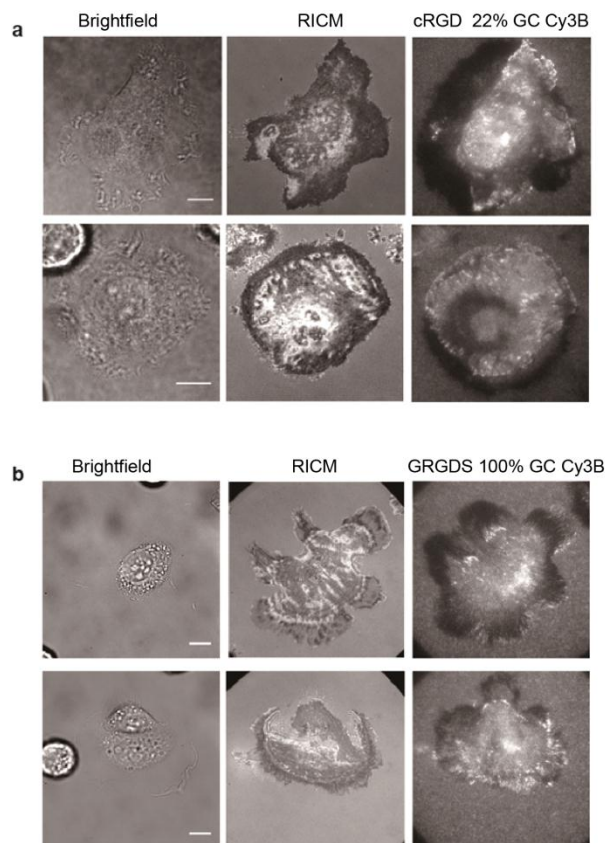
Figure A2.10   Loss of fluorescence signal due to prolonged cell incubation. (a) Representative brightfield, RICM, and fluorescence microscopy images of cells incubated on 22% GC tension probes displaying cyclic RGD peptide for 1 hour. (b) Representative brightfield, RICM, and fluorescence microscopy images of cells incubated on 100% GC tension probes displaying linear GRGDS peptide for 1 hour. Fluorescence intensity values that are below that of the closed probe appeared under specific regions near the cell, and typically corresponded to cell migration history. Scale bar is 10 μm.
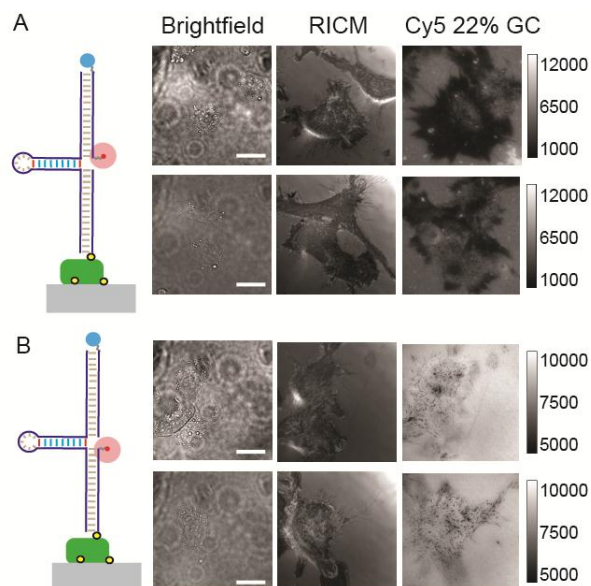
Figure A2.11 Determining the cause of fluorescence signal loss after prolonged cell incubation. (a) Control tension probes were synthesized with Cy5 fluorophore coupled to the ligand strand of the sensor, while the anchor strand lacked the quencher. Representative brightfield, RICM, and fluorescence images indicate significant loss of fluorescence signal under cells that were incubated for ~ 1 hr. This suggests dissociation of the upper strand containing the dye. (b) Control tension probes were synthesized with Cy5 fluorophore conjugated to the anchor strand of sensor lacking a quencher. Representative brightfield, RICM, and fluorescence images indicate slight loss of fluorescence within punctate regions under cells incubated for ~ 1 hr. This suggests that the anchor strand generally remains in tact at this time point. We speculate that this loss of fluorescence intensity is due to cell-generated nucleases. Scale bar is 20 μm.
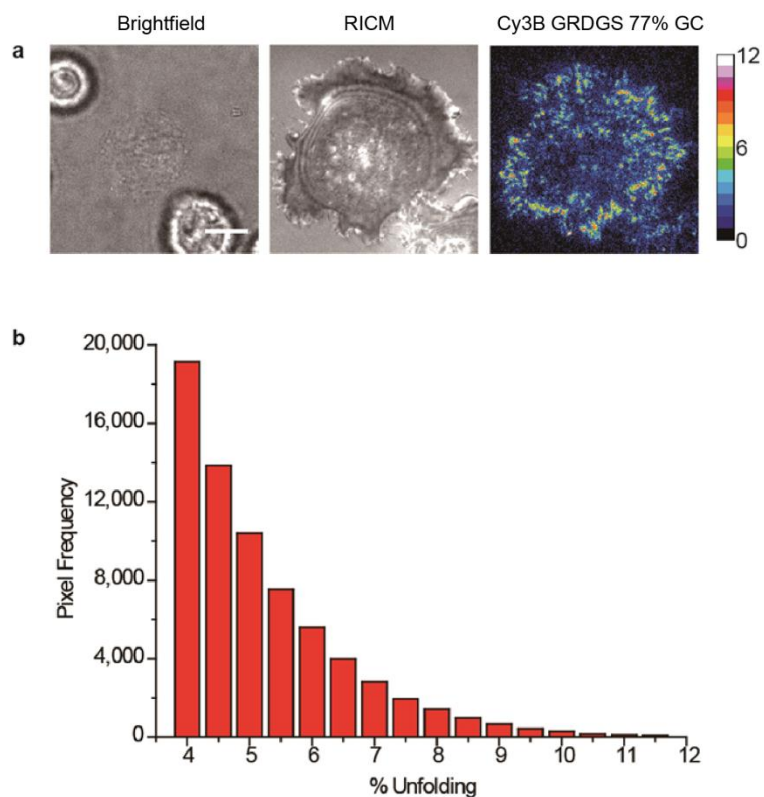
Figure A2.12   Integrin mechanical response on 77% GC tension probe surface exclusively displaying the linear GRGDS peptide. (a) Representative brightfield, RICM and % unfolded map of a cell cultured on the 77% GC tension probe surface for 20 min. Scale bar: 10 μm. (b) Histogram showing the frequency of pixels displaying different levels of % unfolding. Data were collected and analyzed from 6 cells. Note that a significant number of the 77% GC probes with GRGDS peptide were unfolded (with % unfolding values ranging from 4-12%) on these surfaces. In contrast, % unfolding values were diminished and ranged from 0-4% when the GRGDS peptide was presented in a binary mixture with cRGD peptides (Fig. 4b), thus showing that integrins display chemo-mechanical specificity.
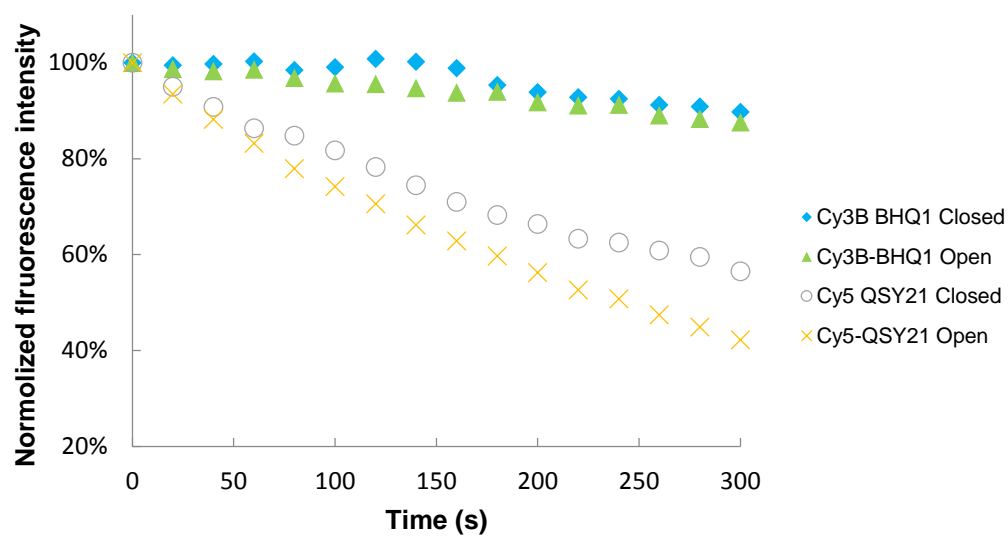
Figure A2.13 Photostability of Cy5-QSY 21 and Cy3B-BHQ1 reporter pairs. Plot shows the fluorescence intensity of MTFM sensors that are in the fully opened or closed conformation. Images were acquired every 20 s using 400 ms exposure time in PBS. Plot indicates better Cy3B photostability in comparison to Cy5.
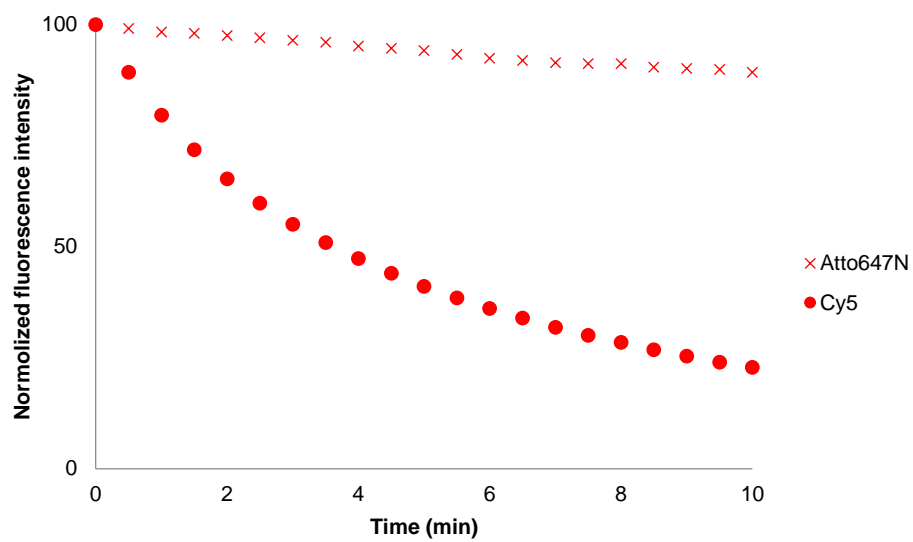
Figure A2.14   Photostability of Cy5 and Atto647N. Plot shows the normalized fluorescence intensity of the Cy5 and Atto647N modified glass slides using a 1 s epifluorescence exposure time. Under these conditions (1 X PBS, RT), Atto647N was much more photostable.
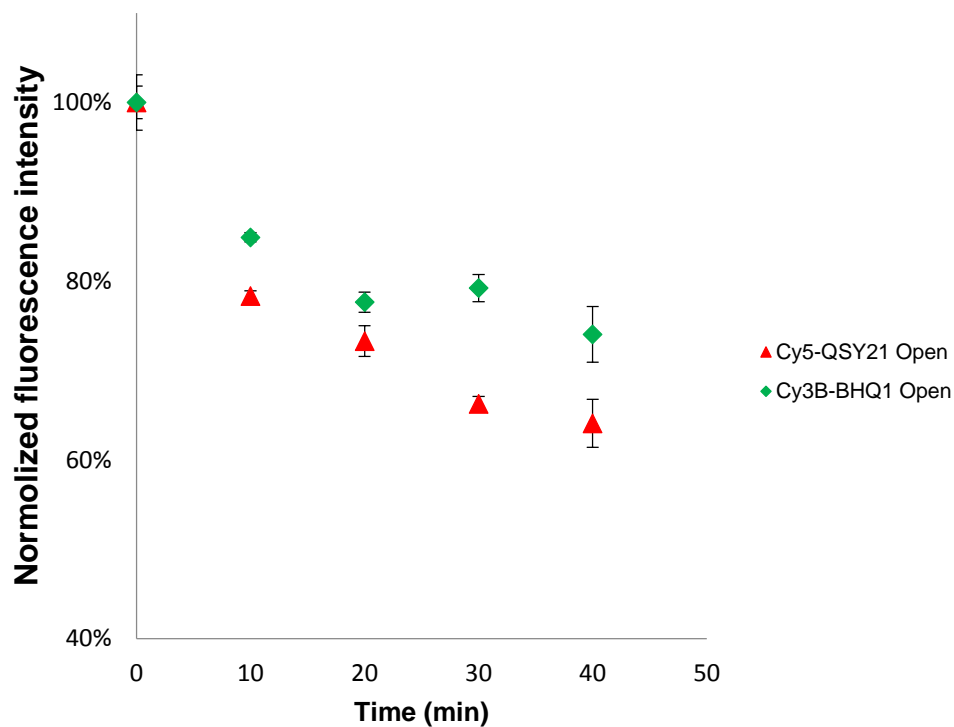
Figure A2.15 Chemical stability of MTFM DNA-based sensors. Plot showing the fluorescence intensity of unfolded sensors (45 mer) for two different fluorophore-quencher pairs. The images were acquired every 10 min, with 400 ms exposure time for Cy3B and 1s exposure time for Cy5. Note that these imaging parameters were identical to the ones used for the cell experiment with multiplexed tension probes. Cy3B demonstrated better chemical stability compared to Cy5 tagged tension probes. To better simulate the cell experiments, we recorded fluorophore stability using cell media (including serum) and also adding cells to the chamber. Cells failed to attach since these sensors lacked the RGD peptide.
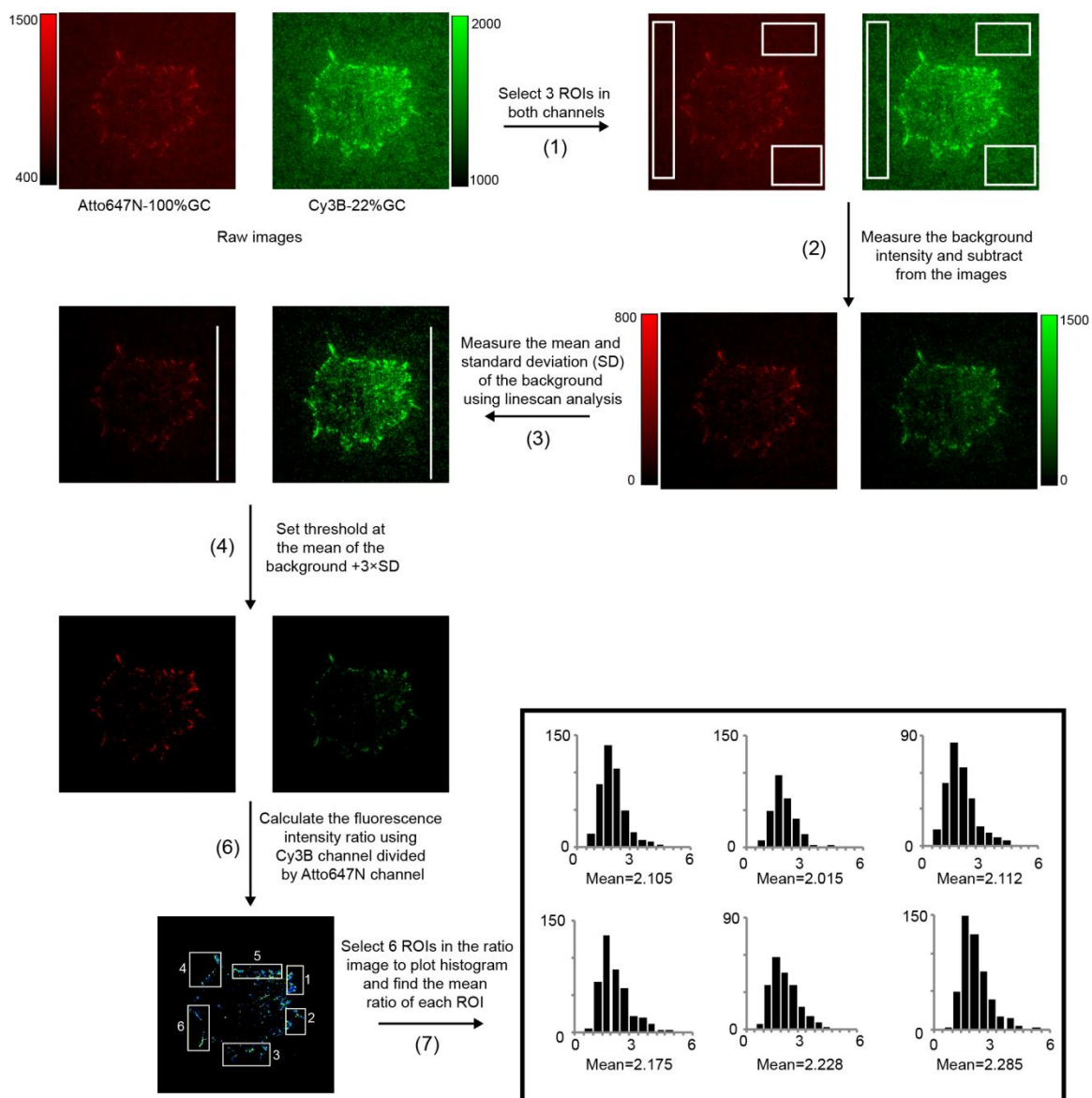
Figure A2.16 Flowchart describing the analysis used to compare the ratio of the signal intensities from the multiplexed probes.
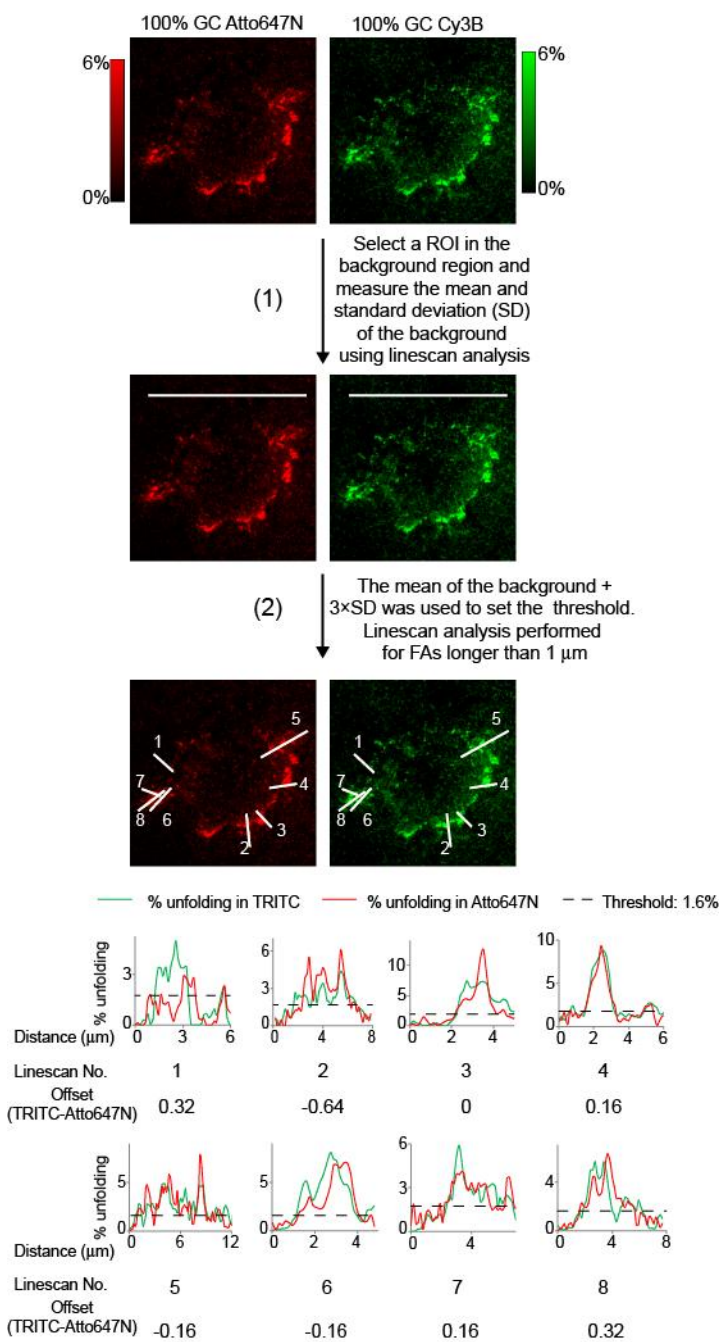
Figure A2.17 Flowchart describing the analysis used to compare the offset of the starting position of the FAs in the two fluorescence channels. This analysis was used to generate the histogram shown in main text Fig. 5e. For the multiplexed probe data set, we subtracted the start position of the tension signal obtained from the 22% GC probe from that of the tension signal in the 100% GC probe channel.
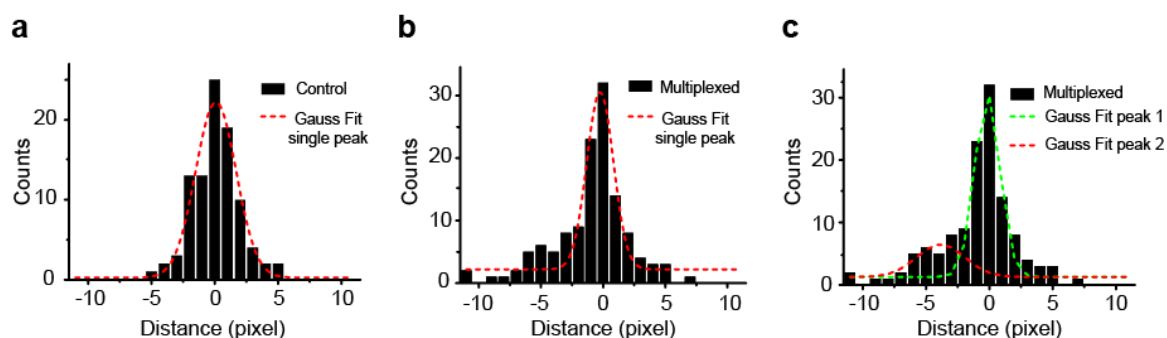
	Control Single Peak Fit		Multiplexed Single Peak Fit		Multiplexed Two Peak Fit			
	Value	Standard Error	Value	Standard Error	Value	Standard Error	Value	Standard Error
y0	0.3	0.4	2.2	0.6	1.3	0.5		
xc	0.1	0.1	-0.24	0.09	-0.2	0.1	-3.8	1.0
w	3.2	0.2	2.1	0.2	2.0	0.2	3.7	2.0
A	88.0	5.8	76.1	6.6	72.6	10.1	24.7	12.5
Reduced Chi-sqr	2.5		5.8		3.3			
Adj.R-Square	0.95		0.90		0.96			

Figure A2.18 Fitting the offset in the start position of tension between the two multiplexed probes. The offset data from control and multiplexed probes was plotted in histograms (Fig. 5e). (**a**) Red dashed line represents the single peak Gaussian fit of the control experiment histogram, where both probes were encoded using 100% GC hairpins. The fit was performed using OriginPro 8.5 data analysis package and the parameters of the fit are shown in the table below. The adjusted R^2 value was 0.95 and the reduced χ^2 value was 2.5, indicating a valid fit to the data. (**b**) Red dashed line represents the single peak Gaussian fit of the multiplexed data. The adjusted R^2 value was 0.90 and the reduced χ^2 value was 5.8 indicating a poor fit for the data when compared to (**a**). To confirm the control and multiplexed histograms represent different distributions, we performed a comparison of the two data sets (F-test) in Origin and found that the two sets are statistically different (p=0.038, which is <0.05). (**c**) To better fit the multiplex histogram, we used two Gaussian functions, which were software generated and are shown in the dashed red and green lines. The center of the red peak was -0.2 ± 0.1 pixels, which is similar to the control center position of 0.1 ± 0.1 pixels. This indicates no difference in the start position of tension in the two the channels. The green peak center position was -3.8 ±1 pixels, indicating that there was a subset of tension signals that displayed the 100% GC probe closer to the cell edge by ~0.5 microns. Based on the adjusted R^2 value (0.96 versus 0.90) and the reduced χ^2 (3.3 versus 5.8), the multiplexed data was more accurately fit to two Gaussian distributions, thus confirming that the two data sets represent distinct populations. 1 pixel= 160 nm.

Table A2.1 MALDI-TOF analysis

Product	MW (calc.)	MW (obs)
c(RGDfK(PEG-PEG))-azide	977.1	970.6
Gly-Arg-Gly-Asp-Ser-azide	573.6	574.2
c(RGDfK(PEG-PEG))-ligand strand	8706.1	8714.2
Gly-Arg-Gly-Asp-Ser-ligand strand	8302.6	8314.1
c(RGDfK(PEG-PEG))-ligand strand-Cy5	9207.3	9203.2
Gly-Arg-Gly-Asp-Ser-ligand strand-Cy5	8803.8	8805.1
c(RGDfK(PEG-PEG))-ligand strand-Atto647N	9434.6	9452.6
c(RGDfK(PEG-PEG))-ligand strand-Cy3B	9357.1	9372.4
Gly-Arg-Gly-Asp-Ser-ligand strand-Cy3B	8953.6	8971.4
QSY 21 labeled anchor strand	8749.8	8747.4

The table summarizes the calculated and observed molecular weights (MW) of all synthesized intermediates and final ligand and anchor strands products used in the current work.

Table A2.2   Calculated force thresholds for hairpins use in the experiment.

ID	Length mer	Sequence	ΔG_{IDT} kJ/mol	$\Delta G_{stretch}$ kJ/mol	ΔG kJ/mol	Δx nm	$F_{1/2}$ pN
22% GC	25	GTA TAA ATG TTT TTT TCA TTT ATA C	12.4	9.5	21.9	8.6	4.2
77% GC	25	GTA CGC GCG TTT TTT TCG CGC GTA C	40.2	9.5	49.6	8.6	9.6
100% GC	28	GCG CGC GCG CGC TTT TGC GCG CGC GCG C	84.4	10.7	95.2	9.9	16.0

Calculated $F_{1/2}$ for 22% GC, 77% GC and 100% GC tension probes at experimental conditions (37 °C, 140.5 mM Na^+ and 0.4 mM Mg^{2+}).

Table A2.3   Verification of the force calculation and assumptions in agreement with prior work

Hairpin		Literature Data (obtained from Woodside et al.)			Calculated Data		
Hairpin name	mer	Δx Nm	$F_{1/2}$ pN	$\Delta G,$ kJ/mol	ΔG_{IDT} kJ/mol	$\Delta G_{stretch}$ kJ/mol	$\Delta G,$calc. kJ/mol
6R50/T4	16	5.1 ±0.3	8.0 ±0.7	25 ±3	20.9	5.6	26.5
8R50/T4	20	7.2 ±0.3	8.4 ±0.6	38 ±3	31.5	7.3	38.8
10R50/T4	24	8.7 ±0.3	10.5 ±0.6	54 ±4	43.4	9.0	52.4
15R53/T4	34	13.6 ± 0.3	12.3 ±0.4	100 ±6	76.5	13.3	89.8
20R50/T4	44	17.8 ± 0.3	13.6 ±0.4	146 ±8	108.8	17.6	126.5
25R52/T4	54	20.9 ± 0.5	14.5 ±0.7	183 ±10	146.8	22.0	168.8
30R50/T4	64	26.5 ± 0.5	14.4 ±0.7	227 ±11	174.3	26.3	200.6
15R60/T3	33	13.0 ± 0.5	10.8 ±0.8	91 ±9	76.0	12.9	88.9
15R60/T4	34	13.5 ± 0.3	13.3 ±0.5	108 ±6	82.9	13.3	96.2
15R60/T6	36	14.8 ± 0.3	11.3 ±0.7	100 ±6	82.9	14.2	97.0
15R60/T8	38	15.2 ± 0.5	10.3 ±0.5	95 ±7	77.5	15.1	92.6
15R60/T12	42	17.3 ± 0.5	9.7 ±0.5	98 ±7	76.7	16.8	93.5
15R60/T15	45	18.6 ± 0.6	9.1 ±0.8	98 ±10	76.0	18.1	94.0
15R60/T20	50	20.8 ± 0.7	8.1 ±0.9	90 ±12	74.4	20.2	94.6
15R60/T30	60	25.7 ±1	7 ±1	96 ±25	70.1	24.6	94.6
20R0/T4	44	17.6 ± 0.3	7.9 ±0.4	86 ±5	63.6	17.6	81.2
20R25/T4	44	17.6 ± 0.4	10.6 ±0.5	112 ±8	86.9	17.6	104.5
20R55/T4	44	18.1 ± 0.3	13.8 ±0.4	146 ±7	115.2	17.6	132.9
20R75/T4	44	19.3 ±	15.2 ±0.5	175 ±10	135.7	17.6	153.4

		0.4					
20R100/T4	44	19.0 ± 0.4	19.3 ±0.8	**220 ±13**	171.4	17.6	**189.1**

Experimental Conditions: 200 mM monovalent salt and 25 °C.

We calculated the free energy of unfolding a library of 20 hairpin sequences that were published in Woodside et al.'s work[24] and benchmarked the results in the following table. We found that the results were in general agreement. Subsets of this library of hairpins highlighting the role of stem length and GC content are plotted in the following figure, thus illustrating the agreement for sequences that are equal to, or less than 25 bases long. Accordingly, we used tension sensor hairpins with total length of approximately 25 nucleotides and stem lengths shorter than 12 base pairs, to ensure the accuracy of $F_{1/2}$.

Table A2.4 Quenching efficiency for different fluorophore-quencher pairs

	BHQ-1 QE%	QSY 21 QE%
Atto647N		94.2% ±0.2%
Cy5		94.9% ±0.1%
Cy3B	95.0% ±0.3%	90.6% ±0.2%
TAMRA	64.9% ±3.6%	86.4% ±0.4%
Alexa Fluor® 488	74.2% ±1.3%	
Fluorescein	62.6% ±3.6%	

Cy3B-BHQ 1, Atto647N-QSY and Cy5-QSY 21 demonstrated the highest QE among these measured pairs.

Table A2.5 Single color Cy3B imaging parameters.

Reporter dye	Cy3B	Cy3B
Hairpin sensor	77%GC, 22%GC	100%GC
Exposure time	400ms	400ms
QE	94.3%	95.0%
Conversion of $\frac{I_{DA}}{I_D}$ (x) to % unfolded(y)	$y = (1.059x - 0.059)*100$	$y = (1.053x - 0.053)*100$

Table A2.6 Dual color Cy3B-100%GC and Cy5- 77%GC, 22%GC imaging parameters.

Reporter dye	Cy3B	Cy5
Hairpin sensor	100%GC	77%GC, 22%GC
Exposure time	400ms	900ms
QE%	92.3%	95.7%
Conversion of $\frac{I_{DA}}{I_D}$ (x) to % unfolded (y)	$y = (1.083x - 0.083)*100$	$y = (1.044x - 0.044)*100$
Bleed through	7.9%	Negligible

Table A2.7 Dual color Cy3B-77%GC, 22%GC and Cy5-100% imaging parameters.

Reporter dye	Cy3B	Cy5
Hairpin sensor	77%GC, 22%GC	100% GC
Exposure time	400ms	900ms
QE%	94.3%	96.6%
Conversion of $\frac{I_{DA}}{I_D}$ (x) to % unfolded(y)	$y = (1.059x - 0.059)*100$	$y = (1.035x - 0.035)*100$
Bleed through	3.6%	Negligible

Table A2.8 Dual color Cy3B-22%GC and Atto647N-100%GC imaging parameters.

Reporter dye	Cy3B	Cy5
Hairpin sensor	22%GC	100%GC
Exposure time	500ms	1s
QE%	92.2%	94.2%
Conversion of $\frac{I_{DA}}{I_D}$ (x) to % unfolded(y)	$y = (1.084x - 0.084)*100$	$y = (1.061x - 0.061)*100$
Bleed through	2.1%	Negligible

Table A2.9 Dual color Cy3B-100%GC and Cy5-22%GC imaging parameters.

Reporter dye	Cy3B	Cy5
Hairpin sensor	100%GC	22%GC
Exposure time	500ms	1s
QE%	92.1%	94.0%
Conversion of $\frac{I_{DA}}{I_D}$ (x) to % unfolded(y)	$y = (1.086x - 0.086)*100$	$y = (1.063x - 0.063)*100$
Bleed through	3.6%	Negligible

Chapter 3   Integrins harness mechanics to trigger platelet activation and aggregation

Adapted from "Platelet Integrins Harness Mechanics to Trigger Activation and aggregation",

manuscript in preparation. Zhang, Y., Qiu, Y., Blanchard, A, Chang, Y., Brockman, J., Lam, W.,

and Salaita, K.

3.1   Introduction

Platelet aggregation, the process by which platelets adhere to each other at the site of vesicular injury, is critical in clot formation. Platelets are recruited and crosslinked through the binding between integrin $\alpha_{IIb}\beta_3$ receptors (60,000-80,000 receptors per cell) and fibrinogen.[1] The clot presents elevated ADP, calcium, and thrombin concentrations that further activate platelets biochemically. Upon activation, platelets release granules and expose phosphatidylserine (PS) facilitating the blood coagulation.[2] Although, the biochemical signaling pathways resulting from integrin-mediated platelet aggregation have been well characterized, much less is known regarding the role of mechanics and mechanotransduction in platelet function.

Platelets are sensitive to mechanical cues. For example, platelets are continuously subjected to hemodynamic forces during circulation and high shear forces can prime platelets and enhance their activation levels.[3, 4] Moreover, platelets interact with fibrin scaffolds within the clot, and are thus exposed to a range of mechanical microenvironments. Recent work by Qiu et al. shows that platelets are sensitive to the stiffness of their surroundings, generating greater levels of activation on stiffer substrates coated with fibrinogen.[5] In fact, soft gels (250 Pa) failed to activate platelets in these experiments. More broadly, soluble fibrinogen in the bloodstream is highly abundant (2 mg/ml) but fails to trigger clotting under normal physiological conditions.[6] Therefore, mechanics modulates the potency of fibrinogen ligands and thus the integrin-mediated platelet junctions are highly mechanosensitive.

In addition, there are several lines of evidence indicating that platelets generate forces upon activation. Lam and coworkers showed that platelets apply a contractile force upon activation that

is proportional to the stiffness of the AFM tip, and this force reaches up to 70 nN per platelet.[7] Traction force microscopy measuring polymer micropillar deformation in response to clot mechanics, estimated that individual platelets exert ~2.1 nN from clots containing hundreds of platelets.[8] Single platelet analysis using traction force microscopy indicated one order of magnitude greater forces of ~34 nN per cell.[9] Taken together, these studies clearly show that platelets apply mechanical forces in response to activation.

Based on the evidences of platelet mechanosensitivity, we investigated the role of mechanical forces in platelet activation and aggregation process. First, we asked whether the ligand mechanics is important to platelet activation. Our hypothesis is that integrin receptors discriminate between soluble and membrane-bound fibrinogen through a mechanosensing process. Presumably, this process requires platelet integrins to test fibrinogen ligands mechanically within the platelet-platelet junctions. Since platelets sense stiffness and apply mechanical forces through integrin receptors, what is the magnitude of platelet integrin force and what are the dynamics of integrin force in space and time? Finally, how is the force related to platelet activation pathways?? The relatively small size of platelets combined with the dynamic nature of platelet adhesion requires techniques with both high spatial discrimination and rapid temporal resolution.

To address these questions, we first investigated the role of ligand mechanics on platelet activation. This was achieved by immobilizing integrin ligands onto a model lipid membrane thus recapitulating the platelet-platelet junction. These experiments demonstrate that the lateral mobility of integrin ligands determines their potency, and suggest an important role for integrin tension in platelet recruitment and activation. Accordingly, we developed molecular tension

probes to map integrin forces during platelet activation. We find that forces are highly dynamic and range from 4-19 pN per receptor. The tension signals show some high-magnitude force puncta at the cell center and a low force region surrounding the lamellipodial rim. This high force center coincides with the region of the platelet that first encounters the substrate. Integrin forces are applied for a duration of 20-30 min and then rapidly terminated as PS is expressed on the cell surface. These experiments demonstrate that platelets fine tune the amount of forces transmitted to their ligands within a narrow range of pN forces. This is significant because the results provide the first molecular tension map of integrins during platelet activation, thus deconstructing the interplay between biochemical and mechanical signaling.

3.2   Results

Given that the platelet-platelet junction is stabilized through integrin-fibrinogen-integrin complexes crosslinked between adjacent cells, we first aimed to investigate the mechanics of the integrin-fibrinogen bond. Fibrinogen is a large, linear, and multi-domain protein and is the major ligand for platelet integrin $\alpha_{IIb}\beta_3$. $\alpha_{IIb}\beta_3$ integrins specifically bind two motifs within fibrinogen: the first is the RGD site on the α subunit and the second is the HHLGGAKQAGDV (AGD) sequence expressed at the carboxyl-terminus of the γ subunit.[10] Minimal peptides that include the AGD or RGD sequences are effective $\alpha_{IIb}\beta_3$ antagonists.[11-15] Accordingly, we used three integrin ligands in our experiments, human full length fibrinogen as well as the two model peptides mimicking fibrinogen binding sequences: cyclic-RGD (cRGD) and AGD (Methods and Figure A3.1 and A3.2).

3.2.1 Lateral ligand fluidity alters platelet adhesion and spreading

We first sought to determine the role of mechanics in initial platelet adhesion. Integrins $\alpha_{IIb}\beta_3$ on the membrane of activated platelets bind soluble fibrinogen from blood flow. These fibrinogen molecules provide adhesion sites that recruit quiescent platelets to the primary clot (Figure 3.1a). To directly test the necessity of force and the role of force in platelet aggregation, we used the hybrid live cell-supported lipid membrane platform. This model platform replaces the activated platelet membrane with a supported lipid bilayer (SLB) displaying integrin $\alpha_{IIb}\beta_3$ bidning ligands (Figure 3.1b).[16] A supported lipid bilayer is comprised of phospholipids that self-assemble onto a planar glass slide. The key advantage of this technique is that ligands are presented in a format that chemically and physically similar to the plasma membrane. The density and mobility of the presented ligands can be fully tuned and the platelet activation response to this input can be directly quantified from the cell adhesion density and spreading areas.[17, 18]
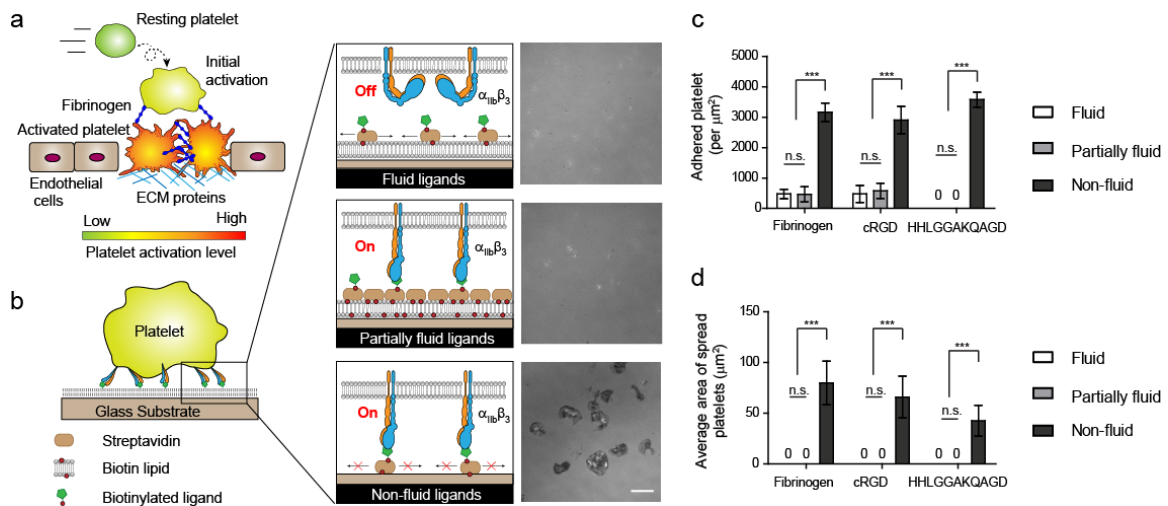
Figure 3.1 Ligand mechanics alter initial platelet activation. (a) Schematic of primary clot recruiting additional platelets from blood flow. (b) Platelet initial activation on a supported lipid membranes (SLBs) is modulated by lateral cRGD ligand fluidity. Representative images of platelets adhering on lipid membranes with different ligand fluidities are shown on the right ("Fluid" denotes ligands on 0.1 % biotin lipid; "Partially fluid" denotes ligands on 4.0 % biotin lipid, and "Non-fluid" denotes ligands immobilized onto the glass surface). Scale bar: 10 μm. (c)

Quantitative analysis of platelet adhesion density on SLBs with different ligand lateral fluidities and different ligand types. (d) Quantitative analysis of platelet spreading area on surfaces with different ligand lateral fluidities and different ligands. (***: $p < 0.001$; n.s.: not significant; n=10 frames for the adhesion density quantification and n=50 cells for the spreading area quantification).

Human platelets were incubated with three integrin ligands (fibrinogen, RGD, and AGD) anchored onto SLBs with different lateral mobilities for 20 min. Figure 3.1b shows representative cell adhesion and spreading on cRGD ligands. When platelets were incubated with a fully fluid SLB, (D ~1-2 μm^2/s), there was minimal cell adhesion with no detectable cell spreading (Figure 3.1c and d). Interestingly, when long-range lipid mobility was hindered ($D = 0.1$ μm^2/s), similar results were observed (Figure 3.1c and d). In contrast, when ligands were covalently immobilized on the substrate ($D = 0.0$ μm^2/s), there was a drastic increase in platelet adhesion and spreading (Figure 3.1c and d). The result indicates that there is an abrupt activation of platelets when their integrin ligands are immobilized compared with ligands that are partially fluid.

Platelets treated with ADP, a soluble platelet agonist localized at the site of the hemostatic plug, displayed adhesion and spreading on the partially fluid SLB, thus rescuing the platelet response to integrin ligands (Figure A3.3). Importantly, fluid ligands still failed to facilitate cell spreading, indicating that activated platelets require mechanical resistance for a complete response.

To further correlate our SLB data with physiological platelet activation event, we directly measured the lateral diffusion coefficient of fibrinogen bound to an activated platelet membrane. Fluorescence recovery after photobleaching (FRAP) experiments with confocal microscopy demonstrated that those bound fibrinogen ligands were non-fluid as the photobleached area did

not show any fluorescence recovery at all (Figure A3.4). This FRAP result successfully links our

lipid data with physiological events.

3.2.2 pN forces are employed for fibrinogen binding and clot retraction

The results presented above demonstrate that ligand mechanics is employed for initial

recruitment of platelets to the primary clot. In addition, it is known that the process of clot

formation requires the mechanical contraction of the platelet aggregate, which occurs following

initial activation (Figure 3.2a). An important question that pertains to these two stages is what is

the magnitude and spatial/temporal distribution of integrin forces during platelet activation. To

investigate this question, we utilized DNA-based molecular tension probes to directly image and

quantify the forces applied by individual platelet integrins upon ligand binding (Figure 3.2b).[19, 20]

In brief, tension probes consisted of a DNA hairpin labeled with a Cy3B-BHQ2

fluorophore-quencher pair. One end of the probe was immobilized onto a glass slide, while the

other terminus was coupled with the cRGD ligand specific for platelet integrin $\alpha_{IIb}\beta_3$. The DNA

hairpin unfolds and generates a 34 ± 2-fold increase in fluorescence when the applied force

exceeds the $F_{1/2}$ (defined as the force at which 50% of hairpins unfold at equilibrium). The $F_{1/2}$

was tuned from 2.4 to 19.0 pN by varying the GC content and stem-loop structure of the hairpins

(Figure 3.2c).

Time-lapse tension response of cells plated on the cRGD probes with $F_{1/2}$ = 4.7 pN was used

to track the process of platelet activation from initial landing to spreading and ending with the

cessation of the tension signal (Figure 3.2d). Within ~2-3 minutes of platelets encountering the

substrate, reflection interference contrast microscopy (RICM) displayed regions of increased

contrast, indicating the association between the cell receptors and the cRGD-coated substrate. This was followed by the appearance of filapodia and increased RICM contrast. Simultaneously, the 4.7 pN tension signal was observed in regions that coincided with intense RICM signal in the center of the contact. Tension signal was also observed along the growing filopodia that extended into permanent attachments. Subsequently, (~4 min after initial contact) the platelet lamellipodia filled in the gaps between the filopodial projections, and displayed a ring-like tension signal at the cell perimeter. The lamellipodia along with the tension signal continued growing until platelets fully spread out with a diameter of ~10 μm within 10 min of the initial contacts.

When the tension signal was integrated, we observed that the total intensity reached a maximum steady level (Figure 3.2e). This plateau was maintained for 20-30 min.[7, 9] Spatial analysis of the steady state tension signal from n=15 human platelets revealed a characteristic ring pattern and a high-intensity central point that coincided with the initial point of platelet-substrate encounter (Figure 3.2f). The lamellipodial ring pattern carried ~40% of the total tension signal, while the vast majority of the remaining signal was localized to the central accumulation point (Figure 3.2e and f). Following the steady state of tension signal, platelets displayed an abrupt and complete loss of tension, which was accompanied by a reduction of the RICM contrast (Figure 3.2e). Taken together, molecular tension probes provide spatial and temporal resolutions which are not achievable by conventional TFM. The revealed platelet mechanical architecture is clearly distinct from that of nuclear cells, such as fibroblasts, epithelial cells, and smooth muscle cells.[21-23]

We next investigated the magnitude of force transmitted by integrin receptors during platelet

activation. TFM indicated a 20-30 nN force per platelet, but given that signaling is mediated by individual integrin receptors, it is important to determine the molecular tension and the heterogeneity of these forces within a single cell. One advantage of using digital DNA-based tension probes is the ability to conveniently test libraries of probes with a range of response thresholds ($F_{1/2}$ values).[20, 24] Given that integrin forces rapidly unfold the 4.7 pN hairpins, we challenged platelets with tension probes of greater $F_{1/2}$ values (13.1 pN and 19.0 pN). Although platelets displayed similar levels of adhesion and spreading on these two probes, the tension signal was 60-70 % weaker (Figure 2g). This shows that the majority of integrins apply force less than 19.0 pN during platelet activation (Figure 3.2g). Importantly, integrin forces are heterogeneous. The lamellipodial edge signal was diminished compared to the central signal on the substrates coated 13.1 pN and 19.0 pN probes (Figure 3.2h). The ratio of the lamellipodial edge signal normalized by the total tension decreased from 0.32 ± 0.05 to 0.15 ± 0.06 and 0.04 ± 0.02, for the 4.7 pN, 13.1 pN and 19.0 pN tension probes, respectively. These results show that integrins at the cell edge experience tension values of less than 19.0 pN, whereas the central region experience forces greater than 19.0 pN.

When the 4.7 pN tension probes were modified with full length fibrinogen and the AGD integrin ligands, we observed differential levels of tension signal. The AGD ligands only generated detectable signal with the 2.4 pN probes which may be due to the weaker affinity of the AGD compared to the cRGD peptides (Figure A3.5). In contrast, full length fibrinogen recapitulated our observations with the 4.7 pN probes, displaying similar spatial patterns of tension (Figure A3.6). However, this tension signal was only qualitative because fibrinogen

crosslinks the biotinylated tension probes and thus each receptor may engage multiple DNA

probes. Taken together, platelets transmit defined pN forces to their integrin ligands in a highly

controlled spatial and temporal pattern.
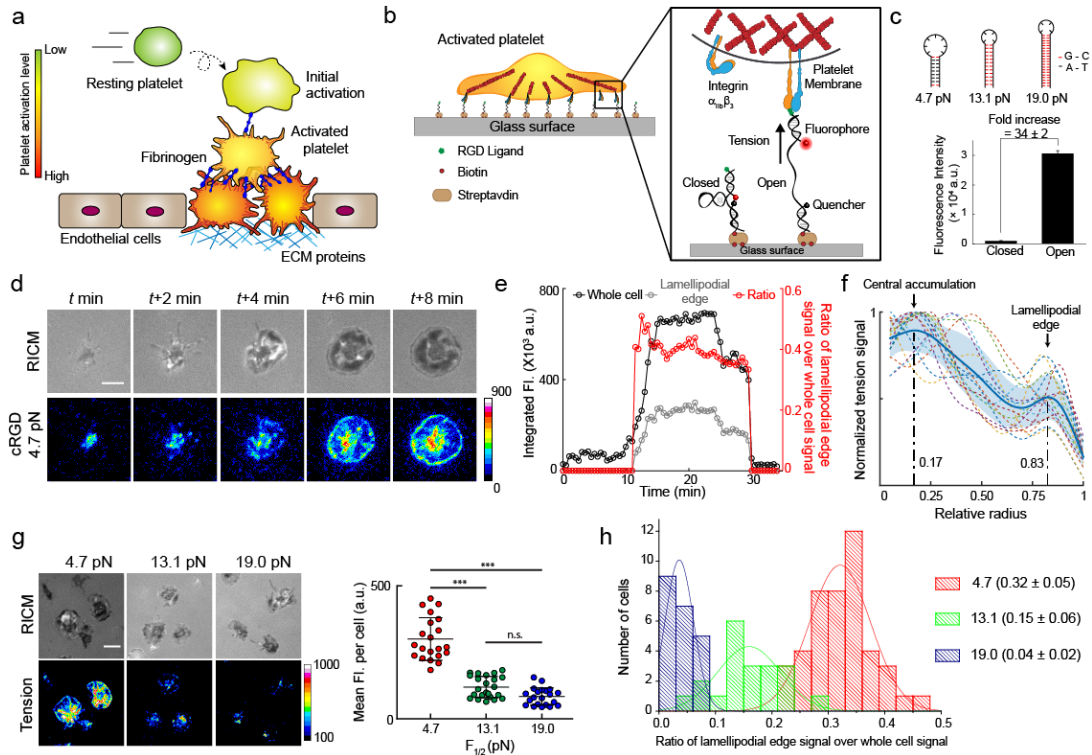
Figure 3.2 Platelets exhibit unique force dynamics during adhesion and spreading. (a) Schematic of an activated platelet forming a stable platelet-platelet junction by integrin $\alpha_{IIb}\beta_3$-fibrinogen complexes. (b) Scheme of DNA-based molecular tension probes for integrin force measurement. (c) Schematic shows the predicted secondary structures of the folded hairpins used in this chapter (top). Bottom plot shows the fluorescence intensities of the closed and open forms of the hairpin. Unfolding of the hairpin generates a 34-fold increase in fluorescence. (d) Representative time lapse RICM and force images as a single platelet spread onto the substrate coated with 4.7 pN tension probes. The intensity of the fluorescence signal indicates the density of unfolded tension probes by integrin forces. Scale bar: 3 μm. (e) The integrated fluorescence signal of the whole platelet and lamellipodium over the time course of platelet spreading in (d). Once the lamellipodia were fully developed, the ratio of lamellipodial signal over the whole platelet signal remained relatively constant. (f) Tension radial intensity profiling of 15 platelets reveals a peak tension at the periphery and a high force zone at platelet center. (g) Representative RICM and force images as the platelets spread on the tension probes with different $F_{1/2}$. The mean fluorescence intensity decreases as the force threshold increases. Scale bar: 5 μm. (h) Spatial distribution of tension with probes of different $F_{1/2}$. The histogram shows the ratio of

lamellipodial tension signal to whole platelet signals decreases as platelets spread onto surfaces with probes of increasing $F_{1/2}$. The shift in the ratio indicates that higher integrin forces exist in the center of spread platelets. (*: p<0.05; **: p<0.01; ***: p<0.001; n.s.: not significant.)

3.2.3 The spatial distribution of platelet tension is regulated by myosin II

phosphorylation pathways

The ability for platelets to generate force is critical in the formation of platelet aggregates.[25] Platelet contractility is driven by myosin II light chain which is regulated by its phosphorylation through myosin light chain kinase (MLCK) and Rho-associated protein kinase (ROCK). To further clarify the role of these two kinases in platelet tension generation, we used pharmacological inhibitors to interfere with myosin activity and recorded the dynamics of integrin tension. Platelets were pre-treated with 0.1 % DMSO (vehicle control), ML-7 (MLCK inhibitor) and Y27632 (ROCK inhibitor) for 1 hr before and then plated onto the 4.7 pN cRGD tension probe surfaces. After 20 min, the DMSO cells displayed similar tension signal as was observed previously (Figure 3.3a and b). In contrast, cells treated with Y27632 displayed diminished tension signal despite adhering and spreading onto the substrates. Platelets treated with ML-7 adhered but failed to spread and to generate tension signal. We also noticed that cells treated with Y27632 lacked strong tension signal in the center (Figure 3.3a). To quantify this observation, we measured the ratio of lamellipodial edge signal over the total tension signal and found this (0.44 ± 0.06) represents a ~20% increase compared to the non-drug treated cells (Figure 3.3c, n = 20 cells). Radial intensity profiling of 25 platelets confirmed this result showing a peak corresponding to the lamellipodial edge but not the center of platelets (Figure 3.3d).

To investigate the role of these two kinases in platelet aggregation and contraction following

the initial adhesion, we tested their effects 20 min after cell activation. ROCK inhibition led to a gradual decrease (within 10 min) in the total tension signal as well as the disappearance of the central tension zone (Figure 3.3e). In contrast, MLCK inhibition dramatically reduced the tension signal (within ~ 1 min) and specially targeted the lamellipodial tension (Figure 3.3f). . Together, these results suggest that RhoA and MLCK kinase signaling pathways have distinct roles in the spatial regulation of myosin II activities and integrin forces. RhoA primarily drives the high magnitude integrin forces at the center of the platelet, while MLCK is necessary for spreading, lamellipodia extension and filopodial protrusion. Inhibiting MLCK, abolishes remodeling of the cytoskeleton, which is critical for platelet spreading and forming stable adhesions.
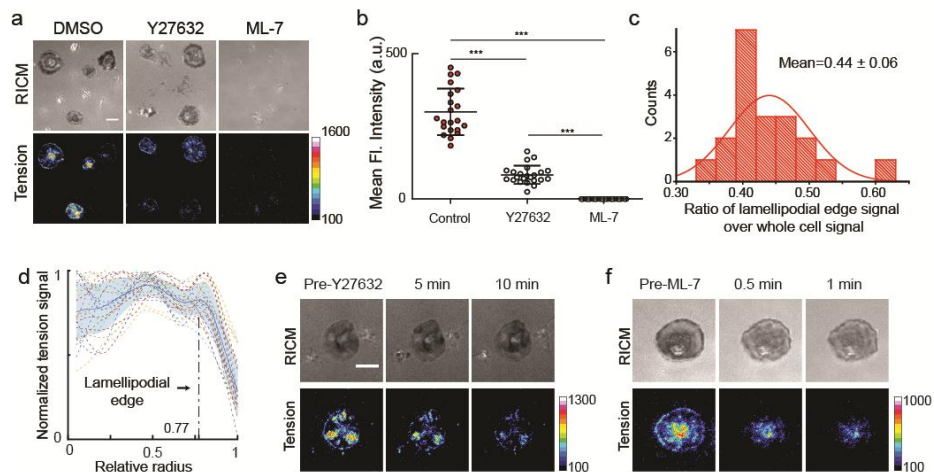
Figure 3.3 Platelet tension during adhesion and spreading is modulated differentially by the MLCK and ROCK pathways in a spatiotemporal manner. (a) Representative RICM and force heat-map images as the ROCK or MLCK inhibitors-pretreated platelets adhered and spread on RGD-tension probes with 4.7 pN $F_{1/2}$. (b) Mean fluorescence intensity of adherent platelets indicates that the ROCK inhibitor Y-27632 decreases the tension intensity while the MLCK inhibitor ML-7 completely eliminates the detection of tension. (c) Histogram of ratios of the lamellipodial edge tension to the whole platelet tension indicates that Y-27632 pretreatment

primarily decreases tension at the platelet center, thereby increasing the ratio to a mean of ~ 0.44. (d) Tension signal radial intensity profiling of 25 individual platelets reveals only one peak at the lamellipodial edge. (e) and (f) show the representative time lapse RICM and force images of platelets treated with ROCK or MLCK inhibitor, respectively.

3.2.4 Correlation of phosphatidylserine exposure with platelet tension

Phosphatidylserine (PS) is a negatively charged lipid typically localized to the inner leaflet

of platelet membrane. PS exposure to the outer leaflet increases the negative charges on the

plasma membrane, promoting platelet procoagulant activity (Figure 3.4a).[2, 26] To investigate the

relationship between chemical and mechanical signalings during platelet activation, we

performed timelapse experiments measuring the PS exposure and integrin tension using confocal

microscopy. The tension signal was recorded with 4.7 pN tension probes while PS levels were

determined using annexin V staining while imaging at a frequency of 3 frames/min. Figure 3.4b

shows three representative cells that were tracked in a single movie. Platelets I and II (highlighted

with white boxes) showed the characteristic abrupt decrease in tension signal occurring 30-50

min after initial activation. This drop in tension signal was associated with a rapid increase of PS

signal. The third platelet in the timelapse continued applying tension without displaying any PS

signal. Quantitative analysis of the temporal delay (Δt) between the loss of tension and the

exposure of PS showed a mean value of 14.7 s for n = 23 cells (Figure 3.4c and d, Figure A3.7).

This demonstrates that platelet tension cessation is upstream of PS exposure during the process of

platelet activation. Three-dimensional reconstruction of platelet morphology during this process

showed that as the tension signal decreased and PS level mounted, cells rounded up which agrees

with observed change in RICM and previous literature (Figure A3.7). This result confirms that PS

exposure follows cytoskeletal reorganization and force modulation.
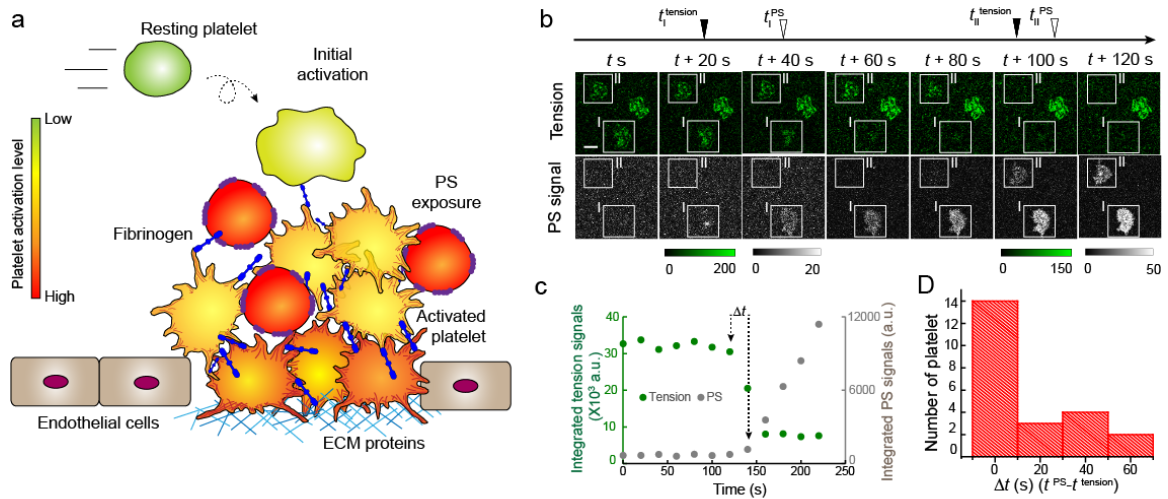
Figure 3.4 Cessation of platelet tension coincides with the exposure of phosphatidylserine (PS). (a) Schematic of PS exposure on the surfaces of active platelets within a clot. (b) Time-lapse movie of platelet tension and PS exposure on the surface conjugated with 4.7 pN tension probes. The PS exposure is measured by fluorescently annexin V staining. Two representative cells are highlighted in the boxes, showing the temporal correlation of tension termination and PS exposure. The platelet in the middle generating strong tension signal did not produce any PS exposure. Scale bar: 2 μm. (c) A time course plot of representative tension and PS intensity signal of platelet I in Figure (b). Δt is defined as the time difference between the time points of tension cessation and PS exposure. (d) The histogram of Δt indicates that tension disappearance occurs simultaneously with the increase in PS signal.

3.3   Discussion

This work aimed to characterize the role mechanical forces in platelet activation and aggregation process. By altering the lateral mobility of platelet ligands, we showed that chemically identical ligands display differential levels of potency depending on their molecular mobility, suggesting platelet initial activation requires mechanical tension. The cell response is pseudo-binary and only immobile ligands triggered platelet activation, in contrast to fluid or partially fluid ligands that failed to trigger platelet spreading. Note that we describe the response appears to be binary because the limits of molecular mobility of ligands required to trigger activation are not clearly defined.

This data supports a new concept, where platelets perform a mechanical checkpoint for activation (Figure 3.5). We speculate that the mechanism mediating this observation is driven by mechanical stabilization of $\alpha_{IIb}\beta_3$ integrin in the open conformation which enhances ligand affinity.[27] This type of response is well documented for $\alpha_5\beta_1$, and likely to be the case for $\alpha_{IIb}\beta_3$.[28] Given that both mobile and hindered ligands are confined in the z-direction (perpendicular to the plasma membrane), this demonstrates that the mechanical checkpoint of ligand is performed in an orientation parallel to the plasma membrane. The result of this mechanical testing is that either the mechanically weak ligands fail in sustaining the ligand-receptor interaction at high affinity state, resulting in the bond dissociation or the mechanically strong ligands provide high resistance forces, stabilizing the integrin at an active state and triggering further platelet adhesion, cytoskeleton reorganization and biochemical signaling pathways.[1] These intracellular signaling events induce inside-out integrin activation and activated $\alpha_{IIb}\beta_3$ integrins bind to fibrinogen. This membrane bound fibrinogen ligands crosslink neighboring activated platelets for clot contraction and also provide adhesion sites for additional platelet recruitment.[29] Importantly, this mechanical checkpoint model may explain how platelets discriminate between soluble fibrinogen and platelet-bound fibrinogen. The mechanical resistance of fibrinogen is likely due to two parameters. First, soluble fibrinogen become immobile once bound to integrins on the surface of activated platelets. Secondly, fibrinogen rapidly polymerizes forming fibrin networks that exhibit significant mechanical stiffness.[30-32] Both of these mechanisms likely contribute to enhancing the fidelity of mechanical testing of fibrinogen to avoid mis-activing platelet during blood flow, since

soluble fibrinogen concentrations exceed 2 mg/ml whereas a stable fibrin gel contains fibrinogen concentrations with at least 100 fold lower concentrations of ligand.[33]

Confirming the transmission of platelet forces to their integrin-ligand complexes, we imaged platelet integrin forces with the highest spatial and temporal resolution reported to date using DNA-based molecular tension probes. We provide the first pN tension maps of integrin $\alpha_{IIb}\beta_3$ during platelet activation. Single platelet integrins transmit forces up to 19 pN with a specific spatial and temporal distribution. Forces accumulate in two zones - a central region with greater tension and a peripheral ring signal along the lamellipodial edge. This is similar to integrin distribution in spread platelets on a fibrinogen-coated surface.[34] TFM measurements of platelets by Henriques et al indicated contractile forces that are maximal at the cell edge.[9] This measurement failed to reveal the central zone of tension likely due to the low spatial resolution of TFM and its inability to readout forces in the Z-direction.

The functional role of the observed high-tension central zone that grows from the initial platelet-substrate adhesion site is unclear. It is possible that platelets flowing within the bloodstream quickly arrest onto the membrane of activated platelets and this initial site allows platelets to firmly take root at the injury site.

The magnitude of tension reported here is derived from individual integrin receptors on the cell surface, thus there are no direct benchmarks reported in the literature. Previous papers reporting on the contractile forces applied by single platelets indicate forces of 29 nN (AFM) and 34 nN (TFM).[7, 9] By estimating the number of hairpins unfolded by a single platelet, we calculated the force per cell is between ~6 nN to ~24 nN, which is consistent with prior reports.

Note this is a lower limit of the total applied force since forces below the $F_{1/2}$ are not included in the analysis and forces significantly exceeding the threshold are also un-estimated.

Pharmacological inhibitors of myosin II allowed elucidating the distinct roles of MLCK and ROCK in controlling the spatial regulation of integrin forces during platelet activation. Interestingly, ROCK inhibition in fibroblasts leads to the loss of stable focal adhesions, and this observation mirrors our findings here that show the loss of the high tension central zone within platelets.[35, 36]

We also determined the temporal relationship between PS exposure, a prerequisite for platelet-dependent thrombin generation, and mechanical signaling. PS-presentation rapidly follows the termination of platelet contraction suggesting that PS-exposing cells do not actively contribute to the clot retraction process.[37-40] This points to a major functional difference between force-generating platelets and PS-presenting platelets with respect to the regulation of coagulation.

Figure 3.5 Proposed the roles of platelet mechanics during its activation and aggregation process. Initial ligand-integrin engagement occurs when a platelet physically encounters fibrinogen at the site of primary clot. During this initial sampling process, platelets perform a mechanical checkpoint for activation with two possible outcomes. The mechanically weak ligands (ligands with high lateral mobility) fail in sustaining the integrin-ligand receptor interaction, resulting in the dissociation of the bond. Or the mechanically strong ligands (immobilized ligands) provide high resistance forces, leading to ligand-receptor interaction at high affinity state and triggering further platelet adhesion and spreading. Biochemical signaling pathways after platelet activation drive the inside-out signaling which switches integrins from an inactive state to an active state. Activated integrins $\alpha_{IIb}\beta_3$ capture the fibrinogen from the blood flow and restrict them with low ligand mobility. These fibrinogen ligands serve as adhesion sites to recruit additional platelets from the blood flow, called platelet aggregation. They also bridge activated platelet together to tighten up the whole clot. After 20-30 min, platelets stop their contraction, detach their cytoskeleton from the membrane and expose PS to initiate the coagulation process. Those PS exposed cells do not participate in further mechanical testing or clot contraction, providing a negative feedback in this mechanical loop.

3.4   Materials and methods

3.4.1 Materials

Human Research Grade Fibrinogen (HCI-0150R) was purchased from Haematologic Technologies. Annexin V, AF488 (A13201) was purchased from Life Technologies. ML-7 (I2764-5MG) and Y27632 (Y0503-1MG) were purchased from Sigma and aliquoted at 30 mM. All amino acids were purchased from AnaSpec (Fremont, CA). Whole Blood Tube w/ Anticoagulant, acid citrate dextrose (ACD) was purchased from BD Vacutainer. Cy3B NHS ester (Product code: PA63101) was purchased from GE Healthcare Life Science (Pittsburgh, PA). Cyclo [Arg-Gly-Asp-d-Phe-Lys(PEG-PEG)] (Product code: PCI-3696-PI, c(RGDfK(PEG-PEG)), PEG = 8-amino-3,6-dioxaoctanoic acid) was acquired from Peptides International (Louisville, KY). Glass coverslips (number 2, 25 mm diameter) were acquired from VWR. Ascorbic acid (>99.0%) and 96-well plates were purchased from Fisher Chemical & Scientific (Pittsburg, PA). DMF (>99.5%), DMSO (99.5%) and sodium bicarbonate (99.0%) were acquired from EMD chemicals (Philadelphia, PA). Sulfuric acid was acquired from Avantor Performance Materials (Center Valley, PA). Ethyl alcohol (EtOH) (200 proof) was purchased from Decon Labs (King of Prussia, PA). 3-aminopropyltriethoxysilane (APTES) and $CH_3(CH_2CH_2O)_{9-12}(CH_2)_3Si(OCH_3)_3$ (mPEG) were acquired from Gelest (Morrisville, PA). Unless otherwise stated, all the other starting materials and reagents were purchased from Sigma-Aldrich and used without further purification. All buffers were made with Nanopure water (18.2 MΩ) and passed through a 0.2 μm filtration system. Anchor strand with BHQ-2 was purchased from Biosearch Technology (Novato, CA). All the other oligonucleotides were custom synthesized and purified by Integrated DNA Technologies (Coralville, IA).

3.4.2 Platelet isolation

Whole blood was drawn from healthy donors into collection tubes with acid citrate dextrose (ACD). Platelet-rich plasma (PRP) was collected after centrifugation under $150 \times g$ for 15 min. Additional ACD was added into PRP (10% of the PRP volume), which was then centrifuged at $900 \times g$ for another 5 min. Platelet-poor plasma was then removed and the platelet pellet was resuspended in Tyrode's buffer containing 0.1% BSA.

3.4.3 Peptide synthesis

AGD Peptides ligands were synthesized following the standard procedure using a Liberty CEM Microwave Automated Peptide Synthesizer (Matthews, NC, USA) and a FMOC-Rink Amide MBHA Resin (AnaSpec, CA, USA). Briefly, Gly, Ala, Asp(OAll), Gln(Trt), Lys(mtt), Leu, His(mtt), Val and 2-(2'-propynyl)alanine were coupled on a CEM Liberty Microwave Synthesizer. FMOC deprotection was completed using 20% piperdine in dimethylformamide at 45-55 ℃ for 180 sec, and washed by 3 times with dimethylformamide. Each amino acid coupling step was performed using 0.1M FMOC protected amino acid and activated with 0.1 M 2-(1Hbenzotriazole-1-yl)-1,1,3,3-tetramethyluronium hexafluorophosphate (HBTU), and 0.2 M N,N –diisopropylethylamine (DIEA) in DMF. Coupling temperatures using microwave were maintained between 75-82 ℃ for 330 sec, then rinsed with three aliquots of dimethylformamide. Final acetylation of the N-terminus was achieved by addition 20% acetic anhydride in dimethylformamide. Resin was filtered and washed with dichloromethane and dried in a vacuum desicator. Peptides were cleaved from dried resin by addition of cleavage cocktail (90 vol% TFA, 5 vol% thioanisole, 3 vol% ethanedithiol and 2 vol% anisole) for 4 hr at room temperature and the resulting filtrate was added drop wise to cold diethylether, centrigued and extracted in

diethylether three more times. Peptides were purified by reverse-phase HPLC (Waters Delta 600) using a Waters Atlantis C-18 preparative column (19 x 250 mm) and employing a linear gradient at 20 mL/min starting at 20% acetonitrile and ending with 55% acetonitrile over 35 min. After removing acetonitrile in rotovap, the peptide fractions were frozen and lyophilized to yield a peptide powder. Product mass was confirmed by MALDI-TOF on a Voyager-DETM STR Biospectrometry Workstation using α-cyano-4-hydroxycinnamic acid (CHCA) as matrix.

3.4.4 Tension signal radial intensity profiling and fitting

The data were acquired by imaging analysis using the Radial Profile Plot Image J plugin, which is available from https://imagej.nih.gov/ij/plugins/radial-profile.html. To account for differences in platelet diameter, we normalized the distance across the platelet by the radius of the platelet (i.e. the center of the platelet and the outer edge of the platelet have a normalized distance of 0 and 1 respectively). To account for differences in fluorescence intensity between platelets, we normalized intensity values by dividing intensity values by the maximum intensity of each line. This gave us normalized intensity vs. normalized distance curves. Due to differences in the number of pixels, we could not take averages between points on different curves to create an average curve. To account for this, we fit each curve to a smoothing spline function using the MATLAB (version 2014b) fit tool. We then generated the average curve (with standard deviation) by finding the average and standard deviation between approximate normalized intensity values generated from 500 normalized distance points along each smoothing spline curve. This was process was performed once each using data from Y27632 treated and untreated platelets, corresponding to Figure 3.2f and Figure 3.3d, respectively.

3.5   References

1.   Joo, S.J. Mechanisms of Platelet Activation and Integrin alphaIIbeta3. *Korean Circ J* **42**, 295-301 (2012).

2.   Heemskerk, J.W., Bevers, E.M. & Lindhout, T. Platelet activation and blood coagulation. *Thromb Haemost* **88**, 186-193 (2002).

3.   Kroll, M.H., Hellums, J.D., McIntire, L.V., Schafer, A.I. & Moake, J.L. Platelets and shear stress. *Blood* **88**, 1525-1541 (1996).

4.   Sheriff, J., Bluestein, D., Girdhar, G. & Jesty, J. High-shear stress sensitizes platelets to subsequent low-shear conditions. *Ann Biomed Eng* **38**, 1442-1450 (2010).

5.   Qiu, Y.Z. *et al.* Platelet mechanosensing of substrate stiffness during clot formation mediates adhesion, spreading, and activation. *P Natl Acad Sci USA* **111**, 14430-14435 (2014).

6.   Weisel, J.W. Fibrinogen and fibrin. *Adv Protein Chem* **70**, 247-299 (2005).

7.   Lam, W.A. *et al.* Mechanics and contraction dynamics of single platelets and implications for clot stiffening. *Nat Mater* **10**, 61-66 (2011).

8.   Liang, X.M., Han, S.J., Reems, J.A., Gao, D. & Sniadecki, N.J. Platelet retraction force measurements using flexible post force sensors. *Lab Chip* **10**, 991-998 (2010).

9.   Schwarz Henriques, S., Sandmann, R., Strate, A. & Koster, S. Force field evolution during human blood platelet activation. *J Cell Sci* **125**, 3914-3920 (2012).

10.   Springer, T.A., Zhu, J.H. & Xiao, T. Structural basis for distinctive recognition of

fibrinogen gamma C peptide by the platelet integrin alpha(IIb)beta(3). *J Cell Biol* **182**, 791-800 (2008).

11.   Basani, R.B. *et al.* RGD-containing peptides inhibit fibrinogen binding to platelet alpha(IIb)beta3 by inducing an allosteric change in the amino-terminal portion of alpha(IIb). *J Biol Chem* **276**, 13975-13981 (2001).

12.   Kloczewiak, M., Timmons, S. & Hawiger, J. Localization of a site interacting with human platelet receptor on carboxy-terminal segment of human fibrinogen gamma chain. *Biochem Biophys Res Commun* **107**, 181-187 (1982).

13.   Sanchez-Cortes, J. & Mrksich, M. The platelet integrin alphaIIbbeta3 binds to the RGD and AGD motifs in fibrinogen. *Chem Biol* **16**, 990-1000 (2009).

14.   Sen Gupta, A. *et al.* RGD-modified liposomes targeted to activated platelets as a potential vascular drug delivery system. *Thromb Haemostasis* **93**, 106-114 (2005).

15.   Srinivasan, R., Marchant, R.E. & Gupta, A.S. In vitro and in vivo platelet targeting by cyclic RGD-modified liposomes. *J Biomed Mater Res A* **93**, 1004-1015 (2010).

16.   Narui, Y. & Salaita, K. Membrane tethered delta activates notch and reveals a role for spatio-mechanical regulation of the signaling pathway. *Biophys J* **105**, 2655-2665 (2013).

17.   Nguyen, T.T., Sly, C.L. & Conboy, J.C. Comparison of the Energetics of Avidin, Streptavidin, NeutrAvidin, and Anti-Biotin Antibody Binding to Biotinylated Lipid Bilayer Examined by Second-Harmonic Generation. *Anal Chem* **84**, 201-208 (2012).

18.   Zou, Z.Y., Chen, H., Schmaier, A.A., Hynes, R.O. & Kahn, M.L. Structure-function analysis reveals discrete beta 3 integrin inside-out and outside-in signaling pathways in

platelets. *Blood* **109**, 3284-3290 (2007).

19. Liu, Y. *et al.* DNA-based nanoparticle tension sensors reveal that T-cell receptors transmit defined pN forces to their antigens for enhanced fidelity. *P Natl Acad Sci USA* **113**, 5610-5615 (2016).

20. Zhang, Y., Ge, C., Zhu, C. & Salaita, K. DNA-based digital tension probes reveal integrin forces during early cell adhesion. *Nat commun* **5**, 5167 (2014).

21. Chang, Y. *et al.* A General Approach for Generating Fluorescent Probes to Visualize Piconewton Forces at the Cell Surface. *J Am Chem Soc* **138**, 2901-2904 (2016).

22. Liu, Y., Yehl, K., Narui, Y. & Salaita, K. Tension sensing nanoparticles for mechano-imaging at the living/nonliving interface. *J Am Chem Soc* **135**, 5320-5323 (2013).

23. Munevar, S., Wang, Y. & Dembo, M. Traction force microscopy of migrating normal and H-ras transformed 3T3 fibroblasts. *Biophys J* **80**, 1744-1757 (2001).

24. Blakely, B.L. *et al.* A DNA-based molecular probe for optically reporting cellular traction forces. *Nat methods* **11**, 1229-1232 (2014).

25. Calaminus, S.D.J. *et al.* MyosinIIa contractility is required for maintenance of platelet structure during spreading on collagen and contributes to thrombus stability. *J Thromb Haemostasis* **5**, 2136-2145 (2007).

26. Lentz, B.R. Exposure of platelet membrane phosphatidylserine regulates blood coagulation. *Prog Lipid Res* **42**, 423-438 (2003).

27. Bennett, J.S. Structure and function of the platelet integrin alphaIIbbeta3. *J Clin Invest*

115, 3363-3369 (2005).

28. Kong, F., Garcia, A.J., Mould, A.P., Humphries, M.J. & Zhu, C. Demonstration of catch bonds between an integrin and its ligand. *J Cell Biol* **185**, 1275-1284 (2009).

29. Li, Z., Delaney, M.K., O'Brien, K.A. & Du, X. Signaling during platelet adhesion and activation. *Arterioscler Thromb Vasc Biol* **30**, 2341-2349 (2010).

30. Ryan, E.A., Mockros, L.F., Weisel, J.W. & Lorand, L. Structural origins of fibrin clot rheology. *Biophys J* **77**, 2813-2826 (1999).

31. Collet, J.P., Shuman, H., Ledger, R.E., Lee, S. & Weisel, J.W. The elasticity of an individual fibrin fiber in a clot. *Proc Natl Acad Sci USA* **102**, 9133-9137 (2005).

32. Brown, A.E., Litvinov, R.I., Discher, D.E., Purohit, P.K. & Weisel, J.W. Multiscale mechanics of fibrin polymer: gel stretching with protein unfolding and loss of water. *Science* **325**, 741-744 (2009).

33. Weisel, J.W. The mechanical properties of fibrin for basic scientists and clinicians. *Biophys Chem* **112**, 267-276 (2004).

34. Jirouskova, M., Jaiswal, J.K. & Coller, B.S. Ligand density dramatically affects integrin alpha IIb beta 3-mediated platelet signaling and spreading. *Blood* **109**, 5260-5269 (2007).

35. Totsukawa, G. *et al.* Distinct roles of MLCK and ROCK in the regulation of membrane protrusions and focal adhesion dynamics during cell migration of fibroblasts. *J Cell Biol* **164**, 427-439 (2004).

36. Totsukawa, G. *et al.* Distinct roles of ROCK (Rho-kinase) and MLCK in spatial regulation of MLC phosphorylation for assembly of stress fibers and focal adhesions in

3T3 fibroblasts. *J Cell Biol* **150**, 797-806 (2000).

37.   Bevers, E.M., Comfurius, P. & Zwaal, R.F. Platelet procoagulant activity: physiological significance and mechanisms of exposure. *Blood Rev* **5**, 146-154 (1991).

38.   Monroe, D.M., Hoffman, M. & Roberts, H.R. Platelets and thrombin generation. *Arterioscler Thromb Vasc Biol* **22**, 1381-1389 (2002).

39.   Heemskerk, J.W., Siljander, P.R., Bevers, E.M., Farndale, R.W. & Lindhout, T. Receptors and signalling mechanisms in the procoagulant response of platelets. *Platelets* **11**, 301-306 (2000).

40.   Heemskerk, J.W., Kuijpers, M.J., Munnix, I.C. & Siljander, P.R. Platelet collagen receptors and coagulation. A characteristic platelet response as possible target for antithrombotic treatment. *Trends Cardiovasc Med* **15**, 86-92 (2005).

Appendix
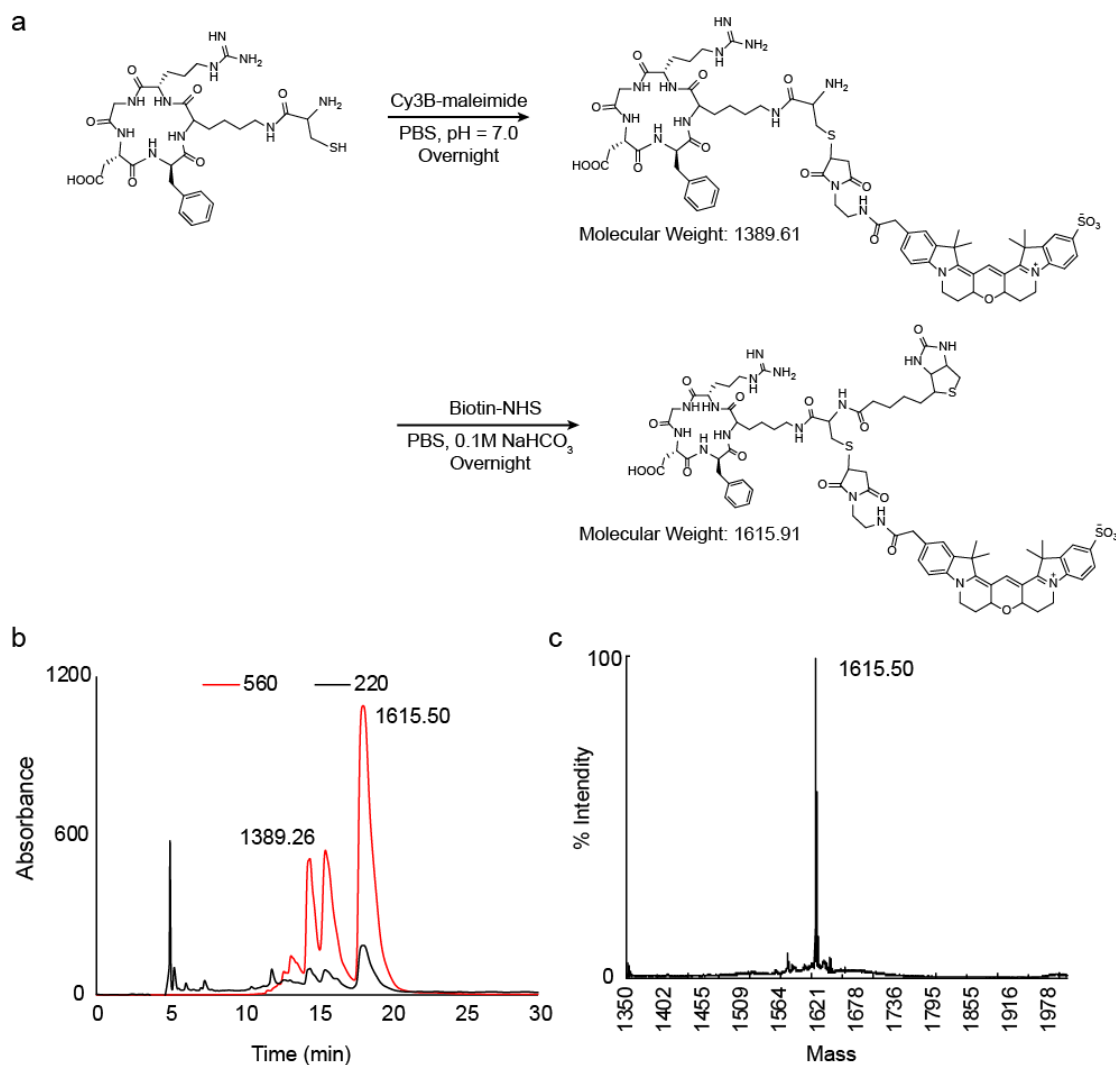
Figure A3.1 Synthesis and characterization of the Cy3B-cRGDfK-biotin ligand for ligand mobility experiment. (a) Steps of Cy3B-cRGDfK-biotin synthesis with expected molecular weights. (b) HPLC of final reaction to purify Cy3B-cRGDfK-biotin. The first two peaks in 560nm channel with characterized mass of 1389.26 are Cy3B-cRGDfK. The peak with characterized mass of 1615.50 is final product of Cy3B-cRGDfK-biotin. (c) MALDI spectrum for final product of Cy3B-cRGDfK-biotin.
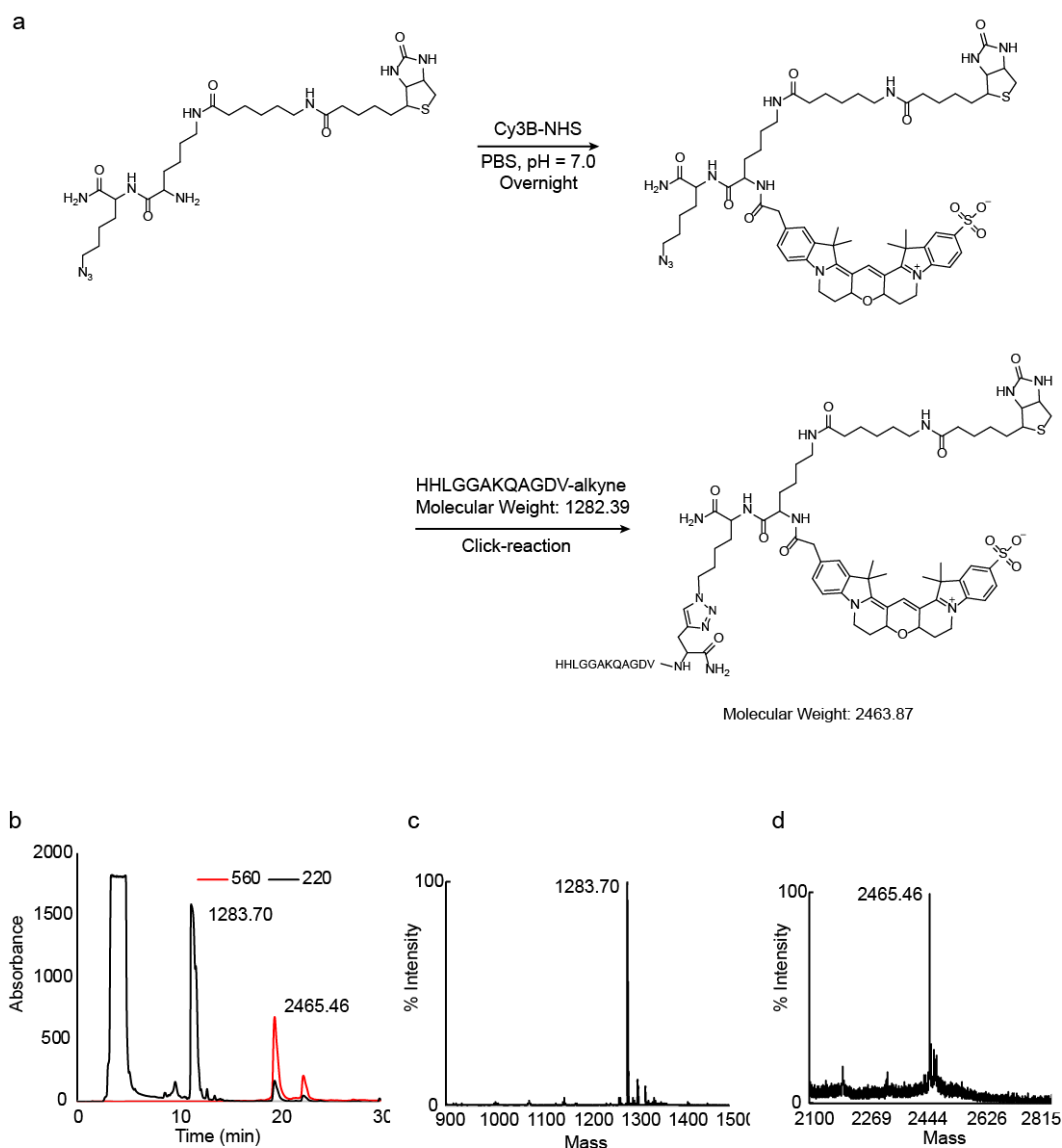
Figure A3.2 Synthesis and characterization of the Cy3B-AGD-biotin ligand for ligand mobility experiment. (a) Steps of Cy3B-AGD-biotin synthesis with expected molecular weights. (b) HPLC of final reaction to purify Cy3B-AGD-biotin. The peak with characterized mass of 1283.70 is AGD strand with terminal alkyne group synthesized on peptide synthesizer. The peak with characterized mass of 2465.46 is final product of Cy3B-AGD-biotin. (c) MALDI spectrum for final product of AGD-alkyne. (d) MALDI spectrum for final product of Cy3B-AGD-biotin.
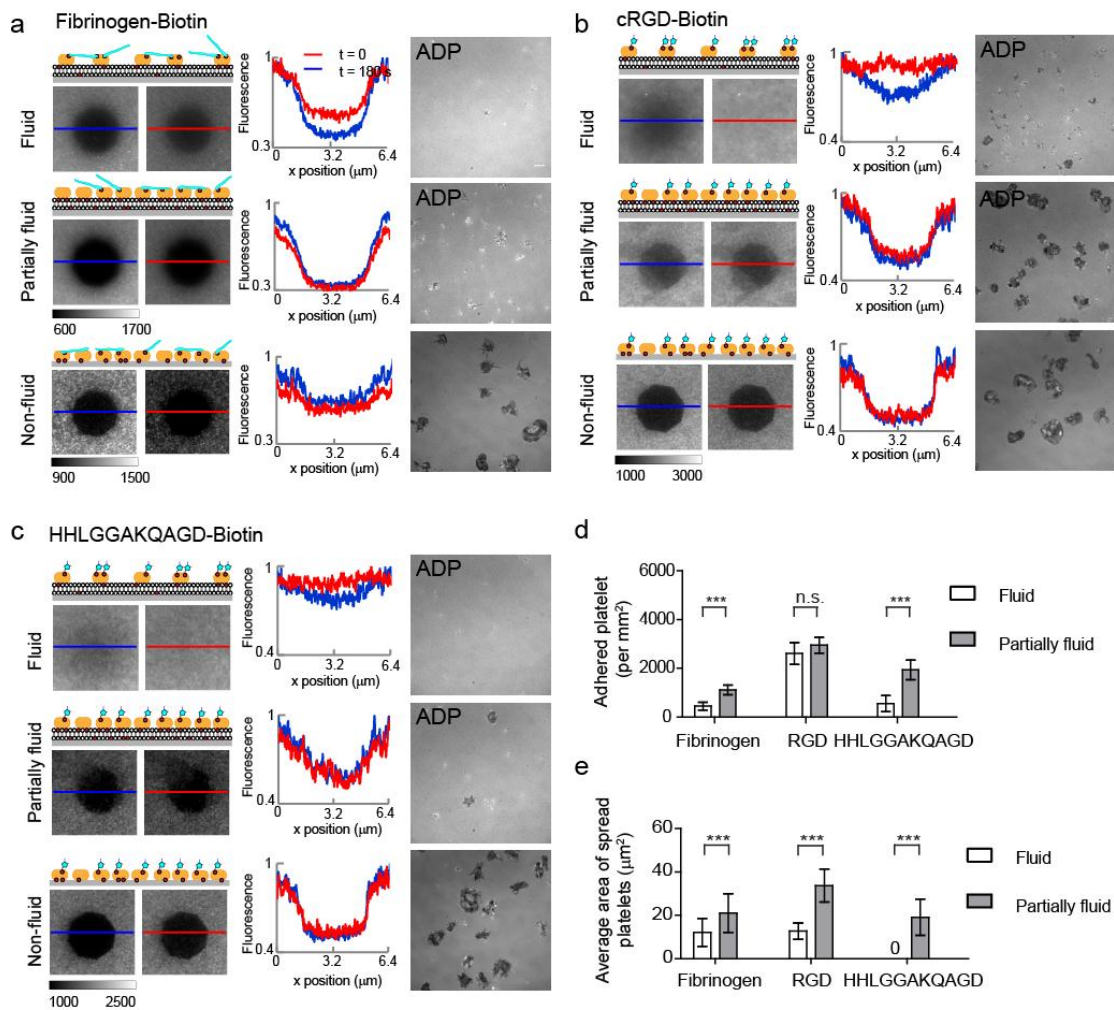
Figure A3.3 Platelet initial activation on SLBs is modulated by lateral ligand fluidity. (a) Schematics of fibrinogen ligands on lipids with different ligand mobilities. FRAP results and representative images of platelet activation with different fibrinogen fluidities are shown on the right. Scale bar: 10 μm. (b) Schematics of cRGD ligands on lipids with different ligand mobilities. FRAP results and representative images of platelet activation are shown on the right. Scale bar: 10 μm. (c) Schematics of AGD ligands on lipids with different ligand mobilities. FRAP results and representative images of platelet activation are shown on the right. Scale bar: 10 μm. (d) Quantitative analysis of platelet adhesion density on SLBs with different ligand lateral fluidities and different ligand types. (e) Quantitative analysis of platelet spreading areas on surfaces with different ligand lateral fluidities and different ligands. (***: p < 0.001; n.s.: not significant; n=10 frames for the adhesion and n=50 cells for the spreading).
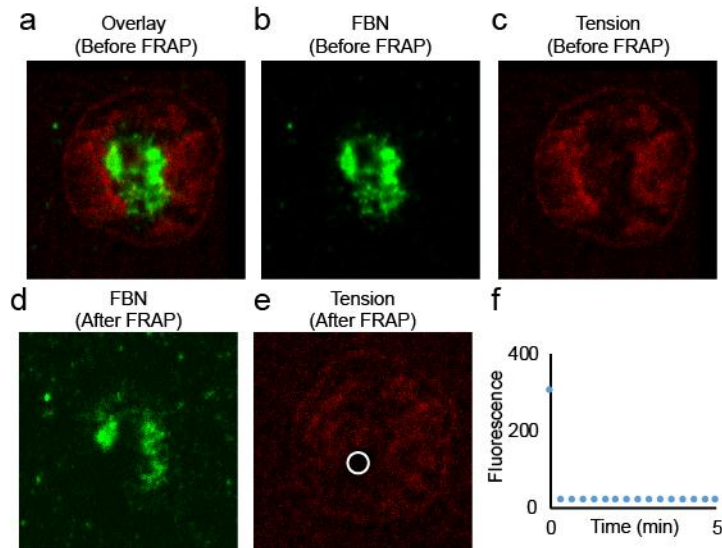
Figure A3.4 FRAP experiment to quantify the fluidity of platelet membrane-bound fibrinogen. (a) Overlay of tension signal (red) and alexa-488 labeled fibrinogen signal (green). Images were taken before the photobleaching of the membrane-bound fibrinogen. (b) and (c) show images of fibrinogen channel and tension channel before photobleaching, respectively. (d) and (e) show the images of fibrinogen channel and tension channel after photobleaching, respectively. White circle highlights the photobleached region. (f) Quantitative analysis of the fluorescence intensity in the photobleached area in a 5-min recovery period. The 0-min data point represents the fluorescence intensity before photobleaching.
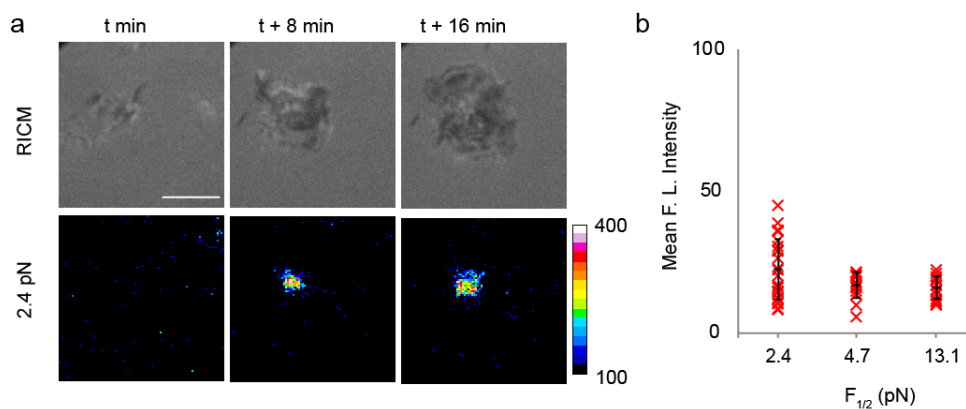
Figure A3.5 Platelet tension signal on AGD tension sensors. (a) Representative time lapse RICM and force images as the platelets spread on the AGD-tension probe with $F_{1/2}$=2.4 pN. Platelet did not generate much tension signal. The weak tension signal was only visible after the cell fully spread out. (b) The mean fluorescence intensity of the unfolded probes did not change much as the force threshold increases. Scale bar: 5 μm.
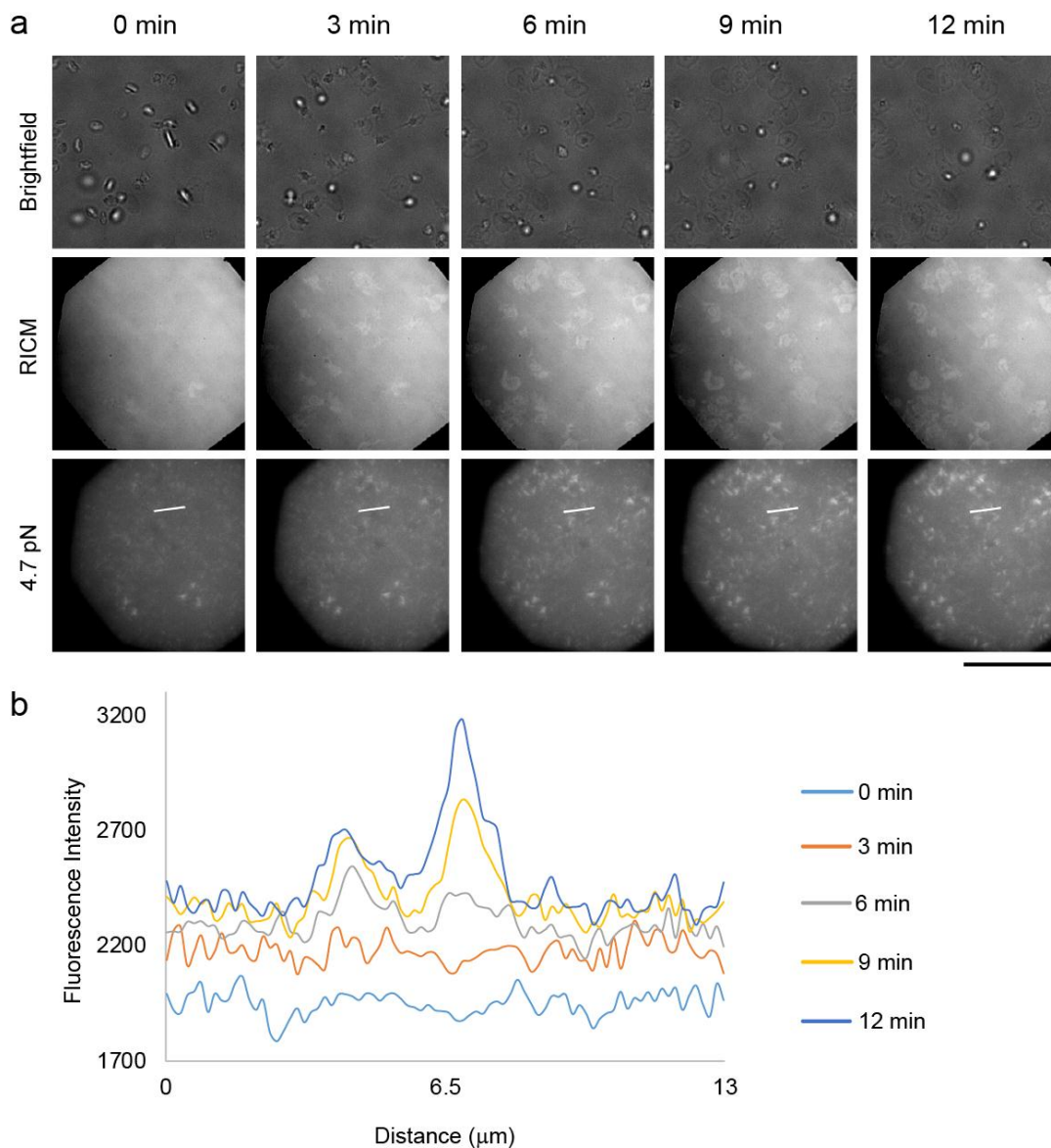
Figure A3.6 Platelet tension measured by fibrinogen tension probes. (a) Representative brightfield, RICM, and tension signal with 4.7 pN $F_{1/2}$ timelapse images at the indicated time points showing the initial cell spreading and adhesion. (b) Linescan analysis of the region highlighted with white line in (a) shows the dynamic growth of tension. Scale bar: 50 μm. Signal from the fibrinogen tension probes presents a much lower signal-to-noise ratio in RICM and tension channels, compared to the signal acquired with cRGD DNA-based tension probes.
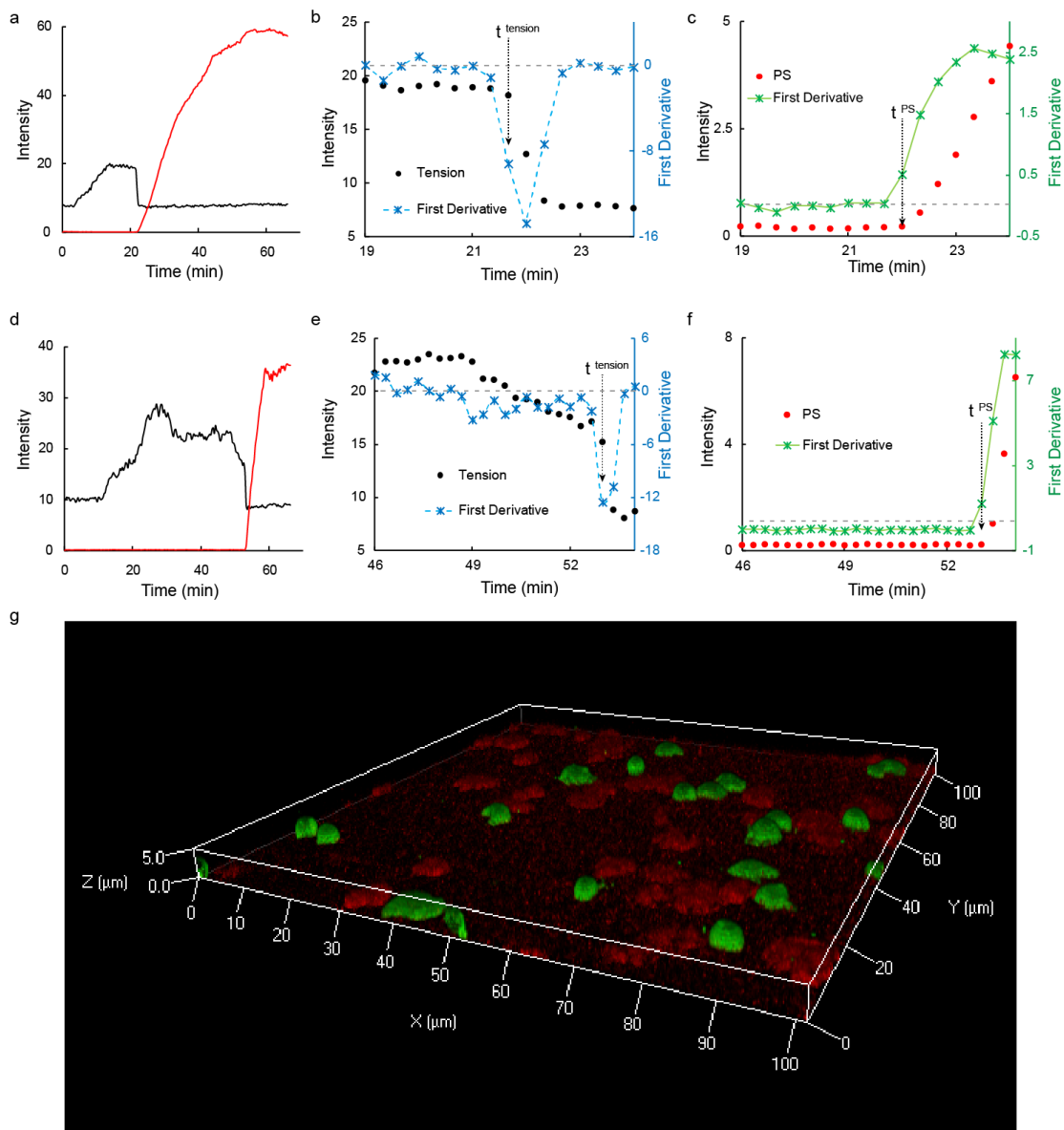
Figure A3.7 Data analysis of Δt, defined as the time difference between the time point of cessation of tension and PS exposure. (a) to (c) and (d) to (f) are data analysis examples of two individual platelets. (a) and (d) Integrated tension signal (black) and PS signal (red) as platelets activate, adhere and spread. (b) and (e) Tension signal analysis at the cessation point. First derivative was also calculated to determine the time point of tension cessation ($t^{tension}$). (c) and (f) PS signal analysis at the tension cessation point. First derivative was also calculated to determine the time point of PS exposure (t^{PS}). (g) 3D rendering of confocal fluorescence image of platelets in two populations. Platelets adhering and spreading on the sensor substrate generate strong tension signals (red). Platelets with PS exposure are rounded up (green).

Chapter 4   DNA origami-based tension probes

4.1   Introduction

Mechanical cues modulate cell functions that range from cell adhesion and migration to proliferation and cancer metastasis.[1-4] Integrin receptors at cell surface are the primary mechanotransducers that transmit forces from the cellular cytoskeleton to the extracellular matrix (ECM) and vice versa. Given the interdisciplinary nature of integrin-mediated mechanotransduction process, different methods to measure integrin mechanics and apply forces to integrins have developed. Single molecule force spectroscopies, including atomic force spectroscopy, magnetic tweezers and optical tweezers, are mainly used to probe the interactions between membrane receptors and their ligands in a serial manner.[5, 6] These single molecule techniques do not recapitulate the biology because membrane receptors function within clusters rather than operating as isolated molecules. For example, integrins assemble into focal adhesions (FAs) containing hundreds of different structural and signaling proteins that physically bridge the ECM to the cytoskeleton. Traction force microscopy (TFM) addresses some of these limitations by measuring the deformation of polymer substrates under cellular forces. Thus, TFM reports the traction stresses ($nN/\mu m^2$) at micron spatial resolution and nN sensitivity. This is sufficient to characterize the forces generated by mature FAs (~micron length scale) but cannot resolve the forces by nascent adhesions or focal complexes that precede the formation of mature FAs.

Recently, our lab developed molecular tension probes to image the piconewton (pN) forces transmitted by individual membrane receptors, such as integrin receptors, T-cell receptors as well as cadherins.[7] Tension probes are comprised of a flexible "molecular spring" with a well-characterized force-extension relationship and flanked by a pair of chromophores acting as a spectral ruler through an energy transfer mechanism. Polyethylene glycols (PEGs), peptides, oligonucleotides and protein domains have been integrated into tension probes as the molecular spring to study cellular forces.[8-12] Different classes of molecular springs offer a range of force-extension relationships, thus providing a toolset for studying various receptors engaged in mechanotransduction processes. For example, PEG-based probes are fully extended upon

experiencing ~ 13 pN tension, and the spider silk protein based elastic peptide probes are sensitive to forces up to ~7 pN.[9, 13] In contrast, DNA-hairpin based probes are highly desirable because their response thresholds can be tuned from 2 to 20 pN by simply increasing the GC content and the length of the stem region.[10, 11, 14] Existing molecular tension probes have in common that they cannot be tuned to respond to forces that exceed ~20 pN. However, integrin receptors have been shown to apply forces greater than 40 pN.[11, 12, 15] Therefore, a calibrated molecular tension sensor is urgently needed to extend the current range of forces detected by molecular tension probes in order to better characterize receptor forces in living cells.

To address this need, we hypothesized that a nanostructure linking multiple molecular springs in a parallel fashion will increase the amount of forces required to generate a signal in a tunable manner. To realize such a design, we generated a nanoscale tension sensor that integrates multiple DNA hairpins using DNA origami approaches. Many complex DNA nanostructures have been created using DNA origami including 2D and 3D microtubes, boxes, tetrahedra and even devices and functional machines.[16-21] Furthermore, DNA origami assembly allows the integration of multivalent ligands in defined geometries.[22-29] Herein, we demonstrate the first example of a calibrated DNA origami tension sensor, and apply this probe to mapping the forces generated by activated platelets. This new class of nanoscale tension probes is significant because it opens the door toward more complex and sophisticated reporters of molecular mechanics with extended force dynamic range. This approach also offers a powerful tool to investigate the roles of multivalency in mechanotransduction.

4.2   Results

4.2.1 *Fabrication of DNA origami based force sensors.*

DNA origami tension sensors include three basic components: a ligand presenting domain, an origami body and a force transducer unit consisting of multiple DNA hairpin molecular tension probes arrayed in parallel (Fig. 4.1a). The body component of the nanoscale

tension sensor is assembled utilizing the DNA origami technique. The origami structure is comprised of a 425 nucleotide single-stranded DNA scaffold folded by ~15 mer staple strands through hybridization. The resulting structure is a six-helix origami packed on a honeycomb lattice (Fig. 4.1a, see Methods section for design details). The six-helix bundle is ~30 nm long and ~6 nm in diameter and presents multiple ligands at one end and the force transducer unit at the other end in a highly defined geometry (Figure 4.1a, b and c). The termini of the strands displaying the force transducing unit are modified with thiol groups, thus anchoring the construct onto a AuNP-coated substrate. The force transducing unit includes DNA hairpins tagged with a fluorophore-quencher pair at the two ends of the hairpin stem. The Cy3B fluorophore, which is proximal to the quencher (BHQ1) and ~11 nm apart from AuNP surface, is dual-quenched by both the molecular quencher through Förster resonance energy transfer (FRET) mechanism and the AuNP through nanometal surface energy transfer (NSET). This dual-quenching mechanism significantly enhances the signal-to-noise ratio by decreasing the background signal.[14] When integrin receptors engage with the adhesive peptides and apply forces exceeding the unfolding force (F_{unfold}) of this origami tension sensor, the hairpins unfold in a cooperative manner. Opening of the DNA hairpin probes separates the fluorophores away from their quenchers and AuNPs generating increased fluorescent signal. As a proof of concept, four constructs were generated: one-hairpin and one-peptide (1H1P), one-hairpin and two-peptide (1H2P), two-hairpin and two-peptide (2H2P) and three-hairpin and two-peptide (3H2P) (Figure 4.1b and 4.1c, see Methods section for design details). Increased molecular weights of 1H2P, 2H2P and 3H2P clearly indicated the successful incorporation of multiple hairpins within the DNA origami scaffold (Figure 4.1d).
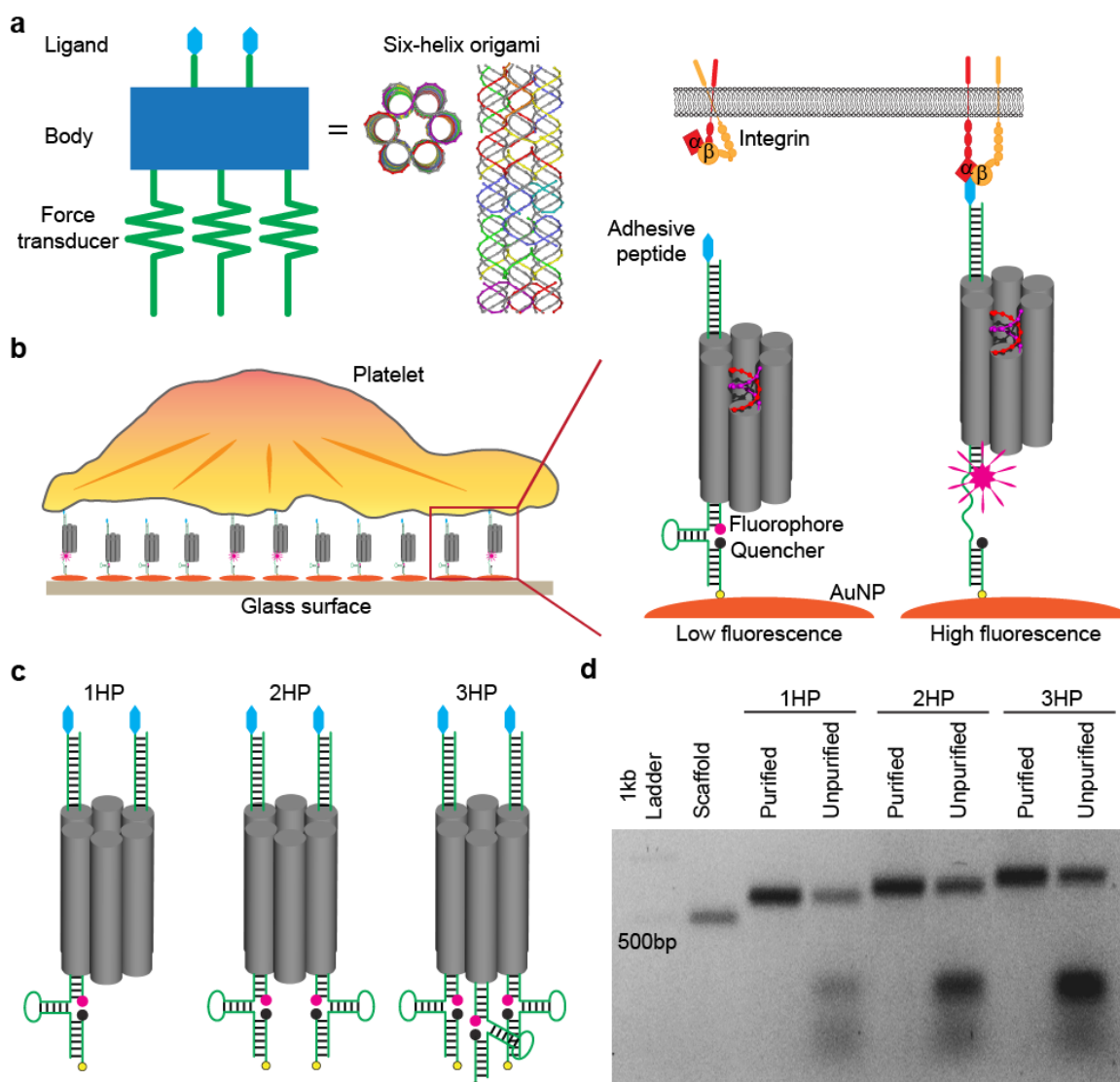
Figure 4.1 Overall design and characterization of DNA origami-based tension probes. (a) Schematic showing three parts of a DNA origami tension probe: ligand presenting domain, origami body and a force transducer unit. The body is comprised of a six-helix DNA origami (top and side view), in which six parallel double-helices are packed on a honeycomb lattice. (b) Illustration of a platelet spreading on an origami based force sensor substrate. The zoomed-in scheme shows the details of the construct and mechanism of response. An adhesive peptide (cRGDfk)-modified DNA strand is attached to one side of the six-helix bundle and DNA hairpin molecular tension probes are hybridized on the other side. The origami constructs are assembled onto AuNPs coated glass surfaces utilizing thiol-Au binding. Upon receptor engagement, the hairpin unfolds under sufficient tension, separating the fluorophore from the quencher and AuNP, which causes dequenching of the dye. (c) Schematic of origami tension probes with two peptides on one side and one-, two- and three-hairpins (1H2P, 2H2P and 3H2P, respectively) on the other side. (d) Agarose gel electrophoresis of purified and unpurified 1H2P, 2H2P and 3H2P. The scaffold band contains single stranded DNA of 425 nucleotides.
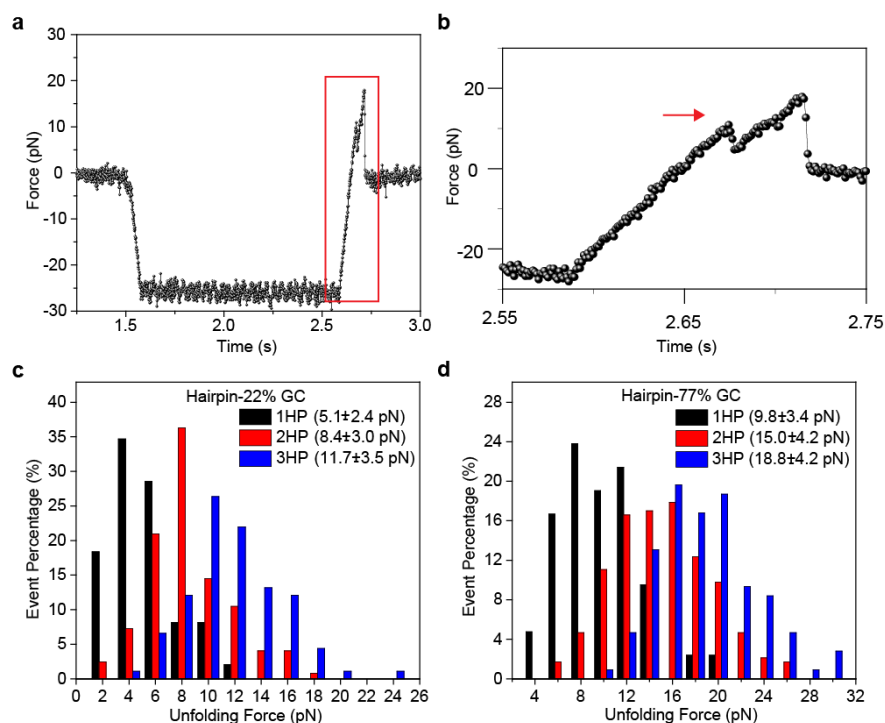
Figure 4.2 DNA origami-based tension probe calibration by biomembrane force probe (BFP) single molecule force spectroscopy. (a) Representative trace of a single molecule unfolding event showing unfolding of DNA origami structure with one hairpin of 77% GC. (b) Zoom-in of the trace in (a) showing the unfolding of the hairpin. The red arrow indicates the opening of the hairpin around 9.8 pN. (c) Histogram of unfolding events for 1HP-22% GC (black, event size = 50), 2HP-22% GC (red, event size = 100) and 3HP-22% GC (blue, event size = 90). The legend shows the corresponding mean F_{unfold} of each probe. (d) Histogram of unfolding events for 1HP-77% GC (black, event size = 42), 2HP-77% GC (red, event size = 230) and 3HP-77% GC (blue, event size = 98). The legend shows the corresponding mean F_{unfold} for each probe.

4.2.2 Calibration of DNA origami tension sensors with BFP

To measure the force thresholds of DNA origami tension sensors, we calibrated two sets of DNA origami tension sensors consisting of hairpins with 22% GC-content stem and 77% GC-content stem. The calibration was performed using the BFP technique, which is a single molecule force spectroscopy technique based on optical monitoring of the displacement of the interface between a microparticle and a red blood cell.[30] The unfolding of the DNA origami tension sensor was identified by a dip in force level in force extension curve (Figure 4.2 a and b).

With a loading rate of 500 pN/s, we found that the experimental F_{unfold} (the mean force required to unfold the DNA origami tension sensors) of the DNA origami-based tension probes

with one, two and three 22% GC hairpins were 5.1 ±2.4 pN (n = 50 unfolding events), 8.4 ±3.0

pN (n = 100 unfolding events), and 11.7 ±3.5 pN (n = 42 unfolding events), respectively (Figure

4.2c). For the DNA origami-based tension probes with one, two and three 77% GC hairpins, the

thresholds were 9.8 ±3.4 pN (n = 100 unfolding events), 15.0 ±4.2 pN (n = 230 unfolding events)

and 18.8 ±4.2 pN (n = 98 unfolding events), respectively (Figure 4.2d). The 1H-22% GC origami

probe displayed a F_{unfold} of 5.1 ±2.4 pN, which generally agrees with the $F_{1/2}$ (the force at which

50% of hairpins unfold) of a single hairpin (4.7 ± 1.7 pN), suggesting that incorporation of the

bulky origami structure does not significantly alter the mechanical properties of hairpin molecular

probes. This agreement of F_{unfold} and $F_{1/2}$ also suggests that it is the single 22% GC hairpin in the

origami sensor that unfolds rather than other elements within the origami scaffold. Although we

observed an increase in F_{unfold} as the number of hairpins per construct was increased, the F_{unflod}

increase was not linear, particularly for 77% GC origami probes. The force thresholds of DNA

origami tension probes with 77% GC content increased by 5.2 pN from one hairpin to two

hairpins and by 3.8 pN from two hairpins to three hairpins, thus deviating from the 9.8 pN per

hairpin relationship. This result led us to suspect that for DNA origami tension probe with

multiple hairpins the DNA origami scaffold must play a role in the distribution of mechanical

forces to the molecular springs. It is also possible that the orientation of the pulling force relative

to the DNA structure alters the cooperativity of the multi-hairpin design.

4.2.3 Computational modeling of tension thresholds

We expected that the DNA origami tension probe consisting of multiple hairpins in

parallel would have a force threshold equal to the sum of the force thresholds of the individual

hairpins. Instead, we observed sub-linear addition of the tension thresholds. We hypothesized that

three effects were causing this unexpected result: 1) statistical variations in force thresholds of the

individual hairpins, 2) unequal distribution of load among multiple hairpins, and 3) non-

uniformity of force pulling angle relative to the surface normal. To investigate these hypotheses *in silico*, we utilized a series of computational models.

4.2.3.1 Even-load Monte Carlo simulation

To better understand the effect of statistical fluctuations of the rupture force of individual force probes, we created a Monte Carlo simulation capable of approximating the average unfolding force of parallel hairpins with a varying number of hairpins (m). First, each hairpin is assigned a force threshold generated from the BFP histogram of the single hairpin construct. Second, the force required to unfold all hairpin is calculated. This is done by calculating the total force required to open the weakest hairpin, then redistributing the force amongst the remaining hairpins and repeating until all of the hairpins are open. Finally, this process is repeated enough times to obtain an ensemble measurement of the average unfolding force, F_{unfold}. As shown in 4.3a, F_{unfold} increases linearly with m for the 9.8 pN hairpin. However, the slope of the line is 6.3 pN/hairpin, which is below the expected slope of 9.8 pN/hairpin. This difference is likely a result of load redistribution amongst the remaining closed hairpin(s) whenever a hairpin opens. This means that if one hairpin has a lower than average force threshold, it will break earlier and redistribute its load. While these results do help to explain our experimental results, they do not fully capture the very small difference observed between the two and three hairpin probes. They also predict a higher increase in F_{unfold} than is observed experimentally.

4.2.3.2 Uneven-load Monte Carly simulation

To test whether uneven distribution of load between hairpins in the parallel force probes might affect the observed rupture force, we modified the above Monte Carlo simulation to include tension imbalances defined by partition coefficients P_i (where i=1, 2,…, m, and $\sum_{i=1}^{m} P_i = 1$). For the two-hairpin tension probe, both partition coefficients can be characterized by P_{min}, the minimum of P_1 and P_2. The relationship between F_{unfold} and P_{min}, as shown in 4.3b, indicates that

the unfold force of a parallel force probe decreases as the load becomes less evenly balanced between the two hairpins. We assume that this is also true for parallel force probes with more than two hairpins.

4.2.3.3 Finite element model simulation

In order to estimate the effect of force orientation on unfolding force of parallel hairpins probes, we generated a 3D model of the six helix bundle and simulated tensile forces in different directions characterized by the angles θ (angle from the z-axis, with the six-helix bundle being oriented along the z-axis) and ϕ (rotation around the z-axis) as shown in 4.3c. For the three hairpin case, all three partition coefficients varied widely with force angle as shown in 4.3d. interestingly, the vast majority of force angles only engage one or two of the hairpins as shown in 4.3e. Only a small subset of angles engage all three hairpins. These results, taken together with the results of the uneven-load Monte Carlo simulation, indicate that the rupture force is highly dependent on force angle.
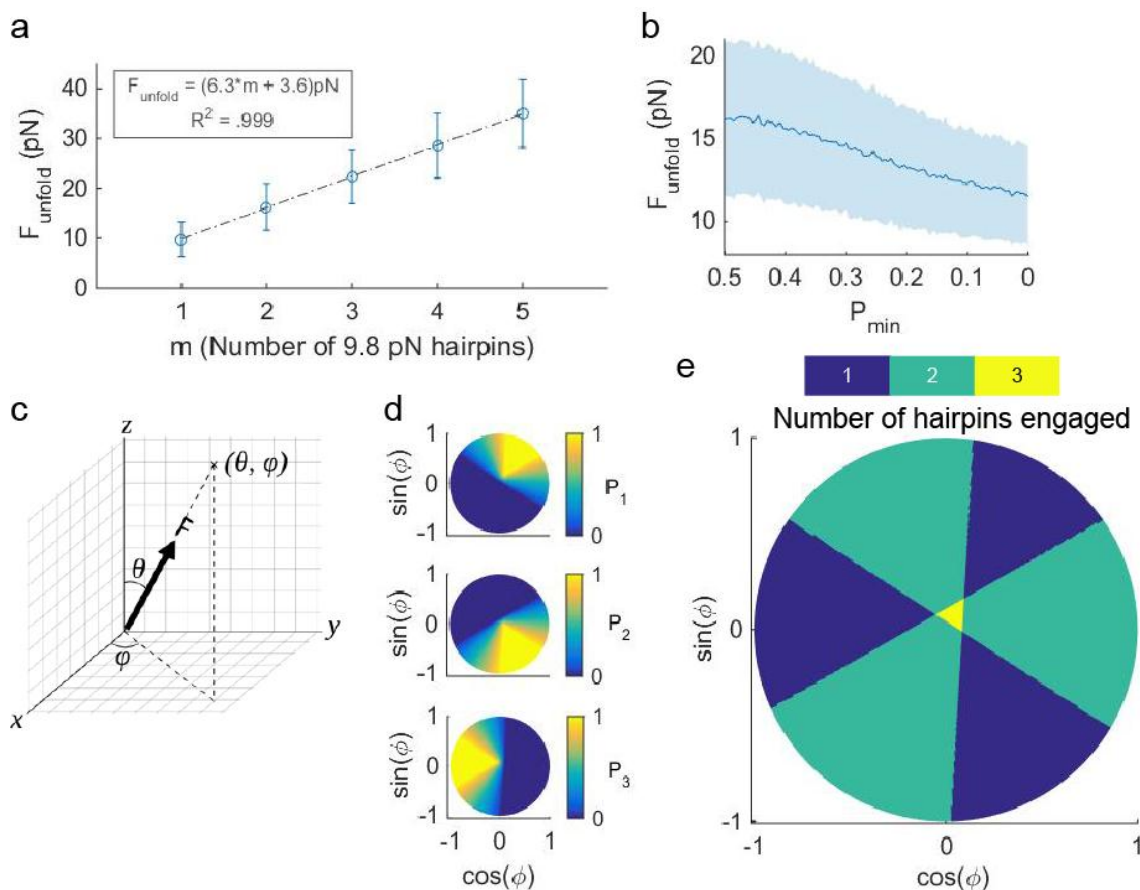
Figure 4.3 Simulation results elucidate potential causes of sub-linear addition of hairpin tension thresholds. (a) Even-load monte carlo simulations demonstrate a threshold increase of 6.3 pN per additional hairpin. Error bars represent standard deviation of simulated opening tension from N=1,000 iterations. (b) Uneven-load monte carlo simulations suggest that the force threshold decreases when tension is transmitted unevenly to hairpins in parallel. Shaded region represents standard deviation as in a. (c) Coordinate system depicting our representation of force angle. Finite element simulations indicate that changes in the force angle lead to changes in (d) the proportion of tension (P_i, i= 1, 2, 3) experienced by the three hairpins, as well as (e) The number of hairpins undergoing tension.
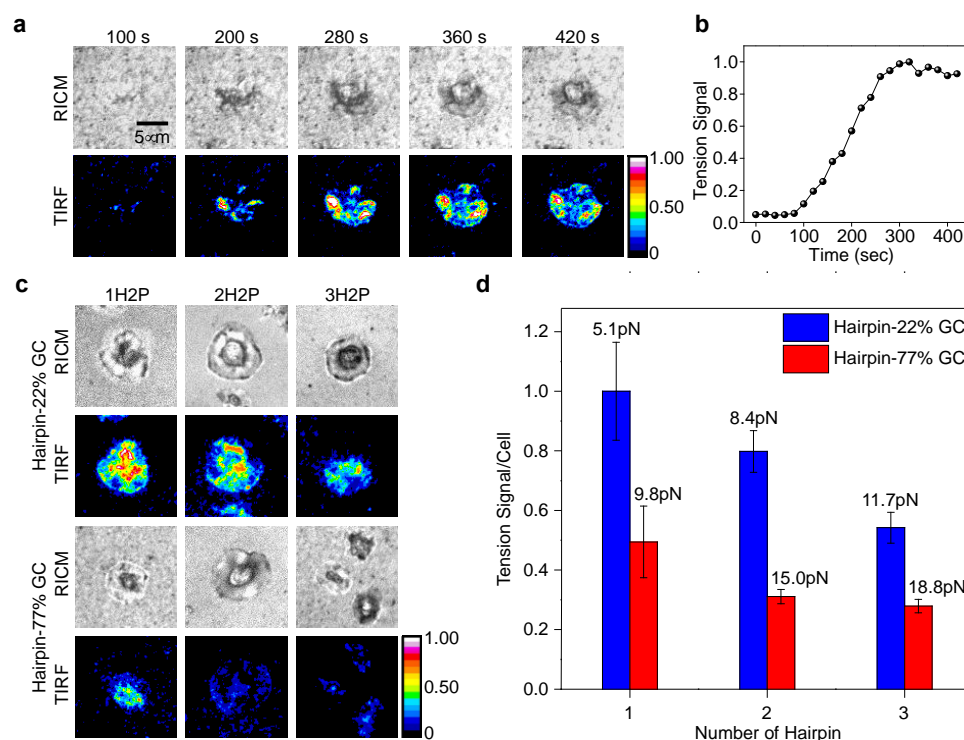
Figure 4.4 Platelet mechanics measured by DNA origami tension sensors. (a) Representative time-lapse images of platelet spreading in RICM channel and tension signal in TIRF channel on the substrate coated with 1HP-22% GC origami tension sensors. Scale bar: 5 μm. (b) Representative plot of tension development of the platelet shown in (a). (c) Representative platelet adhesion and corresponding tension signal of platelets activated on surface coated with DNA origami tension probes with one, two and three hairpins of 22% GC content and 77% GC content. (d) Comparison of the tension signal from platelets activated on DNA origami tension probes with one, two and three hairpins of 22% GC content and 77% GC content. Mean tension signal for 1H2P with 22% GC was normalized to 1 and all the others were calculated relative to it. Each bar represents averaged signal from more than 20 individual cells. BFP calibrated mean F_{unfold} are listed corresponding to each bar.

4.2.4 Application of origami tension probes in living cell system.

The calibration and simulations showed that the DNA origami scaffold can place hairpins in parallel, thus extending the force threshold of a 9.8 pN probe to 18.8 pN. This dynamic range is suitable to measure forces exerted by platelets and T-cells.[14, 31, 32] To demonstrate the capability of measuring cellular forces using this origami tension sensor, we first tested our probes with platelets using cRGDfK (which binds to the $\alpha_{IIb}\beta_3$ integrin) as the ligand. Platelets were plated onto the substrate coated with 1H2P-22% GC (5.1 pN) origami tension sensors. With ADP

activation, platelets quickly attached to the substrate within 3 min and unfolded the 5.1 pN origami tension probes resulting in increased fluorescence intensity under the cell body (Figure 4.4a). Tension signal continued to increase as the platelet further spread out. Platelets fully spread within 5 min and the tension signal reached a plateau at this timepoint (Figure 4.4b). The tension signal located at the lamellipodial edge and under the cell body, showing a similar spatial distribution as was discussed in Chapter 3 using DNA-based molecular probes. These experiments also revealed similar tension dynamics, where the tension signal increases rapidly as the platelet spread and reached a steady state as the platelet fully expanded. This experiment demonstrates that the DNA origami sensor is capable of measuring cellular forces in living cells.

We next investigated the mechanical response of platelets when challenged with origami sensors with higher F_{unfold}. Platelets were seeded onto the surfaces decorated with 1H2P, 2H2P and 3H2P of 22% GC and 77% GC DNA origami tension probes. Representative cell spreading and tension response are shown in Figure 4.4c. Quantitative analysis of these experiments are displayed in Figure 4.4d. Platelets were able to adhere and spread onto all substrates and generated tension signal regardless of F_{unfold}. The mean fluorescent tension signal per cell decreased with increasing F_{unfold}. This general trend confirms that origami sensors with different numbers of hairpins generate different force dynamic ranges. These data also indicate that within a single platelet, forces applied by integrins are highly heterogeneous ranging from 5 to 19 pN. We also noticed that the 1H2P-77% GC probe reported a much lower tension signal compared to the 2H2P-22% GC probe, despite these two DNA origami sensors having similar calibrated tension thresholds. This result may be explained by the complexity inherent to this multi-hairpin design, as discussed in the simulation section above. When the DNA origami sensors display multiple sensors, the unfolding possibility is highly affected by the direction of pulling forces and uneven distribution of these mechanical loading, leading to decreased F_{unfold} and higher tension signal of 2H2P-22 GC%.

We also demonstrated the capability of using the origami tension probes to study the effects of ligand multivalency. Multivalent ligands are critical for cell-membrane receptor recognition, as cells often encounter naturally occurring multivalent arrays of binding partners.[33, 34] In our experiments, one-hairpin origami probe with one binding peptide (1H1P) and two binding peptides (1H2P) were designed (Figure 4.5a). Sensor platforms were prepared with 1H1P and 1H2P of the same concentration and showed similar background intensity, indicating that the two substrates presented the origami tension probes at similar densities. ADP activated-platelets were added to these two substrates and cell adhesion density and tension signal were measured after 20 min of incubation. The 1H2P design supported more platelet adhesion with greater tension signal (Figure 4.5b). This result suggests that the 1H2P origami sensors increase the effective ligand activity. By providing two binding sites per DNA origami probes, the two-peptide origami tension probes increase the overall ligand density and the possibility of each tension probe to interact with platelet integrins. Because of the proximity between the two peptide duplex strands (maximum 6 nm), it is unlikely that two integrins can engage the two ligands of the same construct, as the integrin size is around 10 nm in diameter.[35] The tension signal is due to single integrin receptor forces.

4.3   Discussion

We present the first design of a DNA origami tension sensor and demonstrate the capability of applying this probe to measure cellular forces using platelets as a model system. Origami sensors with greater F_{unfold} generate lower levels of tension signal, thus showing that the majority of platelet integrins apply forces less than 15 pN, but some integrins can exert forces to 19 pN. This is consistent with our results obtained with DNA-based molecular tension probes (Chapter 3). Platelet tension maps also revealed that platelet tension is highly heterogeneous at the single receptor level over the whole cell. This origami tension sensor can also be used to study the effect of ligand multivalency by incorporation of multiple peptides into the nanostructure. In principles,

the origami tension sensor can be further extended to study hetero-multivalency, interactions in which different types of ligand-receptor recognition events occur between the two entities.[36] For example, DNA origami tension sensors can be applied to study how the synergy site on fibronectin, located about 32 Å from the RGD sequence, influences integrin mechanical force transmission.
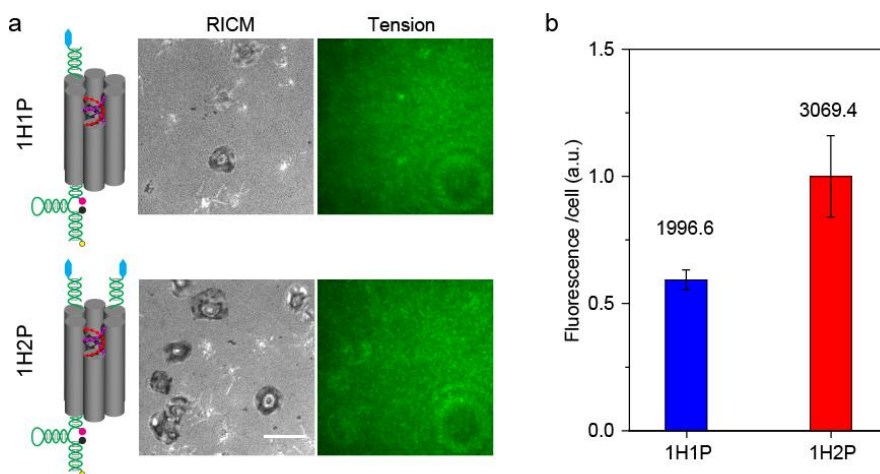
Figure 4.5 Demonstration of the multivalency of origami tension sensors. (a) Schematics of the one-peptide and two-peptide designs with representative RICM images showing cell adhesion density. Scale bar: 10 μm. (b) Quantitative analysis of the cell density (cells/mm^2, shown on top of each bar) and normalized tension signal. 1H2P origami sensor design supports higher cell adhesion density and generates greater fluorescent tension signal.

4.4   Materials and methods

4.4.1 Materials

Amine modified Silica beads (4.86 mm, SA05N) were purchased from Bangslabs. Lipoic acid (T5625) EDC (E6383) and NHS (130672) were purchased from SIGMA-ALDRICH. (3-Aminopropyl) trimethoxysilane (97%, APTMS), triethylammonium acetate (TEAA), and the fluorescent dye Cy3B-NHS ester were purchased from GE healthcare Bio-Science (Pittsburgh, PA). Number two glass coverslips, ascorbic acid (>99.0%), and 96-well plates were purchased from Fisher Chemical & Scientific (Pittsburgh, PA). DMF (>99.5%), DMSO (99.5%) and sodium

bicarbonate (99.0%) were purchased from EMD chemicals (Philadelphia, PA). P2 gel size

exclusion beads were acquired from Biorad (Hercules, CA). Lipoic Acid-PEG-NHS (MW 3400)

and mPEG-NHS (MW 2000) were purchased from Nanocs (New york, NY). DNA sequences

used in this project are listed in Table 4.1 and Figure 4.6.

Table 4.1 DNA sequences in Chapter 4.

2-22%GC	GTGAAATACCGCACAGATGCGTTTGTATAAATGTTTTTTTCATTT ATACTTTATAGCACGAGGGTCTCACCAGTCACACGACCAG
6-22%GC	GTGAAATACCGCACAGATGCGTTTGTATAAATGTTTTTTTCATTT ATACTTTATAGCACGAGGGTCCGGCCTTGCTGGTAATATC
11-22%GC	GTGAAATACCGCACAGATGCGTTTGTATAAATGTTTTTTTCATTT ATACTTTATAGCACGAGGGTCCGGTACGCCAGAATCCTGA
2-77%GC	GTGAAATACCGCACAGATGCGTTTGTACGCGCGTTTTTTTCGCGC GTACTTTATAGCACGAGGGTCTCACCAGTCACACGACCAG
6-77%GC	GTGAAATACCGCACAGATGCGTTTGTACGCGCGTTTTTTTCGCGC GTACTTTATAGCACGAGGGTCCGGCCTTGCTGGTAATATC
11-77%GC	GTGAAATACCGCACAGATGCGTTTGTACGCGCGTTTTTTTCGCGC GTACTTTATAGCACGAGGGTCCGGTACGCCAGAATCCTGA
1-Dye	GACCCTCGTGCTAT
Q-SH	BHQ1-CGCATCTGTGCGGTATTTCACTTT-SH
10-peptide	/5Hexynyl/TTTCCTTCTCTCTTTAAATTAACCGTTGTAGCAATACTG GAAAAAGAAATAC
15-peptide	/5Hexynyl/TTTCCTTCTCTCTTTGTATAACGTGCTTTCCTCAGTCTG TCCA
10-biotin	/5Biosg/TTTAAATTAACCGTTGTAGCAATACTGGAAAAAGAAATA C
Staple 1	GACCCTCGTGCTAT
Staple 2	ATAGCACCAGGGTCTCACCAGTCACACGACCAG
Staple 3	TAATGGATTATTTACATTGG
Staple 4	TCTGAAATAAAAGGAGGCCGATTAAAGGGATTTTAGAC
Staple 5	CTACATTCAGAGATTCAGAGCGGGAGCTAGTGAGGTTAGTAA
Staple 6	ATAGCACCAGGGTCCGGCCTTGCTGGTAATATC
Staple 7	CAGAACAATAACTTGCCGTGTTTT
Staple 8	TGCAACATCTTTGACCACCGA
Staple 9	TAACATCTTACCGCTCAATCG
Staple 10	AAATTAACCGTTGTAGCAATACTGGAAAAAGAAATAC
Staple 11	ATAGCACCAGGGTCCGGTACGCCAGAATCCTGA
Staple 12	GAATGAGTAGAAGAACTCAA
Staple 13	TATAATCAAACAGGGACATTCTGGCCAATTGACGCCAGCCAT
Staple 14	GTAAAAGGTTAGAAAGAACCCTTC
Staple 15	ACGTGCTTTCCTCAGTCTGTCCA
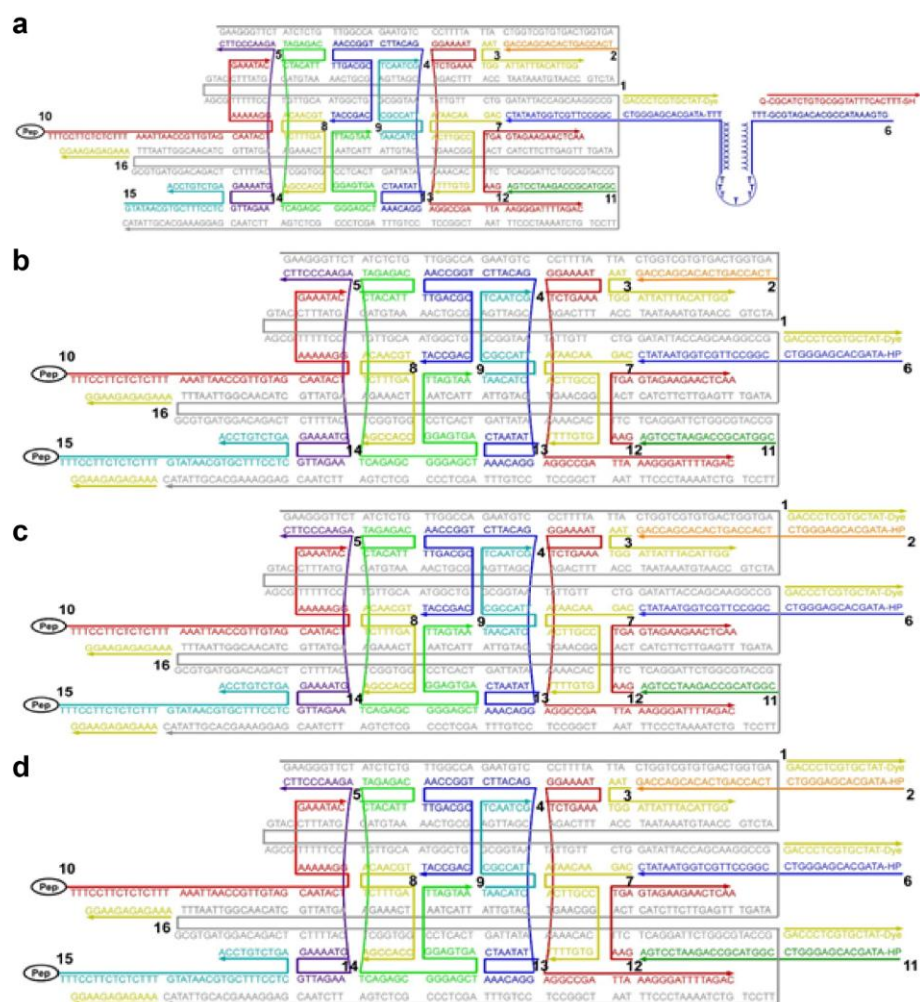
Figure 4.6 Schemes and DNA sequences of six-helix origami bundles with different numbers of peptides and hairpins. (a) 1H1P. (b) 1H2P. (c) 2H2P. (d) 3H2P.

4.4.2 Preparation, purification and characterization of six-helix origami.

Six-helix origami structures were synthesized by mixing the 'staple' strands with a single stranded scaffold (425 nucleotide) in a molar stoichiometric ratio of 5:1 in $1\times$TE-Mg^{2+} buffer (40 mM Tris, 2 mM EDTA, 12 mM MgCl$_2$, pH 8). The final concentration of the scaffold was adjusted to 400 nM. The mixture was then annealed in a thermo cycler from 65 °C to 25 °C over 12 hours. Samples were then subjected to gel electrophoresis (1.5 % agarose) in $0.5\times$TBE-Mg^{2+} buffer (45 mM Tris, 45 mM Boric acid, 1 mM EDTA, 10 mM MgCl$_2$) for purification and

verification. The purified samples were then confirmed with TEM imaging upon staining the samples with 1% uranyl formate for 15 seconds. The peptide modified DNA (10-peptide) was replaced with biotin modified DNA (10-biotin) to prepare origami samples for biomembrane force probe (BFP) calibration experiments.
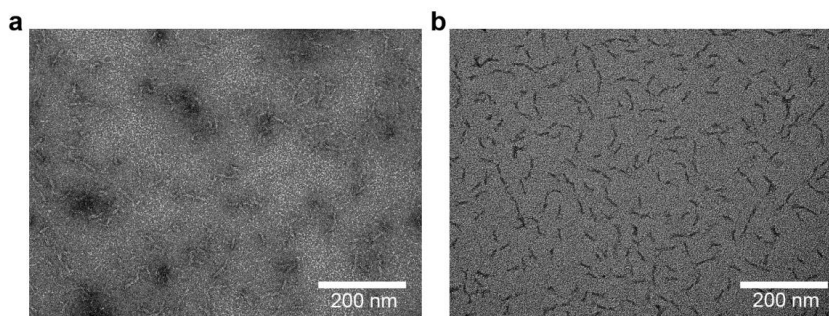
Figure 4.7 Transmission electron microscopy (TEM) images of six-helix origami bundles. (a) Negative stain and (b) positive stain.

4.4.3 Preparation of origami sensor for BFP calibration.

Lipoic acid, EDC and NHS were mixed at molar ratio of 4 mM: 2 mM: 2 mM (100 µL) in phosphate buffer for 15 min (pH 7.0, the activation reaction with EDC and Sulfo-NHS is most efficient at pH 4.5-7.2). Next, 2 mg of silica particles were suspended in 900 µL phosphate buffer (pH 8.0). Then 100 µL of lipoic acid activation solution was added to the 900 µL silica particle solution and rotated for 3h at RT. Lipoic acid modified silica particles were purified by centrifugation. Discard the supernatant and resuspend the silica particles into DI water. Repeat this purification step three times to remove the excess of lipoic acid, EDC and NHS. The silica particles were stored in DI water for subsequent AuNP modification. The AuNP solution (5.4 nM) was added to the lipoic acid particle solution for 15 min and then centrifuged at low speed to remove the unbound Au particles. DNA origami samples were incubated with AuNP modified silica beads overnight at 4 ℃. No purification is needed before BFP calibration.

4.4.4 Origami sensor calibration by BFP.

In the BFP setup, a biotinylated red blood cell (RBC) was first aspirated by a micropipette. A streptavidinylated glass bead was then attached to the apex of the RBC to form an ultra-sensitive force probe. On the opposite side, a bead coated with our DNA force probe was aspirated by a target micropipette. A piezoelectric translator (Physical Instrument, MA) drove the target pipette with sub-nanometer precision via a capacitive sensor feedback control. The beads were assembled in a cell chamber filled with L15 media supplemented with 5 mM HEPES and 1% BSA and observed under an inverted microscope (Nikon TiE, Nikon) through two cameras. One camera (GC1290, Procilica, MA) captured real-time images at 30 frames per second (fps), while the other (GE680, Proscilica, MA) recorded at 1,600 fps as the region of interest was confined to the contact interface between the RBC and the bead. A customized LabView (National Instrument, TX) program analyzed the image and tracked in real-time the position of the bead with a 3-nm displacement precision.[37] The BFP spring constant was set to ~0.3 pN/nm, and it was determined from the suction pressure inside the probe pipette that held the RBC, the radius of the probe pipette, the diameter of the spherical portion of the RBC outside of the pipette, and the contact area between the RBC and the probe bead.[37, 38]

Briefly, in a measurement cycle, a DNA-coated 5-micron silica bead was brought into contact with the probe bead with a 20 pN impingement force for 0.1 s to allow bond formation. The target pipette was then retracted at 500 pN/s until it reached a 20 pN force level before dropping the force level to ~0 pN by bringing the two beads into close proximity again. The biotin-streptavidin bond was ruptured after 1 s, and the target bead was returned to the original position to start the next cycle. To ensure that most adhesion events were due to single bonds, adhesion frequency (number of adhesions divided by total number of contacts) was controlled to be ≤20% by adjusting the coating density of the DNA force probe.[39]

An unfolding event was identified by a dip in force level in the force-ascending phase (Figure 4.2), due to the lengthening of the DNA upon hairpin opening. Similarly, a folding event

was identified by a rise in force level in the force-descending phase. The force at which each unfolding event occurred was recorded and the cumulative histogram was plotted in Figure 4.2 to determine the $F_{1/2}$.

4.4.5 Platelet isolation

Whole blood was drawn from healthy donors into collection tubes with acid citrate dextrose (ACD). Platelet-rich plasma (PRP) was collected after centrifugation under $150 \times g$ for 15 min. Additional ACD was added into PRP (10% of the PRP volume), which was then centrifuged at $900 \times g$ for another 5 min. Platelet-poor plasma was then removed and the platelet pellet was resuspended in Tyrode's buffer containing 0.1% BSA.

4.4.6 Surface Preparation.

No.2 glass coverslips were rinsed and sonicated with nanopure water (18.2 MΩ cm^{-1}) for 30 min, and then sonicated with acetone for 15 min. The cleaned slides were then dried in an oven set at 80 °C for 10 min. Fresh piranha solution (7:3 v/v = H_2SO_4: H_2O_2) was mixed and then used to clean the substrates for 30 min. Afterwards, the substrates were rinsed with copious amount of nanopure water. The substrates were then sonicated in acetone to remove excess water and to further clean the substrate. Subsequently, 2.5% v/v APTMS solution in acetone was added to the slides and incubated for 2 h. The amine-modified coverslips were then rinsed in acetone and water and dried under a stream of N_2. The slides were then annealed for 1 h at 80 °C. The surface was then passivated with 2.5% w/v mPEG-NHS (MW 2000) and 0.5% w/v lipoic acid-PEG (MW 3400) in 200 μl of 0.1 M fresh sodium bicarbonate solution. After overnight incubation at 4 °C, the excess unreacted PEG molecules were rinsed with nanopure water. This strategy affords a glass surface with sufficient lipoic acid groups to irreversibly anchor AuNP at appropriate densities. Finally, coverslips were incubated with 3 nM of unmodified 15 nm AuNP solution for 30 min and then rinsed with nanopure water to remove nonspecifically bound

particles. 45 μl of DNA (~ 120 nM) origami tension probe was added between AuNP functionalized coverslip and clean parafilm and incubated overnight at 4 ℃. Without rinsing the surface, 50 μl passivation strands at 1 μM was added to the AuNP functionalized coverslip for another 6 hr incubation. These modified coverslips were then assembled into cell imaging chambers (Attofluor, Life Technologies) filled with Tyrode's buffer containing 0.1% BSA and immediately used for cell experiments.

4.4.7 AFM imaging.

The density of AuNP on the functionalized glass coverslip was measured by using an atomic force microscope mounted on an anti-vibration stage (MFP-3D, Asylum Research, CA). Silicon AFM tips (MikroMasch) with a force constant (5.4-16 N/m) were used to image the sample in tapping mode at a scan rate of 1 Hz. All images were processed and rendered using IgorPro.
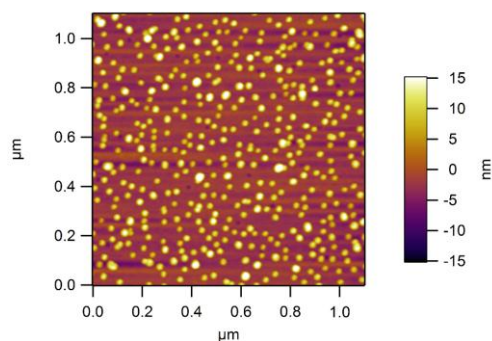
Figure 4.8 Substrate AuNP density characterized by AFM. The density is 357 ± 27 AuNP per μm^2.

4.5 References

1. Burridge, K., Fath, K., Kelly, T., Nuckolls, G. & Turner, C. Focal adhesions: transmembrane junctions between the extracellular matrix and the cytoskeleton. *Annu Rev Cell Biol* **4**, 487-525 (1988).

2. Evans, E.A. & Calderwood, D.A. Forces and bond dynamics in cell adhesion. *Science* **316**, 1148-1153 (2007).

3. Garcia, A.J., Vega, M.D. & Boettiger, D. Modulation of cell proliferation and differentiation through substrate-dependent changes in fibronectin conformation. *Mol Biol Cell* **10**, 785-798 (1999).

4. Levental, K.R. *et al.* Matrix crosslinking forces tumor progression by enhancing integrin signaling. *Cell* **139**, 891-906 (2009).

5. Neuman, K.C. & Nagy, A. Single-molecule force spectroscopy: optical tweezers, magnetic tweezers and atomic force microscopy. *Nat methods* **5**, 491-505 (2008).

6. Helenius, J., Heisenberg, C.P., Gaub, H.E. & Muller, D.J. Single-cell force spectroscopy. *J Cell Sci* **121**, 1785-1791 (2008).

7. Jurchenko, C. & Salaita, K.S. Lighting Up the Force: Investigating Mechanisms of Mechanotransduction Using Fluorescent Tension Probes. *Mol Cell Biol* **35**, 2570-2582 (2015).

8. Liu, Y., Yehl, K., Narui, Y. & Salaita, K. Tension Sensing Nanoparticles for Mechano-Imaging at the Living/Nonliving Interface. *J Am Chem Soc* **135**, 5320-5323 (2013).

9. Morimatsu, M., Mekhdjian, A.H., Adhikari, A.S. & Dunn, A.R. Molecular Tension Sensors Report Forces Generated by Single Integrin Molecules in Living Cells. *Nano Lett* **13**, 3985-3989 (2013).

10. Blakely, B.L. *et al.* A DNA-based molecular probe for optically reporting cellular traction forces. *Nat methods* **11**, 1229-1232 (2014).

11.   Zhang, Y., Ge, C., Zhu, C. & Salaita, K. DNA-based digital tension probes reveal integrin forces during early cell adhesion. *Nat commun* **5**, 5167 (2014).

12.   Wang, X. & Ha, T. Defining single molecular forces required to activate integrin and notch signaling. *Science* **340**, 991-994 (2013).

13.   Liu, Y., Yehl, K., Narui, Y. & Salaita, K. Tension sensing nanoparticles for mechano-imaging at the living/nonliving interface. *J Am Chem Soc* **135**, 5320-5323 (2013).

14.   Liu, Y. *et al.* DNA-based nanoparticle tension sensors reveal that T-cell receptors transmit defined pN forces to their antigens for enhanced fidelity. *P Natl Acad Sci USA* **113**, 5610-5615 (2016).

15.   Jurchenko, C., Chang, Y., Narui, Y., Zhang, Y. & Salaita, K.S. Integrin-generated forces lead to streptavidin-biotin unbinding in cellular adhesions. *Biophys J* **106**, 1436-1446 (2014).

16.   Rothemund, P.W.K. Folding DNA to create nanoscale shapes and patterns. *Nature* **440**, 297-302 (2006).

17.   Douglas, S.M. *et al.* Self-assembly of DNA into nanoscale three-dimensional shapes (vol 459, pg 414, 2009). *Nature* **459**, 1154-1154 (2009).

18.   Andersen, E.S. *et al.* Self-assembly of a nanoscale DNA box with a controllable lid. *Nature* **459**, 73-76 (2009).

19.   Han, D.R. *et al.* DNA Origami with Complex Curvatures in Three-Dimensional Space. *Science* **332**, 342-346 (2011).

20.   Benson, E. *et al.* DNA rendering of polyhedral meshes at the nanoscale. *Nature* **523**, 441-U139 (2015).

21.   Zhang, F. *et al.* Complex wireframe DNA origami nanostructures with multi-arm junction vertices. *Nat Nanotechnol* **10**, 779-784 (2015).

22.   Dutta, P.K. *et al.* DNA-Directed Artificial Light-Harvesting Antenna. *J Am Chem Soc* **133**, 11985-11993 (2011).

23. Bui, H. *et al.* Programmable Periodicity of Quantum Dot Arrays with DNA Origami Nanotubes. *Nano Lett* **10**, 3367-3372 (2010).

24. Schreiber, R. *et al.* Hierarchical assembly of metal nanoparticles, quantum dots and organic dyes using DNA origami scaffolds. *Nat Nanotechnol* **9**, 74-78 (2014).

25. Rinker, S., Ke, Y.G., Liu, Y., Chhabra, R. & Yan, H. Self-assembled DNA nanostructures for distance-dependent multivalent ligand-protein binding. *Nat Nanotechnol* **3**, 418-422 (2008).

26. Pal, S. *et al.* DNA Directed Self-Assembly of Anisotropic Plasmonic Nanostructures. *J Am Chem Soc* **133**, 17606-17609 (2011).

27. Pal, S., Deng, Z.T., Ding, B.Q., Yan, H. & Liu, Y. DNA-Origami-Directed Self-Assembly of Discrete Silver-Nanoparticle Architectures. *Angew Chem Int Edit* **49**, 2700-2704 (2010).

28. Ding, B.Q. *et al.* Gold Nanoparticle Self-Similar Chain Structure Organized by DNA Origami. *J Am Chem Soc* **132**, 3248-3249 (2010).

29. Urban, M.J. *et al.* Plasmonic Toroidal Metamolecules Assembled by DNA Origami. *J Am Chem Soc* **138**, 5495-5498 (2016).

30. Chen, Y. *et al.* Fluorescence Biomembrane Force Probe: Concurrent Quantitation of Receptor-ligand Kinetics and Binding-induced Intracellular Signaling on a Single Cell. *J Vis Exp*, e52975 (2015).

31. Liang, X.M., Han, S.J., Reems, J.A., Gao, D. & Sniadecki, N.J. Platelet retraction force measurements using flexible post force sensors. *Lab Chip* **10**, 991-998 (2010).

32. Schwarz Henriques, S., Sandmann, R., Strate, A. & Koster, S. Force field evolution during human blood platelet activation. *J Cell Sci* **125**, 3914-3920 (2012).

33. Krishnamurthy, V.M., Estroff, L.A. & Whitesides, G.M. Multivalency in Ligand Design, in *Fragment-based Approaches in Drug Discovery* 11-53 (Wiley-VCH Verlag GmbH & Co. KGaA, 2006).

34. Kiessling, L.L., Gestwicki, J.E. & Strong, L.E. Synthetic multivalent ligands in the exploration of cell-surface interactions. *Curr Opin Chem Biol* **4**, 696-703 (2000).

35. Rivas, G.A., Aznarez, J.A., Usobiaga, P., Saiz, J.L. & Gonzalez-Rodriguez, J. Molecular characterization of the human platelet integrin GPIIb/IIIa and its constituent glycoproteins. *Eur Biophys J* **19**, 335-345 (1991).

36. Xu, L. *et al.* Heterobivalent ligands target cell-surface receptor combinations in vivo. *Proc Natl Acad Sci USA* **109**, 21295-21300 (2012).

37. Chen, W., Evans, E.A., McEver, R.P. & Zhu, C. Monitoring receptor-ligand interactions between surfaces by thermal fluctuations. *Biophys J* **94**, 694-701 (2008).

38. Evans, E., Ritchie, K. & Merkel, R. Sensitive Force Technique to Probe Molecular Adhesion and Structural Linkages at Biological Interfaces. *Biophys J* **68**, 2580-2587 (1995).

39. Chesla, S.E., Selvaraj, P. & Zhu, C. Measuring two-dimensional receptor-ligand binding kinetics by micropipette. *Biophys J* **75**, 1553-1572 (1998).

Chapter 5   Summary and future directions

5.1   Summary

This thesis mainly focuses on the development of a new generation of DNA hairpin-based

tension probes for molecular tension fluorescence-based microscopy (MTFM). There is a need

for molecular tension probe displaying pN force resolution and with the capability of examining

multiple individual ligand-receptor interactions simultaneously. The DNA-based MTFM probes

developed as part of this thesis target membrane receptors and act as digital switches upon force

loading. Extensive studies of DNA and RNA mechanics by single molecule force microscopy,

including opening of DNA duplexes in shearing or zipping modes and reversible unfolding of

RNA hairpins, have provided the foundation of this tension sensor design.[1-4] This thesis leverages

the fundamental understanding of oligonucleotide unfolding obtained from single molecule force

spectroscopy toward the investigation of cellular traction forces, particularly the β_3 integrin

mediated adhesion forces in fibroblasts and platelets.

The design of DNA-hairpin based MTFM probes is based on the cooperative nature of DNA

unfolding under mechanical loads. The probability of hairpin unfolding theoretically follows a

sigmoidal curve, and is exponentially dependent on the applied force. The design of a three-strand

system reduces the synthesis cost and endows the sensor with modular components that can be

easily exchanged for the desired target proteins.[5] Chapter 2 details the rationale behind this design

and the application of DNA-based MTFM probes to study integrin $\alpha_v\beta_3$ cellular forces.

DNA tension probes unfold when subject to forces that are below 20 pN, thus defining the

upper limit of response thresholds for these probes. The range of force response thresholds

available to DNA tension probes is well suited for the measurement of platelet-generated and

T-cell generation. Chapter 3 describes the mapping of platelet mechanical contraction and the investigation of the roles of mechanics in platelet activation using the DNA-based MTFM probes. We found that platelets perform a mechanical test of fibrinogen by applying forces to their ligands to determine whether the ligand is surface immobilized or soluble. We also found that platelet forces are highly dynamic and heterogeneous during the process of platelet activation.

One limitation of using DNA hairpins as the mechanical spring element in the MTFM probes is that the range of force thresholds is fairly narrow, spanning from a few pN to 20 pN. Even a hairpin containing a long stem with 100% GC content does not increase the unfolding threshold beyond 20 pN, as the ΔG of unfolding does not increase significantly. Therefore, Chapter 4 aims to design a system with a higher force threshold via parallel connection of multiple single hairpins using an origami helix. The experimental results are unexpected, as we find that the force thresholds do not increase linearly with the number of hairpins per structure. Simulations suggested that parallel hairpins function in a less cooperative manner and the forces required to unfold the DNA origami-based tension probes are strongly affected by the distribution and orientation of the forces. This work provides broader insights into the mechanics of DNA nanostructures.

Another issue associated with the three-strand hairpin design is that this structure is less mechanically stable than the single strand DNA sensor design and reported by Blakely et al.[5] This instability is due to the possible shearing of the DNA duplex handles under prolonged mechanical stresses. However, this instability has also been utilized in force probes designed by Wang et al.[6] Their tension gauge tether is a type of rupturable sensor, which can support cell adhesions if the

forces applied by the receptors are smaller than the threshold of the tethers.

Despite these limitations, many new DNA-based tension probes have been developed for biological applications. The advantage of using DNA as a mechanical spring element in MTFM probes includes their predictable structure, allowing for various modification and ease of design.[7, 8]

5.2   Future directions

5.2.1 Application of current DNA sensors

Besides the advantages mentioned above, DNA-based MTFM probes also allow for multiplexed sensing of the forces applied by different cell surface receptors, as in Chapter 2.2.3 and Chapter 2.2.4. This concept can be further adapted to study the crosstalk between different cell adhesion molecules, such as cadherins and integrins.[9, 10] DNA origami-based tension probes also provide a promising tool to study multivalency, as multiple ligands can be presented within one nanostructure.

5.2.2 Advancing current DNA sensors

The next generation of DNA-MTFM probes will benefit from improving sensor stability, which can be achieved through two different approaches. First, rather than use biotin-streptavidin interactions for immobilization, covalent attachment would afford a stable immobilization system tolerating high cellular forces. For example, the introduction of click-chemistry and the employment of the HaloTag technique are likely candidates that have been previously used for covalently anchoring tension sensors to a substrate.[11, 12] Second, the mechanical stability of the DNA-based MTFM probe itself needs to be increased. To prevent shearing of the duplex handle,

single-stranded DNA tension probes can be used, but such probes are difficult to synthesize.[5] Another compromised design between this three-strand system and single-strand system is shown in Figure 5.1. In this three-strand design (Figure 5.1c), the ligand is integrated at the terminus of the hairpin strand, rather than the fluorophore-labeled strand. Cellular forces can be directly transmited to the hairpin, avoiding shearing of the duplex handles. One can also introduce modified bases to enhance the duplex stability.[13-15] Another possible approach is the use of intercalators to lock the DNA duplex, which has been shown to increase duplex stability.[16, 17]
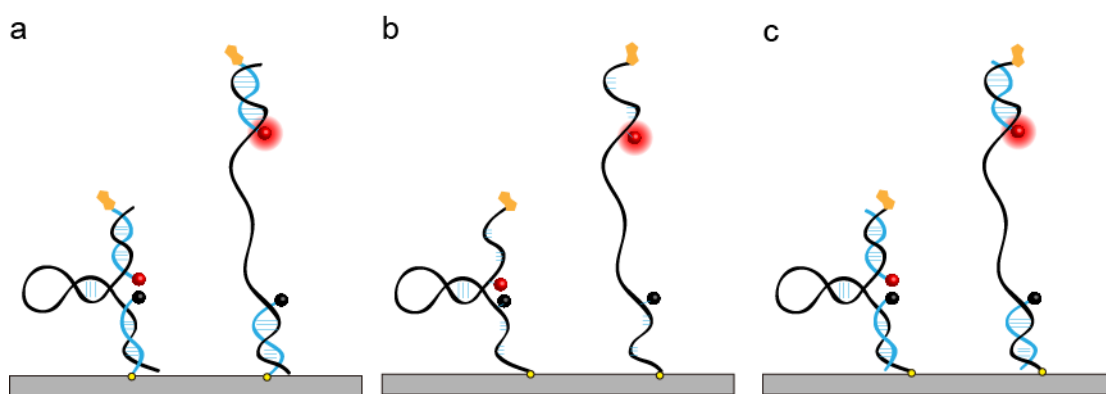
Figure 5.1 Design of DNA-based MTFM with increased mechanical stability. (a) Schematic of three-strand DNA tension probe. The ligand is coupled to the fluorophore-strand. (b) Schematic of single-strand DNA tension probe. All modifications, including ligand, fluorophore, quencher and anchoring group, are all carried by a single-strand hairpin. (c) Schematic of a three-strand DNA tension probe where the ligand is coupled to the hairpin strand to avoid mechanically shearing of the duplex handle.

5.2.3 From 2D to 3D

While previously developed techniques from TFM, mPADs, and our MTFM tension probes have contributed significantly to our understanding of mechanotransduction processes, all of these techniques are restricted to two dimensions. However, physiological processes occur in three dimensions. Recent studies reveal that cells cultured in a three-dimensional matrix show

different ECM interactions.[18-21] Three-dimensional force microscopy has been realized using PEG and collagen hydrogels.[22, 23] Recently, DNA-based hydrogels have been synthesized and well-characterized.[24, 25] The key advantage of DNA hydrogels is that crosslinking is achieved via enzymatic reactions in an efficient manner and under physiologically relevant conditions. In addition, DNA is a biocompatible, biodegradable and relatively inexpensive material, which offers great potential for three-dimensional cell culture. More importantly, the mechanical properties and the macroscopic shapes and sizes of the DNA hydrogel can be finely tuned with different DNA monomers and water content.[26] Combination of DNA hydrogel and DNA-based MTFM probes will provide a new platform for three-dimensional cell traction force measurements.

5.3   *Other contributions and curriculum vitae*

I have also made additional contributions to different projects within the group. A full list of publications is given below:

- Ma, V.P., Liu, Y., Yehl, K., Galior, K., Zhang, Y. and Salaita, K. (2016) Mechanically Induced Catalytic Amplification Reaction for Readout of Receptor-Mediated Cellular Forces. *Angew Chem Int Ed Engl*, **55**, 5488-5492.

- Chang, Y., Liu, Z., Zhang, Y., Galior, K., Yang, J. and Salaita, K. (2016) A General Approach for Generating Fluorescent Probes to Visualize Piconewton Forces at the Cell Surface. *J Am Chem Soc*, **138**, 2901-2904.

- Liu, Z., Liu, Y., Chang, Y., Seyf, H.R., Henry, A., Mattheyses, A.L., Yehl, K., Zhang, Y., Huang, Z. and Salaita, K. (2016) Nanoscale optomechanical actuators for controlling mechanotransduction in living cells. *Nat Methods*, **13**, 143-146.

- Yehl, K., Mugler, A., Vivek, S., Liu, Y., Zhang, Y., Fan, M., Weeks, E.R. and Salaita, K. (2016) High-speed DNA-based rolling motors powered by RNase H. *Nat Nanotechnol*, **11**, 184-190.

- Zhang, Y., Ge, C., Zhu, C. and Salaita, K. (2014) DNA-based digital tension probes reveal integrin forces during early cell adhesion. *Nat Commun*, **5**, 5167.

- Jurchenko, C., Chang, Y., Narui, Y., Zhang, Y. and Salaita, K.S. (2014) Integrin-generated forces lead to streptavidin-biotin unbinding in cellular adhesions. *Biophys J*, **106**, 1436-1446.

5.4   References

1.   Albrecht, C. *et al.* DNA: a programmable force sensor. *Science* **301**, 367-370 (2003).

2.   Liphardt, J., Onoa, B., Smith, S.B., Tinoco, I., Jr. & Bustamante, C. Reversible unfolding of single RNA molecules by mechanical force. *Science* **292**, 733-737 (2001).

3.   Tarsa, P.B. *et al.* Detecting force-induced molecular transitions with fluorescence resonant energy transfer. *Angew Chem Int Ed Engl* **46**, 1999-2001 (2007).

4.   Woodside, M.T. *et al.* Nanomechanical measurements of the sequence-dependent folding landscapes of single nucleic acid hairpins. *Proc Natl Acad Sci U S A* **103**, 6190-6195 (2006).

5.   Blakely, B.L. *et al.* A DNA-based molecular probe for optically reporting cellular traction forces. *Nat Methods* **11**, 1229-1232 (2014).

6.   Wang, X. & Ha, T. Defining single molecular forces required to activate integrin and notch signaling. *Science* **340**, 991-994 (2013).

7.   Liu, Y. *et al.* DNA-based nanoparticle tension sensors reveal that T-cell receptors transmit defined pN forces to their antigens for enhanced fidelity. *Proc Natl Acad Sci U S A* **113**, 5610-5615 (2016).

8.   Wan, Z. *et al.* The activation of IgM- or isotype-switched IgG- and IgE-BCR exhibits distinct mechanical force sensitivity and threshold. *Elife* **4** (2015).

9.   Eliceiri, B.P. Integrin and growth factor receptor crosstalk. *Circ Res* **89**, 1104-1110 (2001).

10.   Porter, J.C. & Hogg, N. Integrins take partners: cross-talk between integrins and other

membrane receptors. *Trends Cell Biol* **8**, 390-396 (1998).

11.   Chang, Y. *et al.* A General Approach for Generating Fluorescent Probes to Visualize Piconewton Forces at the Cell Surface. *J Am Chem Soc* **138**, 2901-2904 (2016).

12.   Morimatsu, M., Mekhdjian, A.H., Chang, A.C., Tan, S.J. & Dunn, A.R. Visualizing the interior architecture of focal adhesions with high-resolution traction maps. *Nano Lett* **15**, 2220-2228 (2015).

13.   biomers.net   (http://www.biomers.net/en/Offers/Duplex_Stability.html)

14.   Aschenbrenner, D., Baumann, F., Milles, L.F., Pippig, D.A. & Gaub, H.E. C-5 Propynyl Modifications Enhance the Mechanical Stability of DNA. *ChemPhysChem* **16**, 2085-2090 (2015).

15.   Severin, P.M., Zou, X., Gaub, H.E. & Schulten, K. Cytosine methylation alters DNA mechanical properties. *Nucleic Acids Res* **39**, 8740-8751 (2011).

16.   Prestinari, C. & Richert, C. Intrastrand locks increase duplex stability and base pairing selectivity. *Chem Commun (Camb)* **47**, 10824-10826 (2011).

17.   Biebricher, A.S. *et al.* The impact of DNA intercalators on DNA and DNA-processing enzymes elucidated through force-dependent binding kinetics. *Nat Commun* **6** (2015).

18.   Cukierman, E., Pankov, R., Stevens, D.R. & Yamada, K.M. Taking cell-matrix adhesions to the third dimension. *Science* **294**, 1708-1712 (2001).

19.   Vargas, D.A. & Zaman, M.H. Computational model for migration of a cell cluster in three-dimensional matrices. *Ann Biomed Eng* **39**, 2068-2079 (2011).

20.   Zaman, M.H., Kamm, R.D., Matsudaira, P. & Lauffenburger, D.A. Computational model

for cell migration in three-dimensional matrices. *Biophys J* **89**, 1389-1397 (2005).

21.   Even-Ram, S. & Yamada, K.M. Cell migration in 3D matrix. *Curr Opin Cell Biol* **17**, 524-532 (2005).

22.   Steinwachs, J. *et al.* Three-dimensional force microscopy of cells in biopolymer networks. *Nat Methods* **13**, 171-176 (2016).

23.   Legant, W.R. *et al.* Measurement of mechanical tractions exerted by cells in three-dimensional matrices. *Nat Methods* **7**, 969-971 (2010).

24.   Lee, J. *et al.* A mechanical metamaterial made from a DNA hydrogel. *Nat Nanotechnol* **7**, 816-820 (2012).

25.   Um, S.H. *et al.* Enzyme-catalysed assembly of DNA hydrogel. *Nat Mater* **5**, 797-801 (2006).

26.   Jiang, H., Pan, V., Vivek, S., Weeks, E.R. & Ke, Y. Programmable DNA Hydrogels Assembled from Multidomain DNA Strands. *Chembiochem* **17**, 1156-1162 (2016).